EUROPIUM COMPLEXES AS PROBES FOR BIOLOGICAL AND MATERIALS APPLICATIONS

By

Laurence Fortunée BENSAID-GEYER

A Dissertation submitted to the Graduate Faculty in Chemistry in partial fulfillment of the requirements for the degree of Doctor of Philosophy,

The City University of New York

2009

This manuscript has been read and accepted for the

Graduate Faculty in Chemistry in satisfaction of the

Dissertation requirement for the degree of Doctor of Philosophy.

Dr Lynn Francesconi

Date	Chair of Examining Committee

Dr. Mahesh K.Lakshman

Date	Executive Officer

Dr. Racquel Z. Legeros

Dr. Charles M. Drain

Dr. Tatyana Polenova

Dr. Marc A. Walters

Dr. Ilona Kretzschmar

Supervisory Committee

THE CITY UNIVERSITY OF NEW YORK

Abstract

EUROPIUM COMPLEXES AS PROBES FOR BIOLOGICAL AND MATERIALS APPLICATIONS

by

Laurence Fortunée Bensaid-Geyer

Advisor: Professor Lynn Francesconi

Europium is a widely used lanthanide due to its emission in the visible region and its long lifetime. It is often complexed with ligands in order to serve different purposes in various domains: these complexes can be used as photostable biological probes but also as photoelectronic devices. This thesis interest will lie on both aspects. In chapter 2, we focused on europium phosphonates for targeting bone cancer. As we look at the adsorption of europium phosphonate to bone, possible scenario can take place: the complex can adsorb to the bone and/or the europium can transchelate from the ligand. If the europium transchelate, we looked at the possibility of a europium incorporation into the hydroxyapatite (HA) structure. We prove the presence of europium within the HA structure using various analytical and spectroscopic methods such as elemental analysis, X-ray diffraction (XRD), Infra-red (IR), luminescence studies, X-ray absorption fine structure (XAFS), and other spectroscopic analysis (SEM, BSE and EDS). In another part, the actual adsorption of europium phosphonate onto HA surface was studied. The adsorption was demonstrated based on luminescence studies showing a

change of europium environment. In chapter 3, solution behavior of lanthanide complexes of the α2-$P_2W_{17}O_{61}^{10-}$ ligand was reported to identify trends that will facilitate rational synthesis of hybrid organic lanthanide polyoxometalate complexes. Based on ^{31}P NMR studies, the equilibrium between the 1:1 and the 1:2 species, that was observed by Pope for the Ce(III) analog is prevalent for the early-mid lanthanides. This equilibrium is slightly dependent on pH but seems to be very much influenced by larger poorly hydrated cations, which appear to favor the 1:2 species for the early to mid lanthanides while they do not appear to influence the equilibrium for the later lanthanides. For all counterions, we found the 1:1 species stable with no trace of the 1:2 species. Finally, in chapter 4, we investigated $Eu[\alpha_1\text{-}P_2W_{17}O_{61}]^{7-}$ (EuPOM) for a layer by layer deposition application with $Zn(phen)_3^{2+}$ (Zn(phen)) and its potential as a electroluminescence device. The depositions were monitored by UV-vis. We successfully fabricated multilayer film via electrostatic interaction between the polyanion $EuPOM^{7-}$ and the polycation $Zn(Phen)_3^{2+}$ until reaching four bilayers when the layers appeared to strip off. Also luminescence studies showed that the multilayer film demonstrated an effective luminescence activity due to the energy transfer through space from the phenanthroline to the europium ion.

Acknowledgments

I acknowledge the considerable patience, understanding, physical and moral support of my family: my husband, Howard; my parents, maman et papa; and my one year old daughter, Avigayil; who I love so much. To them I dedicate my thesis.

Also I want to thank my advisor, Prof. Lynn Francesconi, for her guidance, her advice, her understanding and encouragement through these years. Also I want to thank Dr. Ben Burton-Pye for being like a mentor to me showing such patience helping me.

Table of Contents

Chapter 1: General Introduction

Chapter 3: Europium POM speciation

Chapter 4: Eu(POM) in layer by layer composite

List of Tables

Chapter 1

Chapter 2

Chapter 3

List of Tables

Chapter 1

Chapter 2

Chapter 3

Chapter 1: General Introduction

1.1- Radio-lanthanide-medical application

1.1.1- General medical applications

Lanthanides are elements with atomic numbers between 58 (lanthanum) and 71(lutetium). They are chemically similar because the radial distribution function of 4f electrons are contained within those of the 6s, 6p and 5d shells. In physiological solution, the lanthanides exist as trivalent ions, with the exception of europium and cerium which can also be stable as Eu^{2+} and Ce^{4+}. The configurations range from $[Xe]4f^{0}$ to $[Xe]4f^{14}$. Their 4f electronic shell configuration allows them to possess different photophysical properties. Some of these photophysical properties include luminescence in the visible and the infra red regions after irradiation. They also possess luminescence life times in the order of milliseconds and their emission signal can be separated from scattered light and background fluorescence. These two characteristics make lanthanides good candidates for biological applications such as dissociation enhanced lanthanide immunoassay (DELFIA)[1] and various imaging techniques including imaging macroscopy[2] and magnetic resonance imaging.[3-5] Lanthanides possess radioactive isotopes which can emit γ-rays and/or β-particles and allow them to be used as radio-therapeutic agents or as radio-imaging tracer to visualize and/or treat tumors. The most widely used lanthanide imaging agent as a contrast agent for bone metastatic cancer is phosphonate-gadolinium.[3,4] Samarium-153 and

homium-166 phosphonate chelates also have shown promising results for both treating and targeting bone cancer.[6,7,8,9]

Not related to its photophysical and radio properties, the earliest therapeutic applications of a lanthanide was the use of cerium oxalate as an anti-emetic[10]. In the early 1900s, rare earth salts were being used for the treatment of tuberculosis. Later, the lanthanides were found to have anticoagulant properties, which were discovered after the observation of severe side effects. Atherosclerotic plaque formation was found to be delayed by agents reducing calcium deposition, which led to the investigation of the anti-atherosclerotic properties of lanthanum chloride. Promising results regarding the interaction of the lanthanides with the immune system triggered various investigations of further potential applications[11]. Recently, a new application for lanthanum carbonate (Fosrenol) as a phosphate binder for the treatment of hyperphosphatemia in renal dialysis patients has been approved in both the USA and Europe[12]. Fosrenol is the latest metal-based drug on the market, it is all the more important as it provides an alternative approach to controlling the intake of dietary phosphate without the adverse effects associated with the current aluminum and calcium based phosphate binders.[13]

All of the lanthanide elements possess radioactive isotopes; many are both β-emitting particles as well as gamma rays.[14] The β^- particles can have different energies and half lives. Higher energy β^- particles can penetrate farther into tissue which can be utilized to kill the tumor cells; specificity of the molecule to the area of the tumor is critical in this case as high energy β^- particles can also irradiate bone marrow. The half life of the radionuclide is critical as well: radiotherapeutic agents that take hours or days before localizing in the target tissue require long-lived radiolanthanides. In contrast, agents that

quickly localize should employ short-lived, high-energy radionuclides. The variety of nuclear properties offers the possibility for developing specific chemistry by choosing a specific lanthanide to be incorporated into a carrier and target the diseased tissue. They have been considered as therapeutic agents since the beginning of nuclear medicine.

Several studies have shown the potential therapeutic applications of the radiolanthanides: (i) as bone agents for pain palliation for bone cancer using samarium-153 (^{153}Sm); (ii) as microspheres and colloids for radiation synovectomy using yttrium-90 (^{90}Y) as yttrium citrate, dysprosium-165 (^{165}Dy) in a form of particulate dysprosium ferric hydroxide macroaggregate, homium-166 (^{166}Ho) and ^{153}Sm; (iii) and as a label of monoclonal antibodies for radioimmunotherapy with lutetium-177 (^{177}Lu) and ^{166}Ho. ^{153}Sm, prasedinium-149 (^{149}Pm), terbium-161 (^{161}Tb), ^{166}Ho, and ^{177}Lu have been bound to monoclonal antibodies and peptides for treatment of different types of tumors.[15] Yttrium-90 microspheres, either in the form of resin beads or glass, are currently used to treat unresectable hepatocellular cancer.[16] Surgical resection, regional administration of chemotherapeutic drugs and external radiotherapy are presently being used as the therapeutic modalities for the treatment of liver cancer. For the tumors which do not respond well to chemotherapy and external radiotherapy, such as liver cancer and liver metastases, intra-arterial radionuclide therapy using suitable β-emitting radionuclides has emerged as a promising alternative method where the β-emitters are incorporated into microspheres.[17] A number of β-emitting radionuclides such as, ^{90}Y, ^{131}I, ^{166}Ho and ^{188}Re have been used for the treatment of primary as well as metastatic liver cancer, either in the form of suitable radiolabeled particulates or with lipiodol, which serves as the embolizing agent.[18,17,19] Recently, yttrium was added to the composition of a bioactive glass in order to

develop a biodegradable glass system able to carry the radiation inside the cancer site and provide a high and localized dose of β radiation and used for liver tumor.[20,21]

The three most investigated radiopharmaceuticals are (^{111}In-DTPA)-octreotide, (^{90}Y-DOTA^{0},Tyr^{3})-octreotide (DOTATOC), and (^{177}Lu-DOTA^{0},Tyr^{3},Thr^{8})-octreotide (DOTATATE), where DTPA is diethylenetriaminepentaacetic acid, DOTA is tetraazacyclododecane tetraacetic acid and TOC is $_{D}$-Phe-$_{C}$(Cys-Tyr-$_{D}$-Trp-Lys-Thr-Cys)-Thr(ol). All three are in clinical trial for metastatic neuroendocrine tumors. In recent years, ^{177}Lu has emerged as a promising radionuclide for in vivo therapeutic applications due to its suitable decay properties (see Table 1.1).[22] Lu-177 labeled monoclonal antibodies have shown potential in clinical trials against small peritoneal metastases of colorectal origin.[18,22] Lu-177, a low-energy electron–emitting radiolanthanide, is starting to be used as a replacement for the high-energy electron–emitting nonlanthanide ^{90}Y. Both ^{90}Y-labeled and ^{177}Lu-labeled somatostatin analogs and antibodies have shown promising results in the treatment of tumors. Also, with ^{177}Lu-DOTATATE and ^{177}Lu-DOTATOC encouraging results were found to treat neuroendocrine tumors. ^{177}Lu-DOTATATE and ^{90}Y-DOTATOC have been on trial for their use as peptide receptor of radionuclide therapy to evaluate renal toxicity after peptide receptor radionuclide therapy. They have been useful for the management of patients with inoperable conditions or metastasized neuroendocrine tumors. These complexes have the ability to irradiate the tumors and their metastases through a specific receptor subtype. ^{177}Lu-DOTATATE has shown encouraging preclinical results against various neuroendocrine tumors.[15,23,24,25] In the same spirit, Forrer reported the successful investigation using ^{177}Lu-DOTATOC after the ^{90}Y-DOTATOC for patients with relapse of neuroendocrine tumors.[26-29]

*Table 1.1. Physical characteristics of γ-emitters used most often in radioimmunotherapy (J Nucl Med. **2004**, 45, 1224-1232; Journal of Nuclear Medicine **2006**, 47, 534)*[18,30]

Radionuclide	Half-life	Maximum β-particle (MeV)	Maximum penetration depth (mm)	γ-emission keV (%)
^{131}I	8.0	0.606	3.0	364 (82),637 (6.5)
^{90}Y	2.7	2.28	12.0	None
^{186}Re	3.8	1.08	5.4	137 (9.5)
^{177}Lu	6.7	0.497	2.5	208 (11), 113 (7)
^{166}Ho	27	1.85(51%) 1.77(48%)	8.7 in soft tissue 3.8 in bone	81(7%) 1400(1%)
^{153}Sm	46.3	0.233	3 in soft tissue 2 in bone	103

1.1.2- Lanthanides to treat bone cancer

Both samarium-153 and homium-166 decay by gamma ray emission, which permits conventional gamma-camera imaging. They are also β-emitters, which allows them to be used for therapeutic applications.[31,32] The radiolanthanide samarium-153 complexed with ligands containing phosphonate groups, such as EDTMP, (ethylenediamine tetramethylene phosphate) known as Quadramet^{TM}, is in clinical use for bone pain relief and treatment of bone metastasis [33]. Although the mechanism of pain relief by Sm-153 is not known, it is believed that the β-emission from this isotope causes cytotoxicity to adjacent cells and inhibition of tumor growth, resulting in an analgesic effect[34]. ^{166}Ho complexed with DOTMP (1,4,7,10-tetraazacyclododecane-1,4,7,10-tetramethylene-phosphonate) recently completed its clinical trial for myeloablative treatment of multiple myeloma and ^{166}Ho complexed with DTPA (diethylenetriaminepentaacetic acid) is under investigation for intravascular radiation therapy.[6,35,7,36,37,38,39-41,42,43,44,45] Also, ^{177}Ho-EDTMP and ^{166}Dy-EDTMP have been found to produce more radiation dose to marrow than Sm-EDTMP or

even Ho-DOTMP per unit of initial activity retained in the skeleton which make them good candidate for bone marrow ablation.[46]

1.1.3- Potential of lanthanides in bone cancer treatment

Lanthanides have a similar ionic radii to calcium of about 1 Å. Therefore, they have been more prone to incorporate into calcium sites and have been used as probes for calcium. Because of their higher charge they have a high affinity to the Ca^{2+} sites on biological molecules and a high binding to water molecules. The preferred coordination number of lanthanides is 8 or 9 which is quite higher than the 6 coordination of calcium. Also, their spectroscopic properties due to their 4f shell make them a useful probe for calcium in biological systems using techniques such as NMR (chemical shift reagents), luminescence or fluorescence spectroscopy. In addition, they share similar biological properties. Ln^{3+} has been found to block both voltage operated and receptor operated calcium channels[47]. It can block the Na^{+}/Ca^{2+} synaptic plasma membrane exchange, and inhibit skeletal, smooth, and cardiac muscle contraction by blocking the the Ca^{2+} ATPase in the sarcoplasmic reticulum of muscle. They have already been used as biochemical probes to study calcium transport in mitochondria and other organelles as they block the exterior face of the calcium channel.[48,49] Aside from this characteristic they have the ability to form stable complexes with phosphonated chelates, which have a good affinity to bone and therefore allows a facile radiation delivery of the lanthanides to bone. These aspects will be developed in more detail in the following sections.

1.2- Ligands that bind to lanthanides

1.2.1- Introduction

The potential use of lanthanide complexes as therapeutic agents in nuclear medicine is of interest. The important factor to be considered for their *in vivo* use is their stability in physiological conditions in order to prevent their dissociation in blood and the formation of species resulting from binding to blood components. In that respect, the rigidity of the chelators, their cavity size for macrocyclic ligands, the nature and number of their donor atoms are factors that need to be addressed because they can have an effect on the chemical and biological behavior of these lanthanide complexes. As mentioned earlier the coordination numbers preferred for lanthanides are 8 or 9. Lanthanides are hard Lewis acids which enable them to bind to elements that are hard Lewis bases such as nitrogen, oxygen or fluorine. This explains the ability of water molecules to quench luminescence through O-H oscillatory harmonics (see Section 1.5.3). As carboxylic groups or phosphate groups are good hard anionic donors, they have been largely used in lanthanide complexation in order to increase the stability of the lanthanide-ligand complex. This stability is very important considering that they are toxic and should not dissociate from the ligand.

The most common types of ligands to which lanthanides can be bound are ethylenediamine tetraacetic acid (EDTA) and diethylene triamine pentaacetic acid (DTPA) derivatives and 1,4,7,10-tetraazacyclododecanetetraacetic acid (DOTA) derivatives. The metal ion is encapsulated within the ligand through the binding with the hard donor nitrogen atoms. These donor groups which can wrap around the lanthanide to limit the binding of water molecules. Moreover, these groups can be modified to fit the kinetics and

thermodynamics of the complex which is crucial in our investigation.

1.2.2- DOTA and EDTA derivatives: properties and characteristics

EDTMP is a derivative of EDTA. The lanthanide EDTMP complexation works in a similar fashion to its carboxylic derivative, EDTA by wrapping around the lanthanide. These hexadentate ligands coordinate through two nitrogen atoms and four oxygen atoms so that only one oxygen atom from each of the phosphonate and carboxylate groups bind to the metal ion center.

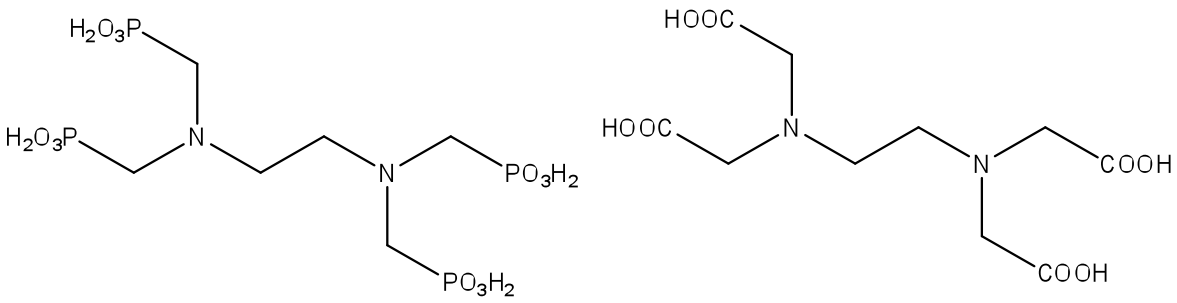

Figure 1.1. Structural formula of the ligands EDTMP (left) and EDTA (right).

According to a recent crystal structure,[50] the europium EDTMP complex is coordinated to the 2 nitrogen donor atoms and four oxygen donor atoms of EDTMP and the coordination sphere is completed with 2 oxygen atoms from the carbonate molecule whereas in the europium EDTA the inner sphere is completed by 3 water molecules.[50] The lanthanide complexed EDTMP can form 4 types of complexes: non-protonated and mono- and diprotonated[51]. At physiological pH the complex present is found to be the non-protonated $EuEDTMP^{5-}$ species.[50]

Due to their open structure, the two ligands DTPA and DTMPA with a phosphonate group substituting the central carboxylate group form complexes with Gd^{3+} that are kinetically different. The Gd^{3+} complexes formed with DTPA derivative ligands dissociate one thousand time faster than Gd(DTPA).[52]

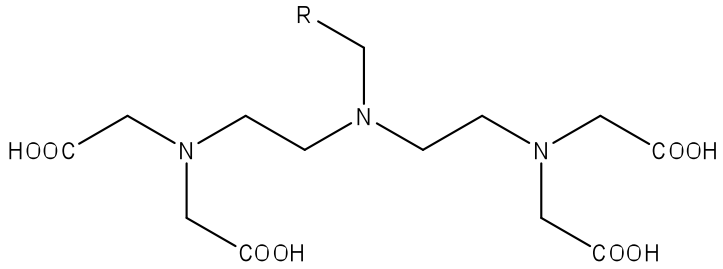

Figure 1.2. Structural formula of the ligand DTPA and its phosphonated derivative DTMP

However, the monoprotonated $HEDTMP^{7-}$ complexed with lanthanides has a dissociation rate 10 times lower than the analogue monoprotonated $HEDTA^{3-}$ complex due to the higher negative charge favoring a strong electronic interaction with the lanthanide Ln^{3+}. Therefore, the stability constant of $Sm(EDTMP)^{5-}$ and $Y(EDTMP)^{5-}$ have been found to be higher than those of $Sm(EDTA)^{-}$ and $Y(EDTA)^{-}$ by 2-3 log K units. The stability constant of Sm(EDTMP) and Y(EDTMP) were determined by competition reaction with log K_{ML} values of 20.7 and 19.19 respectively.[53] Near to physiological conditions, where ^{153}Sm(EDTMP) is used as a palliative agent, Sm^{3+} is predominantly present as $[Sm(HEDTMP)Ca]^{-2}$. Similarly, within pH 7-9 the rates of dissociation of the Ln(EDTMP) complexes are much higher than these of Ln(EDTA). Their short half time dissociation

suggest that the complexes do not adsorb to bone rather the ligand and Ln^{3+} ions adsorb separately after transchelation. For that reason, when used for radiotherapy, these ligands are often injected in excess to prevent metal loss from the complex and since the presence of free lanthanide ions in the body which could be toxic [9].

In contrast, the associated macrocyclic ligand DOTA or its phosphonated analogue DOTMP show different stability properties than the EDTA or EDTMP. They are the most thoroughly studied ligands for the complexation of lanthanides [54].

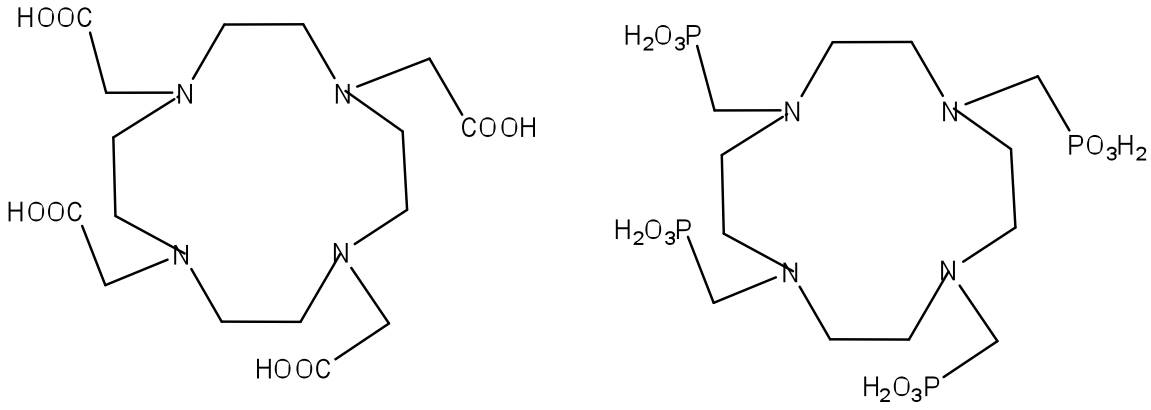

Figure 1.3. Structural formula of the ligands DOTA(left) and DOTMP(right).

They are very popular ligands due to their complexation with gadolinium. The resulting complexes have huge medical application as MRI contrast agents.[3,55] The rate of dissociation of these particular complexes is very slow. Due to their cavity of the four nitrogen atoms which can accommodate the size of a lanthanide ion, they are thermodynamically very stable with a stability constant K_{ML} reaching 28 for Gd(III)DOTA and ranging from 27.6 to 29 through the lanthanide series when complexed with DOTMP[56,5]. These stability constant values were determined by potentiometry, supported

by NMR and calorimetry.[57] The protonation constant indicates that this complex forms 4 protonated complexes within a pH range of 3-9, where the mono-protonated complex predominates at physiological pH.[57]

1.3 Ligands that bind to bone

1.3.1- Bone

The skeleton consists of cartilage, bone and soft tissues. The skeleton provides the structural foundation of the body, the bones in the skeleton protect the tissue organs and tissue of the bone marrow. It is therefore the most subjected to osteoporosis, arthritis, periodontal disease, and metastasis disease. Factors related to bone physiology are important. They include heterogeneity in bone remodeling activities through the skeleton, differences in blood supply and local vascularization, and the blood "bone-barrier". Also bone serves as source and depot for mineral, especially calcium and phosphate. It has different functions including, mechanical support of soft tissues, levers for muscle action, protection of the central nervous system, release of calcium and other ions for the maintenance of a constant ionic environment in the extracellular fluid, and housing and support of hemopoiesis.[58] In order to accomplish these functions bone undergoes resorption and formation continually and therefore is involved with mineral homeostasis.[59,60]

Bone is a composite of an inorganic and an organic phase, about 65% and 35%. The organic phase is mostly type I collagen. The inorganic or mineral phase of bone has been idealized as hydroxyapatite (HA) with the stoichiometric formula, $Ca_{10}(PO_4)_6(OH)_2$ [61] but has been shown to be a carbonate containing apatite, approximated by the formula,

$(Ca,Na,Mg)_{10}(PO_4,CO_3)_6(OH)_2$.[62] This mineral phase can bind certain molecules, which provides an avenue towards treating skeletal disease using targeted drug delivery. Because the membrane of bone consists in lining cells which function as marrow-bone barrier, the accessibility of outside large molecules approaching the bone surface is limited [63].

1.3.2- Biphosphonates

Since the 1970s biphosphonates have been used clinically to treat bone resorption. Due to their acidic and highly soluble properties, they hardly penetrate biological membranes[64]. Their high affinity to calcified tissue explains their characteristic of being bone specific. They have demonstrated great success treating Paget's disease, myeloma, osteoporosis and bone metastases. Biphosphonate is an analogue to pyrophosphate and exhibits similar behavior in relation to calcium phosphate and HA. It is shown to inhibit precipitation of calcium salts from solution, of mineral dissolution and inhibit growth of calcium phosphate crystals.[65,66] The bonding to the bone works through their P-C-P back bone, where C is carbon and P is the phosphonate group. This chain will then act as a hook onto the bone. Two side groups are attached to the carbon, R1 and R2.

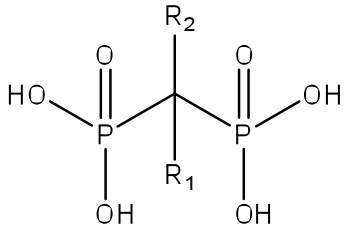

Figure 1.4. Sketch of generic bisphosphonate structure showing R1 and R2 pendant arms.

If R1 is a hydroxyl group it acts as a third possible binding hook onto the bone. The R2 group can be a nitrogen containing group. The nature of this side group influences other surface properties such as interfacial tension and zeta potential. Their differences in binding affinities affect the potency of individual biphosphonates and establish their uniqueness towards different pharmaceutical applications.[67,68] A very prominent feature of these high affinity biphosphonate conjugates is their long retention in the bone due to their stability of the P-C-P bond against enzymatic degradation. The mechanism of the skeletal uptake of the biphosphonate is a simple adsorption onto the bone. Unlike normal bone, metastatic bone does not undergo continuous remodeling. This process is performed by 2 different cell types, osteoclasts and osteoblasts. Osteoclasts resorb bone, whereas osteoblasts replace bone. During bone resorption, growth factors and mineral ions such as calcium are released from the bone matrix. When bone metastases occur, a cycle of signaling takes place that results in increased osteolytic activity.[69] Bisphosphonates are reducing bone turnover and bone loss via inhibition of osteoclast mediated resorption. Through the phosphate moieties the bisphosphonates bind to bone. They localize at the site of bone turn over. After bonding to the bone surface they either cause a toxic effect on the osteoclasts surrounding them or interfere with specific osteoclast intracellular pathways.[70]

The applications of the biphosphonates and pyrophosphate as diagnostic agents are dependent upon their affinity for bone and their ability to link to a so called tracer such as γ-ray emitter technetium-99m (^{99m}Tc).[71] Concerning their elimination process, biphosphonate-Tc-99m conjugates are polar under physiological condition which implies their clearance from the body via urinary and biliary excretion depending on their molecular size. [72,73,74]

1.3.3- Stability of bisphosphonate

Early stability studies have been conducted determining the degree of exchange of the radiometal bisphosphonate complexes with HA. The affinity constants were determined through kinetic studies on HA crystal and physiologic conditions. Three parameters were assessed: binding affinities, zeta potentials, and interfacial tension. A significant difference in binding affinity was attributed to the differences in N-containing R2 functional group (Figure 1.4). This group can influence the binding and release of the bisphosphonate with the HA.[68] Through biodistribution studies, Ketring and Li interrogated the lanthanide to determine if it transchelates to the bone or clears through the urinary track with little dissociation. They reported that the bone uptake may result from two possible sources, either transchelation of the lanthanide from the ligand due to a higher affinity of the Ca^{2+} on the bone surface for the phosphonate ligand or some of the radiolanthanide complexes associate with calcified area through the capillaries.[75,76] They found the stabilities of the complexes to be dependent upon the lanthanide and the ligand used. The stability of a series of chelates-lanthanide complexes have been studied by Li. The chelates evaluated were EDTA, CDTA, DTPA, MA-DTPA (monoamide-DTPA) and DOTA.[76] They measured the exchange between the radiolanthanide complexes and HA *in vitro*. *In vitro*, they found that the smallest Ln forms the most stable complex. The order of stability observed was ^{177}Lu-L > ^{153}Sm-L> ^{140}La-L where the stability decreases as the lanthanide gets bigger. Also, he found that Ln-DOTA (logKs ~ 23)> Ln-DTPA> Ln-EDTA (logKs~17), due to the chelate denticity and the macrocyclic effect. *In vivo*, after monitoring the urinary excretion, the liver and bone uptake, he also observed that the

urinary excretion of the EDTA complexes decreased from ^{177}Lu to ^{140}La indicating a loss in stability in the direction of ^{140}La, consistent with the *in vitro* studies.

Similar studies, directed by Simon, were performed with the phosphonated analogues. Samarium complexes with a series a phosphonated ligand gave us thermodynamic stability constant (Ks) values ranging from 16.9 to 25 at neutral pH were Ks for ^{153}Sm-NTMP < ^{153}Sm-DTPMP < ^{153}Sm-EDTMP < ^{153}Sm-DOTMP. The Ks of the corresponding carboxylated ligands range from 15 to 23 following the same order[77]. Because ^{153}Sm-EDTMP is not kinetically inert, it is used with a large excess of ligand to Sm-153 ratio for routine clinical application. The typical dose administered is 1mCi/kg.[78] However, Majkowska recently found that Zoledronic acid ((1-Hydroxy-2-imidazol-1-yl-phosphonoethyl) phosphonic acid monohydrate), known as *Zometa*, demonstrated a better stability with Lu-177 than other biphosphonate labeled with Sm-153 and Ho-166.[79]

1.3.4- Bisphosphonate binding to bone

Stability studies on lanthanide complexes with DOTA derivatives, BPAMD and BPAPD (see Figure 1.5), suggested that the biphosphonated moieties are not bound to the lanthanide rather they are the one responsible to the binding to bone.[80]

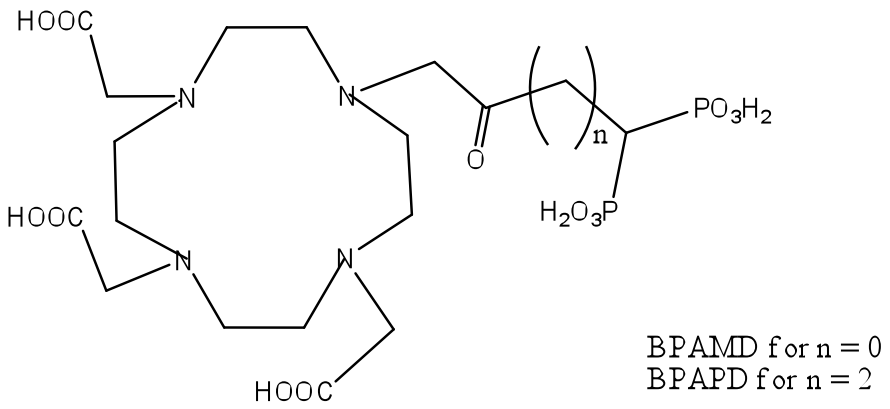

Figure 1.5. Structural formula of the ligands BPAMD and BPAPD.

A study from Försterová, on ^{153}Sm and ^{166}Ho complexes of 1,4,7,10-tetraazacyclododecane-1,4,7,10-tetrakis(methylphosphonic acid monoethylester) (H4 DOTMP OEt) confirmed this observation. They reported that these complexes showed a low binding to HA and calcified tissue which implies that a fully ionized phosphonate group is necessary for a strong bone affinity.[81]

Recently, Rill et al reported a temperature-dependent adsorption study using terbium-135 (Tb) DOTP and DOTA derivative 10-((diphosphonoethyl(hydroxy)phosphoryl)methyl)-1,4,7,10-tetraazacyclododecane-1,4,7-tri(acetic acid) (BPPED). They found the presence of different adsorption sites on the HA surface. Also, they reported that the Tb(BPPE) ligand showed a better adsorbing ability than the Tb(DOTP) and attributed it to the availability of the phosphonate chelating groups, not involved in binding with the central Tb^{3+}. They ascribed this adsorption phenomenon to the displacement of a phosphate group on the HA surface by the phosphonate groups of the ligand.[82]

1.3.5- Medical applications: use as ligands for bone cancer

Bone is a sensitive area for primary and metastatic diseases. The types of cancer that lead in major cases to metastasis are the lungs, breast, prostate, thyroid and kidney. The most common symptom of metastasis is pain. It can be attributed to the stretching of the periosteum by the tumor or the weakening of the bone which ends up causing fractures or tumor growth into surrounding tissues. Metastatic bone lesion can be osteolytic, osteoblastic and mixed. Multiple myeloma (also known as myeloma or plasma cell myeloma) is a progressive hematologic disease. It is a cancer of the plasma cell, an important part of the immune system that produces immunoglobulin to help fight infection and disease. Multiple myeloma is characterized by excessive numbers of abnormal plasma cells in the bone marrow which leads to the formation of tumor in the bone. Multiple myeloma, a cancer of the plasma cell, is an incurable but treatable disease.

Nowadays a large percentage of people suffering from breast, lung, or prostate cancer develop bone metastases due to extended longevity. Bone pain is a frequent complication. There are several promising new therapies that are helping patients live longer, healthier lives. Among these treatments are chemotherapy and total body irradiation. Their objective is to kill the cancer cells. The essential role of the phosphonate agents for such therapies is their ability of linkage to the bone, which would allow the facile delivery of radiation to the bone and further would permit the propagation of the radiation at minimal dose to other organs. They also have the ability to be used as an agent for drug delivery to the bone. Presently, pyrophosphate is used in palliation of pain. It inhibits bone resorption by inhibiting osteoclastic activity. But other synthetic analogs such as bisphosphates,[83,84] may also show similar characteristics towards bone palliation and therefore be of great use.

The selective attachment of radiolanthanides and radionuclides such as ^{166} Ho and ^{153}Sm and rhenium-186/188 ($^{186/188}$Re) to bone of patients suffering from bone metastasis may also have a pain palliative effect.[9] Therapeutic radiopharmaceutical labeling is a way to radiolabel a molecule in order to deliver therapeutic dose of ionized radiation to specific tumors with high selectivity in the body. Various radiolabels have been used for this purpose for the past six decades. For example, therapies using ^{131}I-sodium iodide have been developed for thyroid cancer treatment.

Recently bone seeking radiopharmaceuticals containing nuclides that are beta emitters[6] such as phosphorus-32, ^{32}P sodium orthophosphate, and strontium-89 chloride, $^{89}SrCl_2$, have been clinically approved for bone pain palliation associated with skeletal metastasis. Unlike strontium, lanthanides must be chelated in order to survive the transport in the blood and the delivery to the bone surface. Lanthanide oxides are basic and unless chelated, they rapidly form insoluble rare earth hydroxides in blood, which is buffered near neutral pH.

For the past 20 years, the use of geminal bis(phosphonates) have been widely reported in medical treatment for bone tumors[85]. The bone-seeking ability is through a methylenediphosphonate group present in the ligand, as it was found by Adzamli *et al.* and Kubicek *et al.*[86]. Several methanediphosphonate derivative ligands are commercially produced and marketed as drugs for the treatment of osteoporosis. The bis(phosphonic acid) group shows a high affinity to the bone surface and is a non-hydrolyzable, analogue of natural pyrophosphate. The adsorption of the bis(phosphonates) on the bone is preferentially localized in active areas of bones where growth and pathological changes occur. For example, the methanediphosphonate ligands have been found to mobilize Ca^{2+} and Mg^{2+} ions from the plasma and increase the amount of the two metal ions available for

deposition on bones[87]. More recently, Contrast Agents for MRI with phosphonates and bis-(phosphonates) as targeting groups have been developed[85,88,89,90]. Polyaminocarboxylate ligands have been developed to form stable complexes *in vivo* with lanthanides.

As mentioned earlier, phosphate complexes are used as delivery agents of radiolanthanides[80] for pain palliation of the bone tumors and for therapy of multiple myeloma. The complex of ^{153}Sm with ligands containing the biphosphonate EDTMP, known as Quadramet^{TM}, are in clinical use for bone pain relief and treatment of bone metastasis [91-93]. The ^{153}Sm(EDTMP) showed the best combination of high bone uptake lowest blood and nonosseous tissue activity. This agent has been clinically approved for bone disease palliation or for targeting bone tumors. In 1988[94] and 1995[95], two *in vitro* experiments were performed with ^{153}Sm-EDTMP on HA. From both studies it was observed that Sm-EDTMP was absorbed as a complex onto calcium HA (up to 40 μmol SmEDTMP/g of Ca) and that it is not easily removed by excess complex, EDTMP or DTPA. The authors suggest that only the complex is absorbed but not the free Sm^{3+}.

Sm-EDTMP was first reported as a potential radiopharmaceutical for treating bone tumor by Goeckeler et al. [6,96]. Due to its high energy β-particle (E_β(max) = 1.85 MeV) ^{166}HoDOTMP has been in clinical trials to treat multiple myeloma and was considered for ablation of bone marrow. Even though it is a bone-seeking complex, ^{166}HoDOTMP cannot be use for treatment of skeletal metastases since it emits a high-energy β-particle. The long-range of the β-particles produces excessive marrow suppression when compared to ^{153}Sm-EDTMP. Since these highly penetrating β-particles destroy bone marrow cells remote from the surface of the bone where ^{166}Ho-DOTMP deposits, it can be used for eradication of multiple myeloma cells and the normal stem cells located in the marrow space[9]. Using

electron microscopy and electron probe X-ray analysis, M. D. Chamber reported[97] that SmEDTMP, prepared on macroscopic level, was found to localize in growing areas of rat bone matrix or more specifically in the layer undergoing mineralization.

This suggests that there is a strong interaction between SmEDTMP (and HoDOTP) and HA *in vivo*. Nevertheless, the mechanism of uptake in bone for lanthanide phosphonates, such as ^{153}SmEDTMP and for ^{166}HoDOTMP, remains unsolved at this time. The choice of the chelate structure has been revealed to be crucial in the amount of skeletal uptake. The greater the stability of the complex the lesser the ability of the lanthanide to attach to the bone.

1.4- Synthetic and bone apatites

1.4.1- Preparations of apatites

Synthetic apatites are prepared in order to mimic and understand the formation of the biological apatite and its properties. The first synthesis of apatite was from Daubree in 1851, when HA was made by passing phosphorus dichloride vapor on red hot lime. Hydroxyapatite, $Ca_{10}(PO_4)_6(OH)_2$, with a stoichiometry of 1.67 Ca/P ratio can only be obtained by solid state reaction or by sintering apatite with low carbonate content at temperatures of 900^{o}C and above [62]. Most synthetic and biologic apatites (e.g., mineral phases of teeth and bones) are usually calcium-deficient (i.e., Ca/P less than the stoichiometric value of 1.67). Biologic apatite such as bone apatite can be best described as a substituted apatite, specifically, carbonate apatite. The major constituents of biological apatites are magnesium (Mg) and carbonate (CO_3) ions substituting in the apatite lattice:

Mg for Ca, CO_3 for PO_4. Mineral apatites are also substituted apatites: e.g., Pb, Mn and other cations for Ca; CO_3, SO_4, or MnO_4 for PO_4, Cl or F for OH. Morphology, crystallite size and other physic-chemical properties of the apatite are determined by the type and amount of substitution in the apatite lattice and by the preparation method[62]. The methods of preparation can be divided into three major groups: the hydrothermal method using high temperature-pressure conditions [98,99], solid-state reaction methods at high temperature[100], precipitation[101,102], and the wet chemistry method at relatively low temperature. Also other methods have been used less widely such as sol–gel[103], uttering[104], mechanochemical[105], mechanochemical–hydrothermal[106,107], microemulsion[108], self organization mechanism[109] and others. The solid state reaction method has been used for studying phase stabilities. The powders have irregular forms with large grains size and a heterogeneous composition. The wet chemistry method is much more popular due to its tenability and easiness to conduct in a simple laboratory. Also this method closely mimics the closest the physiological conditions for studying formation mechanism of calcium phosphate phases and adsorption mechanism on HA in vivo and in vitro. For the precipitation method, the reaction temperature and pH are crucial. The crystallinity (reflecting crystal size) of the apatite obtained highly depends on the reaction temperature: the lower the temperature, the lower the crystallinity[62]. Also, when working at a temperature lower than 80°C, the reaction pH becomes very important. For example, formation of different calcium phosphate phases (e.g. dicalciumphosphate dihydrate (DCPC), dicalcium phosphate anhydrous (DCPA), octacalcium phosphate (OCP), or Mg-substituted beta-tricalcium phosphate (β-TCMP) in the presence of Mg[62]. On the other hand, the hydrothermal method has priority over the other methods for the preparation of ceramic such as HA, due to the

effect of hydrothermal fluids on solids [110]. Hydrothermal vapor treatment method was used to prepare HA with different porous characteristic. As a unique method, the hydrothermal method allows for control of the crystalline phases, pore structure and the chemical composition. The powders are crystalline with homogeneous and uniform composition and they can be sintered easily. Therefore it allows the control of the crystal morphology. Hydrothermal treatment consists of mixing aqueous solutions for example $(NH_4)_2HPO_4$ and $Ca(OH)_2$ in a reactor at high pressure- temperature conditions (>100 °C, <1 atm) and also under saturated vapor pressure at temperature below 200 °C [98]. Even though, the hydrothermal solid state reaction lead at 375°C is the best method to prepare pure HA, the method of choice used for this project will be the precipitation method which will lead to a more impure HA but structurally closer to the biological HA system.

The method of choice used for this project was the precipitation method because apatites structurally closer to the biological apatites can be obtained. Using the appropriate reaction temperature and pH the desired apatite and crystallinity can be obtained.

1.4.2- Characterization

(a) X-ray diffraction method.

In 1926 using X-ray diffraction and chemical analyses, the mineral composition of bone and enamel was identified as hydroxyapatite (HA). HA has an hexagonal structure with a space group of $P6_3/m$ with the OH groups displaced from the mirror plan z = ¼ and ¾ [61]. Presently, several analytical methods are used to characterize apatite preparations. The most widely used to prove the presence of HA is the X-ray diffraction (XRD) analysis. The XRD analysis of synthetic Ca-P powder can give information about the, structure, identity,

crystallite size and lattice parameters (a- and c-dimensions). The structure and identity are determined by the reflection pattern and the intensities of the reflections. X-rays are diffracted by the lattice of the crystal to give a unique pattern of peaks or 'reflections' at certain diffraction angle (d-spacing) and with different intensity. The diffracted beams from atoms in successive planes cancel unless they are in phase, and the condition for this is given by the BRAGG relationship.

$n\lambda = 2\ d \sin \theta$

λ is the wavelength of the X-rays

d is the distance between different planes of atoms in the crystal lattice.

θ is the angle of diffraction.

The X-Ray detector moves around the sample and measures the intensity of these peaks and the position of these peaks [diffraction angle 2θ]. The highest peak is defined as the 100% peak and the intensity of all the other peaks is measured as a percentage of the 100% peak. For HA study, the main peaks are between 20° to 40° in 2θ, which is where the HA's more intense and therefore characteristic peaks are found (Figure 1.6, Table 1.2). Comparison of both the intensity and $2\ \Theta$ value of these reflections with databases will reveal the identity of the calcium phosphate sample. The peaks at 31.88° 2θ for the plane [300], and 25.88° 2θ for the plane 002 of HA are characteristic of HA structure.[62]

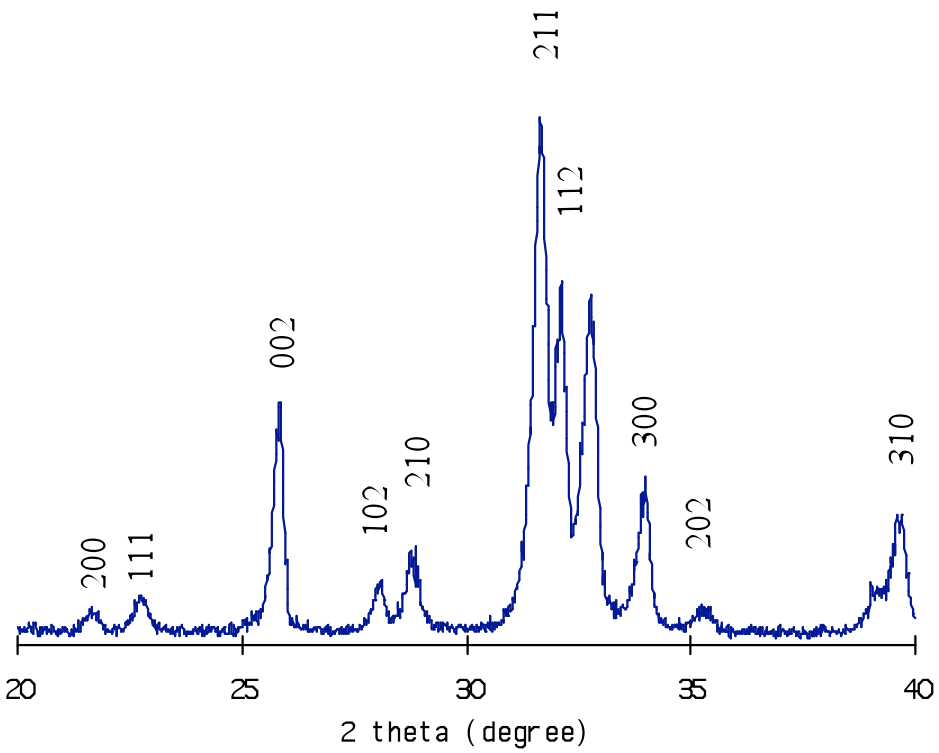

Figure 1.6. XRD pattern of hydroxyapatite HA from sample made following the precipitation method.

Table 1.2. Database 1-42 of the apatite $Ca_5(PO_4)_3(OH)$ with a radiation $\lambda = 1.54056nm$. The system is hexagonal, P63/m with a = 9.418 Å, and c = 6.884 Å.

2Θ	Intensity	h k l
21.819	10	200
22.902	10	111
25.879	40	002
28.126	12	102
28.9	18	210
31.773	100	211
32.196	60	112
32.902	60	300
34.048	25	202
39.818	20	310

The XRD profile also provides information on the crystallinity of the apatite. Apatite preparations with high crystallinity (large crystals) show narrow peaks with high intensity. Apatite preparations with low crystallinity (small crystals) show broad peaks with low intensity. Determination of crystallite size (along the a- or c- axis) is performed using the Debye-Scherrer equation:

$$D = K\lambda/\beta_{1/2}\cos\Theta$$

D = dimension

θ = two theta angle of the (002) or (300) diffraction peak

$\beta_{1/2}$ = broadening of the diffraction peak or peak width at half height $(B^2\text{-}b^2)^{1/2}$

Determination of the lattice parameters (a- and c-axes dimensions) are calculated from the d-spacings of their diffraction peaks, using the formula:

$$d = \frac{1}{\sqrt{\frac{4(h^2 + k^2 + hk)}{3a^2} + \frac{1^2}{c^2}}}$$

d = spacings between reflecting planes

hkl = Miller indices of reflecting plane e.g., (002) or (300)

However determination of the a- and c-axis dimensions of an apatite with low crystallinity (such as apatites prepared at low temperatures, 25 to 37 ^{o}C or apatites containing considerable substituents that promote strain or cause formation of apatites with small crystallites is less accurate. [62]

(b) Infrared (IR) spectroscopy method.

Infrared (IR) spectroscopy is another method to characterize apatite preparations.[111-115] The IR spectra arise from the different modes of vibration and rotation of functional groups in the compound. The apatite IR can give information on identity, purity (presence of different phase), presence of functional groups (in the apatite PO_4^{3-},HPO_4^{2-}, $H_2PO_4^-$ CO_3^{2-}, OH^-) its environment, effect of the incorporation of another element (such as fluoride F^- or lanthanide (III) cations), type of substitution (CO_3^{2-} for OH^- or CO_3^{2-} for PO_4^{3-}) and crystallinity induced from the resolution of the vibration bands.

Table 1.3. Typical IR adsorption bands positions for HA powder (Journal of Materials sciences: materials in medicine, 1997, 8 (1), 1)[116]

Apatite, IR bands	Assignments
3570	O-H stretch
1615	H-O-H, adsorbed H_2O
1454-1414	C-O of CO_3 groups
Phosphate v3	1190-976
(vs)	1091
(vs)	1042
Phosphate v1 (m)	962
Phosphate v2(ms)	877
Phosphate v4	660-520
(m)	632
(vs)	602
(vs)	566
Phosphate v2 (w)	472

(c) Scanning Electron Microscopy method.

Scanning Electron Microscopy (SEM) is used in order to demonstrate crystal morphology, but cannot provide a definitive identification of the compound. This method is useful in determining the effect of substitutions on the morphology (crystal size and shape) of the apatite.

(d) Solid State Nuclear Magnetic Resonance.

The use of solid state phosphorus nuclear magnetic resonance (SSNMR) is a useful tool to detect the environment of the europium based on the side-bands attributed to the interaction between the phosphorus nucleus and the paramagnetic electron of europium.

(d) Compositional analysis

Two other methods are used to give information on the HA after identification: surface area analysis to assign the apatite porosity and thermogravimetry providing information on the thermal stability of different components of the calcified apatite.

The composition of the apatite can be determined also by elemental analysis with inductive coupled plasma atomic emission spectrometry (ICP). This analysis allows determination of the concentration of calcium and phosphate and thus, the Ca/P ratio. This method will not provide us with identification of the different phases present but it will only confirm the other results from XRD or IR analysis.

(e) Analytical methods used in this study.

Based on our study, other analysis methods have been used, such as Rietveld analysis based on the XRD data which would allow us to solve the crystal structure of the HA powder and get the position(s) of the calcium ions (or in our case, substituted europium ions) in the HA structure; luminescence studies to ascertain the environment of the europium as a substitute for Ca(II) and X-ray absorption fine structure (XAFS) to assign the distances between the europium and its surroundings atoms.

1.5- Metal and lanthanide ions substitution in Hydroxyapatite

1.5.1- Introduction

The apatite structure has been widely used as host lattice for luminescent ions. Two to three decades ago, Sr^{2+} and Mn^{2+} -coactivated calcium halophosphates[117-120] and Sb^{3+} in alkaline earth lanthanide apatite silicates[121] had already been used for application in fluorescent lamps. Later, several studies were concentrated on the making of the $M_5(PO_4)_3X$ type apatites with M = Ca, Sr, Ba, Pb and X=F, Cl, Br, or OH, for their technological importance as phosphor materials, laser hosts[122] and medical applications[49,123]. Lanthanide doped nanoparticles have attracted strong interest due to their luminescent properties and potential use as fluorescent labels. The incorporation of trivalent rare earth ions such as Nd^{3+} [124], Yb^{3+} [125,126], and Er^{3+} into apatite has revealed important spectroscopic properties which could be used in laser technology. Some Eu^{3+} doped apatite structures have also been reported in fluoroapatite[127], oxyapatites[128,129], strontium apatite [127,130-132] and hydroxyapatite[133].

Ions can often be found within the hydroxyapatite structure. This material has been used for several years in biological applications thanks to its ability to accept many ionic substitutions. The mineral composition of some biological tissue such as bone, teeth, and invertebrate skeleton are comprised of impure hydroxyapatites which plays various kinds of inorganic substances; it is why the importance to concentrate on modified or ion-substituted HA was addressed. Various doped hydroxyapatite were synthesized and characterized. The most encountered are Mg^{2+} [134], CO_3^{2-}, HPO_4^{2-} [62] fluoride [113] and silicon [135]which posses an important role in developing artificial bone. Lebugle *et al.*[48,49,136] has

investigated lanthanide doped calcium phosphates and their luminescent properties. Mayer and Webster [137] also investigated the incorporation of divalent ions Mg^{2+}, Zn^{2+} [138-141] and Sr^{2+} [142] and trivalent Ga^{3+} [143], Al^{3+} [144], Bi^{3+}, Y^{3+} and La^{3+} [145] in carbonated hydroxyapatite and hydroxyapatite[137]. The substitutions of these ions were observed to be beneficial to enhance the HA properties [62] by increasing bone formation and preventing bone resorption. For example yttrium oxide hydroxyapatite has been used as a bone repairing biomaterial in order to repair osteoshortage[146]. In another aspect, lead doped HA has been studied to solve the problem of lead poisoning in human due to environmental contamination[147,148]. Another type of apatite substitution involved lanthanides such as lanthanum [145,149,150], neodymium, dysprosium [151,150], samarium[150] and cerium[152]. Recently, Chakraborty et al. investigated Lu-177 doped HA as a viable radionuclide for liver cancer therapy; Lu-177 is a potentially good radiotherapeutic isotope due to its large scale production and its longer half live[153]. Also using HA as a drug delivery carrier, Eu-doped HA was prepared as template to investigate the drug storage/release properties[154].

1.5.2- Preparations of synthetic lanthanide-substituted HA or other CaPs

Whitlockite-like structures doped with europium ions have been synthesized following a solid state reaction method at 400°C [155,156]. Also, a europium-doped strontium HA crystallized powder has been prepared using a high-temperature solid state reaction for luminescence studies [132].

In order to get single crystals, the method of choice is the use of the hydrothermal conditions. Indeed, Fleet prepared single crystals of Ln-HA (Ln=La, Nd, Sm, Dy) using a standard cold-seal hydrothermal reaction[150] for crystallographic studies.

The most popular and easy way to prepare HA or substituted HA is the precipitation or liquid phase synthesis. A solution containing a mixture of calcium salt (calcium nitrate [49,142] or acetate) and lanthanide salt (lanthanide nitrate is added to a solution containing a phosphate salt (diammonium hydrogenophosphate) and a solution of ammonium hydroxide may be added to adjust the pH [142]. Two other alternative procedures can be used : Webster dripped calcium nitrate and ammonium phosphate into a dilute solution of ammonium hydroxide with the addition of the dopants in a solid nitrate form during this liquid phase synthesis [137] and Ternane used an aqueous solution of calcium oxide and europium oxide to which is added a solution of phosphoric acid[133].

1.5.3- Studies on calcium sites occupation by lanthanides

As HA can be a host for lanthanide ions, the position of these foreign ions within the HA structure is of interest. Two calcium sites are available for substitution, Ca1 and Ca2, in the $P6_3/m$ apatite structure. They differ in their sizes and stereochemical environments. The Ca1 ions are 9-fold coordinated with oxygen atoms in a CaO_9 polyhedron structure, whereas the Ca2 ions are seven-fold coordinated close to the OH- ions in the channels of this CaO_6A polyhedron structure (A= OH or F). The Ca2 form two triangles that are staggered of 60° angle from each other around the c axis.

In 1991, Hughes and Cameron reported the study of four Ln-doped apatites. They demonstrated that light lanthanides (La to Sm), as a group, showed a pronounced preference for Ca2 site in the apatite structure: Nd(III) could occupied either site and Pm and Sm could also substitute at the Ca1 site[157]. Other studies[158-160] on fluoroapatite (FAp) single lanthanide (La-FAp, Nd-FAp, Gd-FAp) or double lanthanide (La,Gd-FAp, Ce,Dy-

FAp, Pr,Er-FAp and Eu,Lu-FAp) substitution suggested a general preference for Ca2 site versus Ca1 site but the site occupancy ratios (Ln-Ca2/Ln-Ca1) decreased across the lanthanide series, in response to progressive minimization of volume strain[150]. This could be attributed to a special accommodation or structural change in apatite as the radius of the ions increases versus the effective size of the Ca2 site. Fleet suggested that the $Ca1O_6$ being a distorted trigonal prism Ca1 site does not accommodate ions that are either appreciably smaller or bigger than Ca^{2+} ion in F-apatite and HA. Also, both Fleet and Serret [161] found that the calcium site preferred for a lanthanide substitution was Ca2 site and that the Ca1 sites were occupied only with Ca^{2+}ions.

Substitution of Ln^{3+} for Ca^{2+} in the apatite structure requires concomitant altervalent substitution in order to maintain the charge balance. Blasse suggested that the charges were compensated by an oxygen ion O^{2-} on the fluorine site[128]. In the same way, Serret suggested the introduction of trivalent lanthanides into the HA through the transformation of OH^- to O^{2-} ions in order to maintain charge neutrality[149]. The idea was supported by Get'man who stated that in the absence of foreign ions, calcium substitution with Ln^{3+} is accompanied by hydroxyl group transformation into oxide ion O^{2-} [151].

The distribution of each lanthanide in Ca1 or Ca2 sites appeared to be more complicated. Beyond Sm, the lanthanide ions become too small for strain free substitution into Ca1 and enter Ca2.

1.5.4- Luminescence studies

As mention earlier, different ways to detect and identify the presence of HA can be achieved using different analytical methods, the most widely used being XRD and IR.

However, for Eu-doped HA samples, luminescence spectroscopy appears to be a good tool to detect and analyze the sample. The advantages for using europium as our lanthanide are many. First, europium emits light in the visible region of the spectrum which facilitates the monitoring of its luminescence with commercially available instruments; europium has been widely used in our laboratory and therefore is well-known and well-handled; and its principal emission bands are between 590 and 616 nm where biological media do not fluoresce. In theory, even though the f-f transition are Laporte forbidden, they become partially allowed as electronic dipole transitions where we get an admixtures of configurations of opposite sign[162].

Europium is one of the lanthanides, the most known one thanks to its strong emission intensity in the visible region when irradiated with UV-light [163]. Also, it was the first to be studied in solution. In the 1940's Freed *et al.*[164]discovered that europium luminescence intensity was solvent dependent[163]. Europium has a long life time that is on the order of milliseconds. Its life-time is also dependent upon the environment of europium which may quench the luminescence. The quenching effect was found to be inversely proportional to the energy gap between energy state and group state of the metal[162] and depends upon the oscillator to Ln(III) distance which has been established to be in the order of the second- and outer-sphere hydration values and emphasize the quenching effect of unbound water molecule. This deactivation of the luminescence from excited Ln^{3+} ions in solution occurs by a non-radiative vibrational energy transfer process due to high energy vibrational levels of the water molecule or of ligand oscillators [165]. Harmonic of N-H, C-H and C=O stretching vibrations can also have an impact on the luminescence but not as much as O-H oscillators which are the most effective quenchers in solution and solid state (Figure 1.7).

The corresponding deuterated oscillators are found to be less effective in the quenching of the lanthanide luminescence because of their lower frequency.

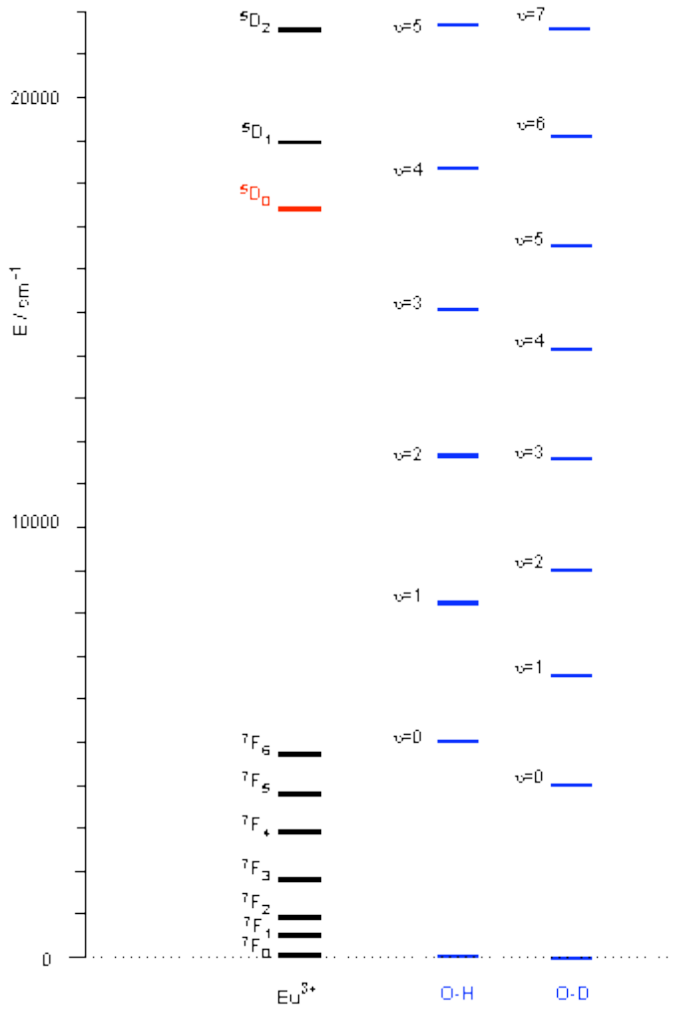

Figure 1.7. Energy level diagram of europium and the stretching harmonic of O-H and O-D oscillators (Applied Spectroscopy Reviews **2005**, *40*, 1-31)[1]

Therefore the substitution of H_2O by D_2O eliminates the deexcitation pathway and causes the increase of lifetime. Through this observation, Horrocks and Sudnick developed a method to measure the number of Ln-coordinated water molecule [166]. From a separate

measurement of life times in H_2O and D_2O solution they determine the number of coordinated water molecules, *q*:

$$q = A_{Ln}(\tau^{-1}_{H2O} - \tau^{-1}_{D2O})$$

where $A_{Eu} = 1.1$ and τ^{-1} also known as k values are in ms^{-1}.

Because lanthanides generally have long luminescence lifetimes, the decay signal can be separated from the background fluorescence signal. In order to do so, a time-gating technique is used, consisting of turning on the detector after the short lived fluorescence has decayed, leaving the long-lived lanthanide luminescence and suppressing the scattered light or luminescence background (Figure 1.8)

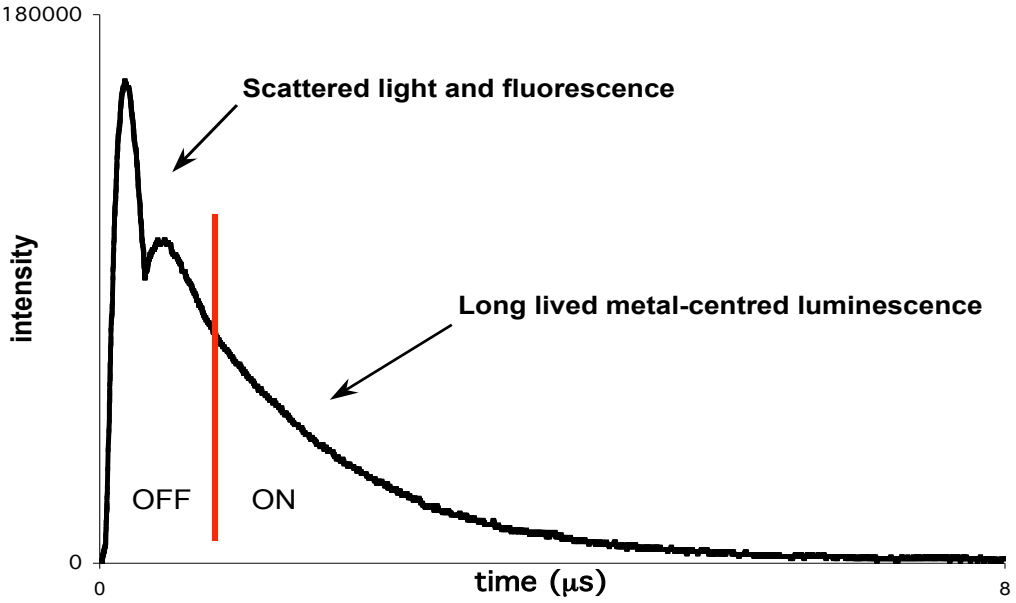

Figure 1.8. Graph indicating the procedure of time-grating (Applied Spectroscopy Reviews **2005**, *40*, 1-31)[1]

1.6- Objective and specific aims.

The objective of this thesis is to look at europium complexes as a useful tool in various domains. It could be for biological applications or electronic related areas. We will look at two kinds of adsorption using europium complexes: one as target molecules onto bone for bone cancer and one as photoluminescence component onto glass as luminescence amplificators. The important properties that make europium useful if its absorption in the visible region and its long life time. Chapter 2 may help elucidating the environment of lanthanide complexes after injection. Due to the relation of lanthanides to actinides, this study may also provide insight on the position of actinide based HA incorporation after an eventual actinide contamination. We chose europium (III) because it makes a good candidate for Ca-substitution in the apatite or hydroxyapatite framework due to its ionic size and luminescence properties. Occurrence of pure stoichiometric HA, $Ca_{10}(PO_4)_6.(OH)_2$ with Ca/P = 1.67, is not found in biological system. Biological apatite is considered as Ca deficient, non-stoichiometric (Ca/P < 1.67), "impure" apatite. In order to mimic closely the biological system, the precipitation synthetic method was the method of choice. In the first part of Chapter 2, we focused on europium doped hydroxyapatite, synthesized by precipitation reaction. This study allowed us to identify the position of the europium within the hydroxyapatite lattice thanks to different analytic and spectroscopic methods: elemental analysis, X-ray diffraction (XRD), Infra-red (IR), luminescence studies, X-ray absorption fine structure (XAFS), and other spectroscopic analysis (SEM, BSE and EDS). In the second part, we looked at two phosphonate ligands, EDTMP and DOTMP, complexed with europium and follow their adsorption to HA using mainly the luminescence analysis tool to monitor the change of environment as they adsorbed to bone

observing their different behaviors towards the adsorption where the influence of the ligand structure and the influence of biological media were addressed.

Chapter 3 focused on the behavior of three $Ln[\alpha_2\text{-}P_2W_{17}O_{61}]^{7-}$ (praseodymium, europium and ytterbium) towards countercations, pH, concentration of countercations and lanthanides. In Chapter 4, we looked at $Eu[\alpha_1\text{-}P_2W_{17}O_{61}]^{7-}$ (EuPOM) in a layer by layer deposition application with $Zn(phen)_3^{2+}$ (Zn(phen)) and its potential as a photoluminescence device.

1.7- References

(1) Faulkner, S.; Pope, S. J. A.; Burton-Pye, B. P. *Appl. Spec. Rev.* **2005**, *40*, 1-31.

(2) Davidson, R. S. *Chem. Soc. Rev.* **1996**, *25*, 241-253.

(3) Lauffer, R. B. *Chem. Rev.* **1987**, ***87***, 901-927.

(4) Caravan, P.; Ellison, J. J.; McMurry, T. J. *Chem. Rev.* **1999**, *99*, 2293.

(5) Alves, F. C.; Donato, P.; Sherry, A. D.; Zaheer, A.; Zhang, S.; Lubag, A. J. M.; Merritt, M. E.; Lenkinski, R. E.; Frangioni, J. V.; Neves, M.; Prata, M. I. M.; Santos, A. C.; de Lima, J. J. P.; Geraldes, C. F. G. C. *Investigative Radiology* **2003**, *38*, 750-760.

(6) Goeckeler, W. F.; Edwards, B.; Volkert, W. A.; Holmes, R. A.; Simon, J.; Wilson, D.; *J. Nucl. Med.* **1987**, *28*, 495-504.

(7) Chakraborty, S.; Das, T.; Banerjee, S.; Chaudhari, P. R.; Sarma, H. D.; Venkatesh, M.; Pillai, M. R. A. *Nucl. Med. Commun.* **2004**, *5*, 1169-1176.

(8) Volker, W. A.; Simon, J.; Ketrin, A. R.; Holmes, R. A.; Lattimer, L. C.; Corwin, L. A. *Drugs of the Future* **1989**, *14*, 799.

(9) Volkert, W. A.; Hoffman, T. J. *Chem. Rev.* **1999**, *99*, 2277.

(10) Jakupec, M. A.; Unfried, P.; Keppler, B. K. *Rev. Physiol Biochem. Pharmacol* **2005**, *153*, 101

(11) Evans, C. H. *Trends Biochem. Sci.* **1983**, 445.

(12) Albaaj F.; Hutchison A. J. *Expert Opin. Pharmacother.* **2005**, *6*, 319.

(13) Fricker, S. P. *Chem. Soc. Rev.* **2006**, *35*, 524-533.

(14) Volker, W. A.; Goeckeler, W. F.; Ehrhardt, G. J.; Ketrin, A. R. *J. Nucl. Med.* **1991**, *32*, 174.

(15) *Radio-lanthanides in nuclear medicine.* ; Sigel H, ed.; Ro¨sch, F.; Forssell-Aronsson, E., Eds.; Marcel Dekker, Inc.: New York, NY, **2004**; Vol. 77-108.

(16) Nelson, K.; Vause, P. E., Jr.;; Koropova, P. *Mayo Clinic Jacksonville, Jacksonville, FL, USA Health Physics* **2008**, 95.

(17) Nijsen, J. F. W.; van het Schip, A. D.; Hennink, W. E.; Rook, D. W.; van Rijk, P. P.; de Klerk, J. M. H. *Curr. Med. Chem* **2002**, 73.

(18) Koppe, M. J.; Bleichrodt, R. P.; Soede, A. C.; al., e. *J Nucl Med.* **2004**, *45*, 1224-1232.

(19) Lambert B.; Van de Wiele C. *Eur J Nucl Med Mol Imaging* **2005**, *32*, 980-9.

(20) Khodjibekova, M.; Szyszko, T.; Khan, S.; Nijran, K.; Tait, P.; Al-Nahhas, A. *Department of Nuclear Medicine, Hammersmith Hospital, London, UK. Reviews on Recent Clinical Trials* **2007**, *2*, 212.

(21) *J. Mater. Sci: Mater. Med.* **2008**, *19*, 1225-1233.

(22) Pillai, M. R. A.; Chakraborty, S.; Das, T.; Venkatesh, M.; Ramamoorthy, N. *Appl Radiat Isot* **2003**, *59*, 109-18.

(23) Schmitt, A.; Bernhardt, P.; Nilsson, O.; al., e. *J Nucl Med.* **2004**, *45*, 1542-1548

(24) de Jong M.; Breeman W.A.; Bernard B.F. *Int J Cancer* **2001**, *92*, 628-633.

(25) Bodei, L.; Cremonesi, M.; Ferrari, M.; Pacifici, M.; Grana, C.; Bartolomei, M.; Baio, S.; Sansovini, M.; Paganelli, G. *Eur J Nucl Med Mol Imaging* **2008**, *35*, 1847-1856.

(26) Kwekkeboom, D.J.; Bakker, W.H.; Kam, B.L. *Eur J Nucl Med Mol Imaging.*

2003, *30*, 417-422.

(27) Kwekkeboom, D.J.; Bakker, W.H.; Kooij, P.P. *Eur J Nucl Med.* **2001**, *28*, 1319-1325.

(28) Teunissen, J. J.; Kwekkeboom, D. J.; Krenning, E. P. *J Clin Oncol.* **2004**, *22*, 2724-2729.

(29) Forrer, F.; Uusija¨rvi, H.; Storch, D.; Maecke, H.; Mueller-Brand, J. *J Nucl Med* **2005**, *46*, 1310.

(30) Breitz, H. B.; Wendt III, R. E.; Stabin, M. S.; Shen, S.; Erwin, W. D.; Rajendran, J. G.; Eary, J. F.; Durack, L.; Delpassand, E.; Martin, W.; Meredith, R. F. *Journal of Nuclear Medicine* **2006**, *47*, 534.

(31) Volkert, W. A.; Goeckeler, W. F.; Ehrhardt, J.; Ketring, A. R. *J. Nucl. Med.* **1991**, *32*, 174-185.

(32) Neves, M.; Kling, A.; Lambrecht, R. M. *Appl. Radiat. Isot.* **2002**, *57*, 657-664.

(33) Maini, C. M.; Bergomi, S.; Romano, L.; Scuito, R. *Eur. J. Nucl. Med. Mol. Imaging* **2004**, *31 supp 1*, 171.

(34) Porter, A. T.; Ben-Josef, E.; Davis, L. *Curr Opin Oncol* **1994**, *6*, 607.

(35) Serafini, A. N. *J. Nucl. Med.* **2001**, *42*, 895-906.

(36) Rajendran, J. G.; Eary, J. F.; Bensinger, W.; Durack, L. D.; Vernon, C.; Fritzberg, A. *J. Nucl. Med.* **2002**, *43*, 1383-1390.

(37) Breitz, H.; Wendt, R.; Stabin, M.; Boucher, L.; Wessels, B. *Cancer Biother. Radio.* **2003**, *18*, 225-230.

(38) Majali, M. A.; Saxena, S. K.; Joshi, S. H.; Unni, P. R.; Ramamoorthy, N. *Nucl. Med. Commun.* **2001**, *22*, 97-103.

(39) Das, T.; Chakraborty, S.; Banerjee, S.; Samuel, G.; Sarma, H. D.; Venkatesh, M.; Pillai, M. R. A. *J. Label. Compd. Radiopharm.* **2003**, *46*, 197-209.

(40) de Murphy, C. A.; Tendilla, J. I.; Monroy-Guzma´n, F.; Pedraza-Lo´pez, M.; Aldama- Alvarado, K. *Appl. Radiat. Isot.* **2004**, *61*, 1227-1233.

(41) Kairemo, K. J. *Acta Oncol.* **1996**, *35*, 343-355.

(42) Dadachova, E.; Mirzadeh, S.; Smith, S. V.; Knapp Jr., F. F.; E.L., H. *Appl. Radiat. Isot.* **1997**, *48*, 477-481.

(43) Fani, M.; Vranjes, S.; Archimandritis, S. C.; Potamianos, S.; Xanthopoulos, S.; Bouziotis, P.; Varvarigou, A. D. *Appl. Radiat. Isot.* **2002**, *57* 665-674.

(44) Hu, F.; Cutler, C. S.; Hoffman, T.; Sieckman, G.; Volkert, W. A.; Jurisson, S. S. *Nucl. Med. Biol.* **2002**, *29*, 423-430.

(45) Li, W. P.; Smith, C. J.; Cutler, C. S.; Hoffman, T. J.; Ketring, A. R.; Jurisson, S. S. *Nucl. Med. Biol.* **2003**, 241-251.

(46) Pedraza-López, M.; Ferro-Flores, G.; de Murphy, C.; Tendilla, J.; Villanueva-Sánchez, O. *Nucl Med Commun.* **2004** *25*, 615-21.

(47) Evans, C. H. In *Handbook of Experimental Pharmacology*; Springer-Verlag, Ed. Berlin, 1988.

(48) Lebugle, A.; Pelle, F.; Charvillat, C.; Rousselota, I.; Chane-Ching, J. Y. *Chem. Commun.* **2006**, 606-608.

(49) Doat, A.; Fanjul, M.; Pelle, F.; Hollande, E.; Lebugle, A. *Biomaterials* **2003**, *24*, 3365-3371.

(50) Mondry, A.; Janicki, R. *Dalton Transactions* **2006**, 4702-4710.

(51) De Witt, G. C.; May, P. M.; Webb, J.; and Hefter, G. *Biomaterials* **1996**, *9*, 351.

(52) Kotek, J.; Kálmán, F. K.; Hermann, P.; Brücher, E.; Binnemans, K.; Luke, I. *Eur. J. Inorg. Chem.* **2006**, *10*, 1976-1986.

(53) Kálmán, F. K.; Király, R.; Brücher, E. *Eur. J. Inorg. Chem.* **2008**, 4719.

(54) Dischino, D. D.; Delaney, E. J.; Emswiler, J. E.; Gaughan, G. T.; Prasad, J. S.; Srivastava, S. K. *Inorg. Chem.* **1991** *30*, 1265.

(55) Desreux, J. F. *Inorg. Chem.* **1980**, ***19***, 1319.

(56) Sherry, A. D.; Cacheris, W. P.; Nickle, S. K. *Inorg. Chem.* **1987**, *26*, 958.

(57) Sherry, A. D.; Ren, J.; Huskens, j.; Brücher, E.; Tóth, É.; Geraldes, C. F. C. G.; Castro, M. M. C. A.; Cacheris, W. P. *Inorg. Chem.* **1996**, *35*, 4604–4612.

(58) Rodan, G. A. *Proc. Natl. Acad. Sci. USA* **1998**, *95*, 13361-13362.

(59) Krabbe S.; Transbol I.; C., C. *Archives of Disease in Childhood* **1982**, *57*, 359-363.

(60) Teti, A.; Zallone, A. *Bone* **2009**, *44*, 11-16.

(61) Kay, M. I.; Young, R. A.; Posner, A. S. *Nature* **1964**, *204*, 1050.

(62) LeGeros, R. Z. *Monographs in Oral Science* **1991**, *15*.

(63) Talmaga, R. V. *Am. J. Anat.* **1970**, *129*, 467.

(64) Bouleenc, X.; Marti, E.; Joyeux, H.; al., e. *Biochem. Pharmacol.* **1993**, *46*, 1591.

(65) Fleisch, H. R.; Russell, G. G.; Francis, M. D. *Science* **1969**, *165*, 1262-1264.

(66) Fleisch, H. R.; Russell, G. G.; Straumann, N. *Nature* **1966**, *212*, 901.

(67) Russell, R. G. R. *Bone* **2007** *40*, S21-S25.

(68) Nancollas, G. H.; Tanga, R.; Phipps, J.; Hennemana, Z.; Guldea, S.; Wua, W.; Mangooda, A.; Russell, R. G. G.; Ebetin, F. H. *Bone* **2006**, *38*, 617-627.

(69) Pandit-Taskar, N.; Batraki, M.; Divgi, C. R. *J. Nucl. Med.* **2004**, *45*, 1358-1365.

(70) *Jarvis, C. I.*; *Morin, A. K.*; *Lynch, A. M. Clinical Reviews in Bone and Mineral Metabolism* **2005**, *3*, 3-18.

(71) Fogelman, I.; Bessent, R. G.; Turner, J. G.; Citrin, D. L.; Boyle, I. T.; Greig, W. R. *J. Nucl. Med.* **1978**, *19*, 270.

(72) Hirabayashi, H.; Takahashi, T.; Fujisaki, J.; al., e.; *J Control Release* **2001**, *70*, 183.

(73) Smith, R. L.; *Handbook of experimental pharmacology: concepts in biochemical pharmacology*; Brodie BB, Gillette JR, ed.; Springer: Berlin, **1971**; Vol. 28.

(74) Fujisaki, J.; Tokunaga, Y.; Sawamoto, T.; al., e. *J drug Target* **1996**, *4*, 117.

(75) Ketrin, A. R.; Volker, W. A.; Simon, J.; Goeckeler, W. F.; Troutner, D. E.; J., N. E. G. *J. Nucl. Med.* **1990**, *31*, 767.

(76) Li, W. P.; Ma, D. S.; Higginbotham, C.; Hoffman, T.; Ketring, A. R.; Cutler, C. S.; Jurisson, S. S. *Nuclear Medicine and Biology* **2001**, *28*, 145-154.

(77) Simon, J.; Wilson, D. A.; Baughman, S. A.; Leggett, D.; Goeckeler, W. F.; Stringham, L.; Volkert, W. A.; McMillian, K. *Proc. VII Intl. Symp. Radiopharm. Chem.* **1988**, *7*, 359.

(78) Serafini, A. N.; Houston, S. J.; Resche, I.; Quick, D. P.; Grund, F. M.; Ell, P. J.; Bertrand, A.; Ahmann, F. R.; Orihuela, E.; Reid, R. H.; Lerski, R. A.; Collier, B. D.; McKillop, J. H.; Purnell, G. L.; Pecking, A. P.; Thomas, F. D.; Harrison, K. A. *J. Clin. Oncol.* **1998**, *16*, 1574.

(79) Majkowska, A.; Neves, M.; Antunes, I.; Bilewic, A. **2009**, *67*, 11.

(80) Vitha, T.; Kubicek, V.; Hermann, P.; Vander Elst, L.; Muller, R. N.; Kolar, Z. I.; Wolterbeek, H. T.; Breeman, W. A. P.; Lukes, I.; Peters, J. A. *J Med Chem* **2008**, *51*, 677-83.

(81) Försterová, M.; Jandurová, Z.; Marques, F.; Gano, L.; Lubal, P.; Vanek, J.; Hermann, P.; Santos, I. *J. Inorg. Biochem.* **2008**, *102*, 1531-40.

(82) Rill, C.; Kolar, Z. I.; Kickelbick, G.; Wolterbeek, H. T.; Peters, J. A. *Langmuir* **2009**, *25*, 2294-2301.

(83) Russell, R. G. G.; Rogers, M. J. *Bone* **1999**, *25*, 97.

(84) Josse, S.; Faucheux, C.; Soueidan, A.; Grimandi, G.; Massiot, D.; Alonso, B.; Janvier, P.; Laib, S.; Guicheux, J.; Bujoli, B.; Bouler, J. M. *Key Engineering Materials* **2005**, *284-286*, 399-402.

(85) Fleisch, H. *Bisphosphonates in Bone Disease,*; 4th Ed.; Academic Press: London,, 2000.

(86) Kubíek, V.; Rudovský, J.; Kotek, J.; Hermann, P.; Vander Elst, L.; N. Muller, R.; Kolar, Z. I.; Wolterbeek, H. T.; Peters, J. A.; Lukeš, I. *J. Am. Chem. Soc.* **2005**, *127*, 16477.

(87) Zeevaart, J. R.; Jarvis, N. V.; Louw, W. K. A.; Jackson, G. E.; Cukrowski, J.; Mouton, C. J. *J. Inorg. Biochem.* **1999**, *73*, 265-272.

(88) Adzamli, I. K.; Gries, H.; Johnson, D.; Blau, M. *J. Med. Chem.* **1989**, *32*, 139-144.

(89) Adzamli, I. K.; Johnson, D.; Blau, M. *InVest. Radiol.* **1991**, *26*, 143-148.

(90) Adzamli, I. K.; Blau, M.; Pfeffer, M. A.; Davis, M. A. *Magn. Reson.Med.* **1993**, *29*, 505-511.

(91) Charmaine de Witt, G.; May, P. M.; Webb, J.; Hefter, G. *BioMetals* **1996**, *9*, 351-361.

(92) Zhu, S.; Xiao, D.; Han, X. *Zhonghua Fangshe Yixue Yu Fanghu Zazhi* **1999**, *19*, 307-309.

(93) Zhu, S.; Xiao, D.; Wu, Y. *Tongweisu* **2002**, *15*, 148-150.

(94) Chirby, D.; Franck, S.; Troutner, D. E. *Appl. Radiati. Isot.* **1988**, *39*, 495-499.

(95) Luo, S.; Qiao, J.; Pu, M.; Liu, Z.; Zhao, P.; Fu, Y. *Nuclear Science and Techniques* **1995**, *6*, 241-245.

(96) Goeckeler, W. F.; Troutner, D. E.; Volkert, W. A.; Edwards, B.; Simon, J.; Wilson, D. *Nucl. Med. Biol.* **1986**, *13*, 479.

(97) Chambers, M. D., Texas A&M University: College Station, 1995.

(98) Ioku, K.; Yamauchi, S.; Fujimori, H.; S., G.; Yoshimura, M. *Solid State Ionics* **2002**, *151*, 147-150.

(99) Liu, J.; Ye, X.; Wang, H.; Zhu, M.; B., W.; Yan, H. *Ceramics International* **2002**, ***121***, 59-64.

(100) RamachandraRao, R.; Roopa, H. N.; Kannan, T. S. *Journal of Materials Science-Materials in Medicine* **1997**, *8*, 511-518.

(101) Afshar, A.; Ghorbani, M.; Ehsani, N.; Saeri, M. R.; Sorrell, C. C. *Materials and Design* **2003**, ***24***, 197-202.

(102) Dorozhkina, E. I.; Dorozhkina, S. V. *Colloids and Surfaces* **2002**, ***203***, 237-244.

(103) Bezzi, G.; Celotti, G.; Landi E.; La Torretta, T. M. G.; Sopyan, I.; Tampieri, A. *Materials Chemistry and Physics* **2003**, ***78***, 816-824

(104) Yamashita, K.; Arashi, T.; Kitagaki, K.; S., Y.; Umegaki, T. *Journal of American Ceramic Society* **1994**, ***77***, 2401-2407.

(105) Silva, C. C.; Pinheiro, A. G.; Miranda, M. A. R.; Góes, J. C.; Sombra, A. S. B. *Solid State Sciences* **2003**, ***5*** 553-558.

(106) Suchanek, W. L.; Shuk, P.; Byrappa, K.; Riman, R. E.; TenHuisen, K. S.; Janas, V. F. *Biomaterials* **2002**, ***23***, 699-710.

(107) Nakamura, S.; Isobe, T.; Senna, M. *Journal of Nanoparticle Research* **2001**, *3*, 57-61.

(108) Lim, G. K.; Wang, J.; Ng, S. C.; Chew, C. H.; Gan, L. M. *Biomaterials* **1997**, *18,* 1433-1439.

(109) Masanori, K.; Ikomaa, T.; Itohb, S.; Matsumotob, H. N.; Koyamab, Y.; Takakudab, K.; Shinomiyab, K.; Tanakaa, J. *Composites Science and Technology* **2004**, *64*, 819-825.

(110) Vogel, G. L.; Carey, C. M.; Chow, L. C.; Brown, W. E. *J. Dent. Res.* **1987**, *66*, 1691.

(111) Leung, Y.; Walters, M. A.; Legeros, R. Z. *Spectrochimica Acta, Part A: Molecular and Biomolecular Spectroscopy* **1990**, *46A*, 1453.

(112) Antonakos, A.; Liarokapis, E.; Leventouri, T. *Biomaterials* **2007**, *28*, 3043.

(113) Wei, M.; Evans, J. H.; Bostrom, T.; Grondahl, L. *J. Materials science: materials in medicine* **2003**, *14*, 311.

(114) Fowler, B. O. *Inorg. Chem.* **1974**, *13*, 207.

(115) Rintoul, L.; Wentrup-Byrne, E.; Suzuki, S.; Grondahl, L. *J. Mater. Sci.: Mater. Med.* **2007**, *18*, 1701.

(116) Rehman, I.; Bonfield, W. *Journal of materials sciences: materials in medicine*

1997, *8*, 1.

(117) Rappalardo, R. G.; Walsh, J.; Hunt, R. B. *J. Electrochem. Soc.* **1983**, *130*, 2087.

(118) Ryan, F. M.; Hopkins, R. H.; Warren, R. W. *Journal of Luminescence* **1972**, *5*, 313-33.

(119) Ryan, F. M.; Vodoklys, F. M. *Journal of the Electrochemical Society* **1971**, *118*, 1819-23.

(120) Ryan, F. M.; Vodoklys, F. M. *Journal of the Electrochemical Society* **1971**, *118*, 1814-19.

(121) Wanmaker, W. L.; ter Vrugt, J. W.; G., V. J. *J. Solid State Chem.* **1971**, *3*, 452.

(122) Budin, J. P.; Michel, J. C.; Auzel, F. *J. Appl. Phys.* **1979**, *50*, 641.

(123) Mondejar, S. P.; Kovtun, A.; Epple, M. *Journal of Materials Chemistry* **2007**, *17*, 4153-4159.

(124) Ryan, F. M.; Warren, R. W.; Hopkins, R. H.; Murphy, J. *Journal of the Electrochemical Society* **1978**, *125*, 1493-8.

(125) DeLoach, L. D.; Payne, S. A.; Krupke, W. F.; Smith, L. K.; Kway, W. L.; Tassano, J. B. *OSA Proc. Adv. Solid-State Lasers, Proc. Top. Meet.* **1993**, 188-91.

(126) DeLoach, L. D.; Payne, S. A.; Smith, L. K.; Kway, W. L.; Chase, L. L.; Krupke, W. F. *OSA Proc. Adv. Solid-State Lasers* **1992**, 293-5.

(127) Jagannathan, R.; Kottaisamy, M. *Journal of Physics: Condensed Matter* **1995**, *7*, 8453-66.

(128) Blasse, G. *Journal of solid state chemistry* **1975**, *14*, 181-184.

(129) El Ouenzerfi, R.; Panczer, G.; Goutaudier, C.; Cohen-Adad, M. T.; Boulon, G.;

Trabelsi-Ayedi, M.; Kbir-Ariguib, N. *Optical Materials (Amsterdam, Netherlands)* **2001**, *16*, 301-310.

(130) Kubota, S.; Stanger, R. L.; Suzuyama, Y.; Yamane, H.; Shimada, M. *Journal of the Electrochemical Society* **2002**, *149*, H134-H137.

(131) Taitai, A.; Lacout, J. L. *Journal of Physics and Chemistry of Solids* **1989**, *50*, 851-5.

(132) El Ouenzerfi, R.; Kbir-Ariguib, N.; Trabelsi-Ayedi, M.; Piriou, B. *Journal of Luminescence* **1999**, *85*, 71-77.

(133) Ternane, R.; Trabelsi-Ayedi, M.; Kbir-Ariguib, N.; Piriou, B. *Journal of Luminescence* **1999**, *81*, 165-170.

(134) Tampieri, A.; Cellotti, G.; Landi, E.; Sandri, M. *Key Engineering Materials* **2004**, *264-268*, 2051.

(135) Leventouri, T.; Bunaciu, C. E.; Perdikatsis, V. *Biomaterials* **2003**, *24*, 4205-4211.

(136) Doat, A.; Pelle, M.; Gardant, N.; Lebugle, A. *J. Solid State Chem.* **2004**, *177*, 1179.

(137) Webster, T. J.; Massa-Schlueter, E. A.; Smith, J. L.; Slamovich, E. B. *Biomaterials* **2004**, *25*, 2111-2121.

(138) Mayer, I.; Apfelbaum, F.; Featherstone, J. D. B. *Archives of Oral Biology* **1994**, *39*, 87-90.

(139) Mayer, I.; Cohen, S.; Gdalya, S.; Burghaus, O.; Reinen, D. *Materials Research Bulletin* **2008**, *43*, 447-452.

(140) Mayer, I.; Cuisinier, F. J. G.; Gdalya, S.; Popov, I. *Journal of Inorganic Biochemistry* **2008**, *102*, 311-317.

(141) Mayer, I.; Schlam, R.; Featherstone, F. D. B. *Journal of Inorganic Biochemistry*

1997, *66*, 1-6.

(142) Bigi, A.; Boanini, E.; Capuccini, C.; Gazzano, M. *Inorganica chimica Acta* **2007**, *360*, 1009.

(143) Cuisinier, F. J. G.; Voegel, J. C.; Apfelbaum, F.; Mayer, I. *Journal of Crystal Growth* **1992**, *125*, 1-6.

(144) Mayer, I.; Cohen, H.; Voegel, J. C.; Cuisinier, F. J. G. *Journal of Crystal Growth* **1997**, *172*, 219-225.

(145) Mayer, I.; Layani, J. D.; Givan, A.; Gaft, M.; Blanc, P. *Journal of Inorganic Biochemistry* **1999**, *73*, 221-226.

(146) Qiu, J.; Zhang, J.; Zhang, M.; Chen, Z. *Sheng Wu Yi Xue Gong Cheng Xue Za Zhi* **1998**, *15*, 26.

(147) Ellis D.E.; Terra J.; Warschkow O.; Jiang M.; Gonzalez G. B.; Okasinski J.S.; Bedzyk M.J.; Rossi A.M.; JG, E. *Phys. Chem. Chem. Phys* **2006**, 967.

(148) Pizzala H.; Caldarelli S.; Eon J.-G.; Malta Rossi A.; Laurencin D.; E., S. M. *J. Am. Chem. Soc.* **2009**, *131*, 5145-5152.

(149) Serret A.; Cabanas M.V.; Vallet-Regi M. *Chem. Mater.* **2000**, *12*, 3836.

(150) Fleet M.; Liu X.; Pan Y. *J. Solid State Chemistry* **2000**, *149*

(151) Get'man E.I.; Loboda S. N.; Tkachenko T.V.; Ignatov A.V.; Zabirko T. F. *Functional Materials* **2005**, *12*.

(152) Feng Z.; Liao Y.; Ye M. *J. Mater. Sci. Mater Med.* **2005**, *16*, 417-21.

(153) Chakraborty, S.; Das, T.; Sarma, H.; Venkatesh, M.; Banerjee, S. *Nucl. Med. Biol.* **2008**, *35*, 589-97.

(154) Piaoping Yang; Zewei Quan; Chunxia Li; Xiaojiao Kang; Hongzhou Lian; Jun Lin *Biomaterials* **2008**, *29*, 4341.

(155) Lazoriak B. I.; Golubev V. N.; Salmon R.; Parent C.; Hagenmuller P. *Eur. J. Solid State Inorg. Chem.* **1989**, *26*, 455.

(156) Lazoryak, B. I.; Strunenkova, T. V.; Vovk, E. A.; Mikhailin, V. V.; Shpinkov, I. N.; Romanenko, A. Y.; Schekoldin, V. N. *Material Research Bulletin* **1996**, *31*, 665.

(157) Hughes, J. M.; Cameron, M.; Mariano, A. N. *American Mineralogist* **1991**, *76*, 1165.

(158) Fleet, M. E.; Pan, Y. *J. Solid State Chem.* **1994**, *111*, 78.

(159) Fleet, M. E.; Pan, Y. *Am. Miner.* **1995**, *80*, 329.

(160) Fleet, M. E.; Pan, Y. *Am. Miner.* **1997**, *82*, 870.

(161) Serret, A.; Cabanas, M. V.; Vallet-Regi, M. *Chem. Mater.* **2000** *12* 3836.

(162) Faulkner S.; Pope S.J.A.; Burton-Pye B. *Applied Spectroscopy Reviews*, *39*, 1-35.

(163) Weissman, S. I. *J. Chem. Phys.* **1942**, *10*, 214.

(164) Freed, S.; Weissman, S. I.; Fortress, F. E.; and Jacobson, H. F. *J. Chem. Phys.* **1939**, *7*.

(165) Parker D.; Dickins R. S.; Puschmann H.; and, C. C.; Howard J.A.K. *Chem. Reviews.* **2002**, *102*, 1977–2010.

(166) de W. Horrocks, W.; and Sudnick D.R. *J. Am. Chem. Soc.* **1979**, *101*, 334.

Chapter 2: Europium incorporation into HA and Europium complexes Adsorption onto HA

2.1- Introduction

As life expectancy increases, the focus in oncology research has shifted towards metastatic cancer including bone cancer. New therapy methods have been developed involving the use of bisphosphonates for pain palliation but also radiotherapy using radioactive lanthanide complexes, more especially, lanthanideEDTMP or lanthanideDOTMP. The two most known complexes are the ^{153}SmEDTMP and ^{166}HoDOTMP for treating bone cancer and myeloma respectively. For treating bone cancer, the unknown factor, when using Sm-153(EDTMP), is the behavior of the complex after it adsorbed to bone. In this chapter we are using HA as a mimic to bone. HA is the main mineral component of bone. It has been widely synthesized and characterized by various research groups (see chapter 1 section 1.4 and 1.5). Also, doped HA with various ions and metal ions have been reported in order to elucidate their incorporation to the robust framework of HA.

The first part of the study was concerned with the incorporation of europium in HA to better understand the mechanism for the lanthanide ligand complex when adsorbed on HA. If this lanthanide transchelate from the ligand, the pursue of its location and environment is desirable. The second part of the study was concerned with the actual adsorption of the lanthanide ligand to HA; specifically, the ligands EDTMP and DOTMP complexed with europium.

2.2- Experimental section

2.2.1- Materials and samples preparation

Nanopure water was obtained from a Millipore Reverse Osmosis Direct-Q System. The conductivity was greater than 18 Megaohm.

$Eu(NO_3)_3$ and $EuCl_3$ were purchased from Aldrich, EDTMP was synthesized by Alltech. The EDTMP was purchased from University of Missouri and the DOTMP was purchased from Macrocyclics. The Eu(III) concentrations were determined by complexometric titration using xylenol orange as an indicator and EDTA (0.1M) as the complexing agent [1]. HA fast flow was purchased from Fluka (73.9 m^2/g)

Europium doped hydroxyapatite

The synthesis of HA and Eu(III) doped HA was developed by Professor Raquel Z. LeGeros of the NYU school of Dentistry.

Preparation of HA. 250 mL solution of $Ca(Ac)_2$ (0.05 M) was added dropwise to a stirring solution of 650 mL of water and 100 mL of Na_2HPO_4 (0.1 M, 0.01 mol) maintained at 90°C. After the addition of the Ca-containing solution was completed, the reaction was continued for another 3 hours at the same temperature with continuous stirring. The precipitate was filtered by vacuum filtration, rinsed with double distilled water and dried in an oven over night at 120°C. The pH of the filtrate was measured as 5.6. The dried precipitate was characterized using X-ray diffraction on a Philips X'Pert X-ray diffractometer to determine its phase composition and structure and determine crystallinity (crystal size). BET was used to determine specific surface area. Specific surface area was determined to be 56.1 and 22 m^2/g using N_2 BET measurement.

The samples of europium doped HA were prepared as follows. A solution of 650 mL of water and 100 mL of Na_2HPO_4 (0.1 M, 0.01 mol) was placed in a one liter Erlenmeyer flask and heated whilst stirring in an oil bath at 90°C. A 200-250 mL solution of $Ca(OAc)_2$ (0.05 M) and 10 to 50 mL solution of $Ln(NO_3)_3$ (0.05 M) was added to the latter solution dropwise via a separatory funnel over a 2 hours period (see Table 2.1). After complete addition the mixture was stirred and heated for another 3 hours. The precipitate formed was isolated by vacuum filtration and stored in an oven over night at 120 °C. The filtrate was tested with a pH of 5.6. The solids were characterized by ICP-AA, X-ray powder diffraction, IR, luminescence and SSNMR.

Table 2.1. Composition reaction of europium doped HA samples preparation.

Eu content / mL	1%	5%	9.5%	13%	16.8%	18.2%	25%
$Eu(NO_3)_3$ (0.05 mM)	2.4	10.5	22	30	40	44.5	50
$Ca(OAc)_2$ (0.05 mM)	200	200	200	200	200	200	200
Na_2HPO_4 (0.1 mM)	100	100	100	100	100	100	100
H_2O	650	650	650	650	650	650	650

EuEDTMP and Eu(DOTMP) preparation

Europium-EDTMP was prepared as follows. In a 20 mL vial EDTMP was dissolved in water with NaOH and adjust to pH 9. A solution of $EuCl_3$ (1:1 eq) was added and the pH adjusted to 9. The mixture was stirred in an oil bath at 90 ^{o}C for 2 hours for EuEDTMP and overnight for EuDOTMP. The solution was evaporated to dryness. The residue was checked by ^{31}P NMR to verify purity: one peak at 53 ppm for EuEDTMP[2] and one peak at 46 ppm for EuDOTMP at pH = 7.4, which are in agreement with Mondry[2] and Sherry[3] showing a fast proton exchange at this pH.

Phosphate buffer was prepared as follows. One liter of pH 7.4 phosphate buffer was prepared with 100 mM NaCl (5.84 g, 100 mmol), 40 mM KCl (3 g, 40 mmol), 4.3 mM Na_2HPO_4 (1.53 g, 4.3 mmol) and 1.4 mM KH_2PO_4 (0.19 g, 1.4 mmol).

Tris Buffer was prepared as follows: 1.51 g of THAM ($C_4H_{11}NO_3$) dissolved into 250 mL of water and pH adjusted to7.4 if needed with HCl.

Europium complex solutions were prepared as follows: The residue was dissolved in the TRIS (or phosphate) buffer. This solution was filtered by gravity filtration, diluted in a 100 mL volumetric flask with TRIS (or phosphate) buffer to obtain a 12 M solution and adjusted to pH 7.4.

EuEDTMP and EuDOTMP adsorbed to HA

Method using TRIS buffer

EuEDTMP adsorption to synthetic HA using phosphate buffer: an aliquot of 25 mL of the complex solution was added to 15 mg, 30 mg, 60 mg and 300 mg of HA. This mixture was shaken vigorously manually for 5 min and then put on a shaker overnight. The mixture was then filtered and washed 3 times with distilled water.

Method using phosphate buffer

This adsorption method followed the procedure of Drobny.[4] The hydroxyapatite, synthesized in the laboratory, was suspended in 25 mL buffer solution (0.05 M, pH 7.4). The Eu-EDTMP solution (12 M) was then added and the solution adjusted to pH 7.4 with HCl. The suspension was shaken for 5 min vigorously manually then was put on a shaker for 2 hours at speed 100-130. The resulting adsorbed HA was separated from the supernatant containing the unbound Eu-EDTMP by centrifugation. The pellet was washed 3 times with buffer solution and then frozen with liquid nitrogen and lyophilized.

Europium-DOTP adsorbed to HA samples were prepared similarly to the EuEDTMP adsorbed to HA samples using phosphate buffer.

2.2.2- Characterization of the synthetic preparations

Surface area characterization. Surface area was measured by BET method using N_2 on a Tristar 3000 surface area and porosity analyzer (Micromeritrics).

Infrared measurements. Fourier transform infrared spectrometer (FT-IR) (Nicolet Magna IR 550 Spectrometer Series II) analyses were made on Eu-HA powder pressed into a pellet. The pellets were prepared by mixing 1mg Eu-HA powder with 250 mg KBr (IR grade) and pressed at 10,000 psi using a hydraulic press (Carver laboratory press, mode C, Ser.No.33000-577, Fred S. Carver INC). The scan covered the range from 4000 to 400 cm^{-1}. The absorption bands were identified based on: hydroxyl stretch H-O-H (adsorbed H_2O and OH group) band at 3200 to 3400 cm^{-1}, O-H (hydroxyl) band at about 630 cm^{-1}, the v_1 P-O (PO_4 groups) bands at about 960 to 1200 cm^{-1}, v_4 P-O bands at about 500 to 600 cm^{-1} (at about 604 cm^{-1} and 561 cm^{-1}).

Elemental analysis by ICP. Elemental analyses were carried out using inductive coupled plasma atomic emission spectrometry (Spectroflame M120E). **(i) Standard Solution Preparation.** The standard solutions of P (1.5, 3, 4, 6, 8.5 ppm), Eu (0.5, 1, 2, 4, 7, 10 ppm), Ca (1, 3, 7, 10, 14, 20, 30 ppm) were prepared by diluting a 1000 ppm ICP standard solution (GFS Chemicals, Inc.) with distilled water. **(ii) Sample Preparation.** 2.2 mg of samples were each dissolved with 2 drops of HNO_3 or HCl and diluted with distilled water in a 50 mL volumetric flask to prepare the ICP samples. **(iii) Method.** The maximum wavelengths for the different elements were selected (P, 214.9 nm; Eu, 368 nm; Ca, 317.9 nm). A calibration curve for each element was constructed. After the calibration curve of each element was completed, the concentration (in ppm) was determined for two solutions of each sample.

Collection of NMR data. All of the NMR spectra were recorded on a JEOL GX-400 spectrometer in 5 mm tubes. Resonance frequencies are 400 MHz for ^{31}P. Chemical shifts are given with respect to external 85% H_3PO_4 for ^{31}P. Typical acquisition parameters for ^{31}P spectra included the following: spectral width, 320 MHz; acquisition time, 0.8 s; pulse delay, 0.1 s; pulse width, 15 μs (45° tip angle). Anywhere from 10 000 to 50 000 scans were required. For all of the spectra, the temperature was controlled to 25 (0.2°). For ^{31}P chemical shifts, the convention used is that the more negative chemical shifts denote upfield resonances. For all the measurements, all the samples were dissolved in D_2O.

X-ray diffraction (XRD). X-ray diffraction analysis was performed on a Philips X'Pert X-ray diffractometer, using Ni filtered CuKα radiation, operating at 45 mV and 45 mA, scanning in the 2θ range of 20-40^o, at step size of 0.02^o (2θ) and 3 seconds/step.

(1). Lattice parameters: HA powder was characterized using X-ray diffraction analyses (Philips X'Pert X-ray diffractometer) using Ni filtered CuKα radiation, operating at 45 kV and 45 mA, scanning in the 2θ range of 20-40^o, at step size of 0.02^o (2θ) and 3 seconds/step. Potassium Chloride was used as a standard to calibrate the angle shift. Lattice parameters were calculated from the following formula: $1/d^2 = [4/(3a^2)](h^2+hk+k^2)+l^2/c^2$, where d is the spacings between reflecting planes, $d = \lambda/(2\sin\theta)$, hkl = the Miller indices of reflecting plane, λ (wavelength) = 1.545 Å, θ = diffraction angle. The a-axis and c-axis dimensions were determined from [300] plane and determined from [002] plane respectively.

(2). Crystal size: [002] and [300] direction Crystal size was determined from the broadening at half height width ($\beta_{1/2}$) of the diffraction peak (either [002] or [300]) using the Scherrer formula: $t = 0.9\lambda / (\beta_{1/2} \cos\theta)$, where t is crystal size, λ (wavelength) = 1.545Å, $\beta_{1/2}$ is the difference of sample and instrumental broadening, $\beta_{1/2} = (B^2 - b^2)^{1/2}$, B = observed broadening from the XRD pattern, b = instrumental broadening (0.001 radian).

Rietveld analysis. Powder X-ray diffraction was performed using Powder XRD APS Sector 11-BMB for Rietveld analysis. Samples were ground in mortar and pestle, sieved to less than 20 μm grain size and loaded into Kapton® capillaries. Structure refinements of all five samples were done using the Rietveld method using the General Structure Analysis System (GSAS) and EXPGUI software packages. The data were collected and analyzed at Miami University, Oxford (OH) by Olaf Borkiewicz.

EXAFS analysis APS Sector 5-BMD 3/08.

The extended X-ray absorption fine structure (EXAFS) was used to determine the structural state (e.g. the identity, number, and interatomic distance of surrounding atoms) of Eu in the apatite. EXAFS fitting was done with the program WinXAS, and theoretical phases and amplitudes calculated using FEFF7. Eu L_3-edge EXAFS measurements on the europiumapatite were conducted at the X11A beamline X18B of National Synchrotron Light Source, Brookhaven National Laboratory. The sample was ground, diluted to 1.25 wt% Eu by mixing with BN powder and loaded in an acrylic frame holder and sealed on both ends by a layer of Kapton tape. The X-ray storage ring operated at 2.8

GeV with a maximum current of 280 mA. A Si (111) channel-cut monochromator, detuned by 20% to reduce the harmonics, was used to select the desired X-ray energy. The monochrometer was calibrated by assigning the first inflection point of the L_3-absorption edge of Eu in EuO model compound to 8052 eV. The X-ray beam size was 7 mm (horizontal) by 0.5 mm (vertical). All spectra were collected at room temperature in fluorescence mode at 90° to the incident beam using a Canberra 13-element Ge solid-state detector. The EXAFS scans were collected within 30 minutes by scanning the monochromator energy from x eV to x eV by using 5 eV steps before the Eu L_3 absorption edge (8052 eV) with 2 second signal recording time, 0.5 eV steps within + 30 eV of the absorption edge with 2 seconds signal recording time, and 0.05 Å-1 steps in photoelectron wave number above the absorption edge with 5 seconds signal recording time. 10 scans were collected at room temperature and averaged to obtain the raw spectrum for EXAFS fitting. The data were collected and analyzed in Miami University, Oxford (OH) by Olaf Borkiewicz and Yun Luo.

SEM-EDS: Sample texture, mineralogical purity and chemistry were evaluated by scanning electron microscopy at Miami University on a Zeiss Supra35 variable pressure SEM with a field emission source, an EDAX X-ray fluorescence detector, and an HKL electron backscatter diffraction detector. Data were collected at 20 kV acceleration voltage. Powder samples were lightly dusted on a carbon sticky tape and were analyzed uncoated in variable pressure mode to avoid charging. Textures were first observed by secondary electron imaging. The samples were then screened for phases with different mean atomic weights by backscattered electron imaging. Both the apatite (majority of the

samples) and any secondary phases, determined by brighter backscattered electron signal, were chemically analyzed by EDS. The data were collected and analyzed in Miami University, Oxford (OH) by Olaf Borkiewicz.

Luminescence. Luminescence was analyzed using a Flurolog Tau3 with a Spex 1934D phosphorimeter. Emission spectra were obtained after excitation at 397 nm. Excitation spectra was obtained by monitoring the luminescence at 614 nm (maximal intensity of the emission spectrum) and by varying the excitation from 250 to 600 nm. The luminescence decay lifetimes of the Eu^{3+} were obtained by monitoring the luminescence at 397 nm. The lifetimes were processed by fitting the decay curves to a single or double exponential functions using Sigma plot version3.

2.3- Results and discussion

2.3.1- Elemental analysis study

Table 2.2. Elemental analysis of the HA doped europium samples. These samples were prepared following a precipitation method at 95 °C as described in Experimental Section 2.2.1.

Eu content	0%	1%	5%	9.5%	13%	16.8%	18.2%	25%
Eu (mM)	0.000	0.165	0.26	0.529	0.741	0.881	0.934	0.973
Ca (mM)	17.900	30.45	5.54	4.760	4.930	4.148	3.905	3.185
P (mM)	12.645	19.90	4.44	4.497	4.929	4.297	4.174	3.781
Eu/(Eu+Ca) x100	0.00	0.54	4.5	9.99	13.06	17.52	19.31	23.40
(Ca+Eu)/P	1.42	1.54	1.31	1.18	1.15	1.17	1.16	1.10
Ca/P	1.42	1.53	1.24	1.25	1.06	1.00	0.97	0.84

Table 2.2 summarizes the elemental analysis data of all samples. The molar ratios Eu/(Eu+Ca) indicate that the amount of incorporated europium is close to the theoretical values, the more europium inserted the more europium collected in the precipitate. The ratio of (Ca+Eu)/P allows us to estimate the purity of the HA obtained. The (Ca+Eu)/P molar ratios are different than the Ca/P ratio for pure HA (1.67)[5]. In our prepared HA the Ca/P ratio is 1.42 which is lower than the stoichiometric ratio of 1.67 of HA. This indicates that the apatite is a calcium deficient apatite. The ratio for the 5% europium doping sample is similar to the one for the HA prepared which suggests incorporation of europium into the HA structure at 5% doping. After 5% the (Ca+Eu)/P ratio decreases

from 1.40 at 5% to 1.18 at 9.5% doping where it stabilizes at 25% europium doping when the (Ca+Eu)/P ratio reaches is 1.10 (Figure 2.1); these ratios are lower than the one for our prepared HA and suggest the presence of additional phosphate phases, which might contain europium. By comparison, the ratio Ca/P decreases with the increase in europium doping showing an increase in the phosphate phase especially after the 5% ratio. These observations of the presence of a possible europium phosphate phase are supported by the previous XRD analysis.

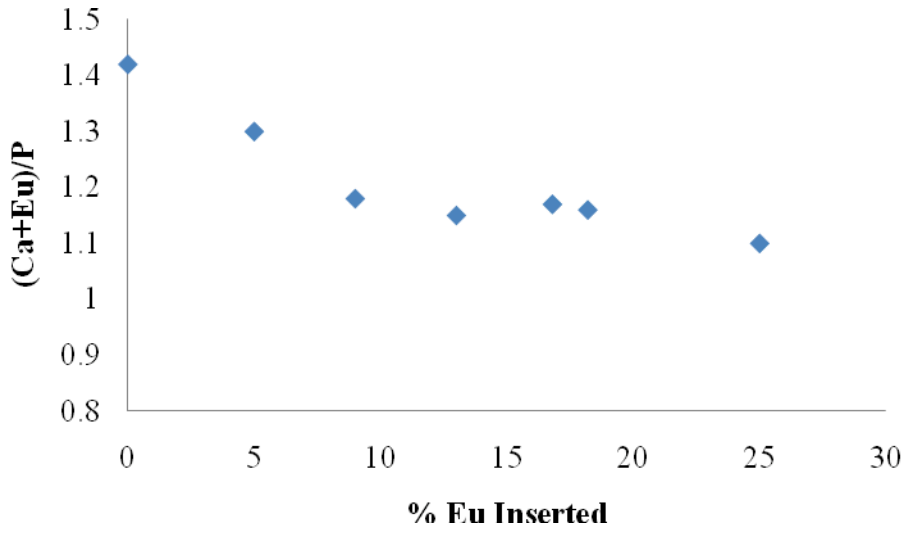

Figure 2.1. Graphic representation of the variations of (Ca+Eu)/P ratio with europium incorporation to the sample.

2.3.2- X-ray diffraction study

The X-Ray Diffraction (XRD) patterns of the hydroxyapatite samples doped with lanthanides such as Neodymium, Dysprosium, Lanthanum, and Europium have been reported to have similar pattern to the XRD of HA.[6-9] Likewise, our XRD from hydroxyapatite samples doped with various concentration of europium, show a similar pattern to the XRD of HA. The main characteristic peaks of the HA XRD pattern are observed in Figure 2.2. The XRD of the low concentration europium powders shows high crystallinity. As the doping increases the peaks get broader which is evidence of a lower crystallinity (see Figure 2.2). The broader the diffraction peaks the smaller the crystallite size.

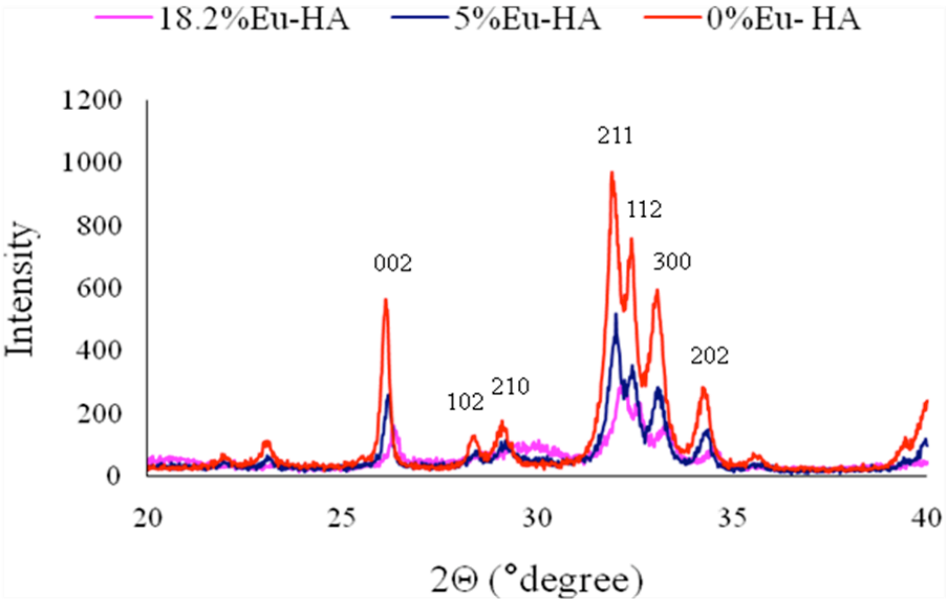

Figure 2.2. XRD spectra of 0%, 5% and 18.5%Eu-doped HA showing the plan lattice.

X-ray patterns of samples 5%Eu-HA and 18.2%Eu-HA indicated structural changes or presence of additional phases. As the concentration of the Eu(III) ion dopant

increased, a broad peak at about 30^{o} 2θ became more apparent, suggesting the presence of an amorphous phase identified as being $EuPO_4.H_2O$ (JCPDF file no. 20-1004). The presence of additional phases in the two preparations precludes better comparison of their structural parameters using the Rietveld refinement data.

At Miami University, the 1%Eu-doped HA and the 5% Eu-doped HA have been collected by Rakovan's group member in Miami University, Ohio, with a broader 2θ range and longer scans to provide better resolution. From Figure 2.3, the 1% Eu-doped HA XRD spectrum shows a perfect match with the HA XRD spectrum from JCPDF database, whereas the 5% Eu-doped HA XRD spectrum shows a less crystalline mixture of peaks, some matching the HA peaks from the database and the others matching the $Eu(PO_4).H_2O$ XRD database.

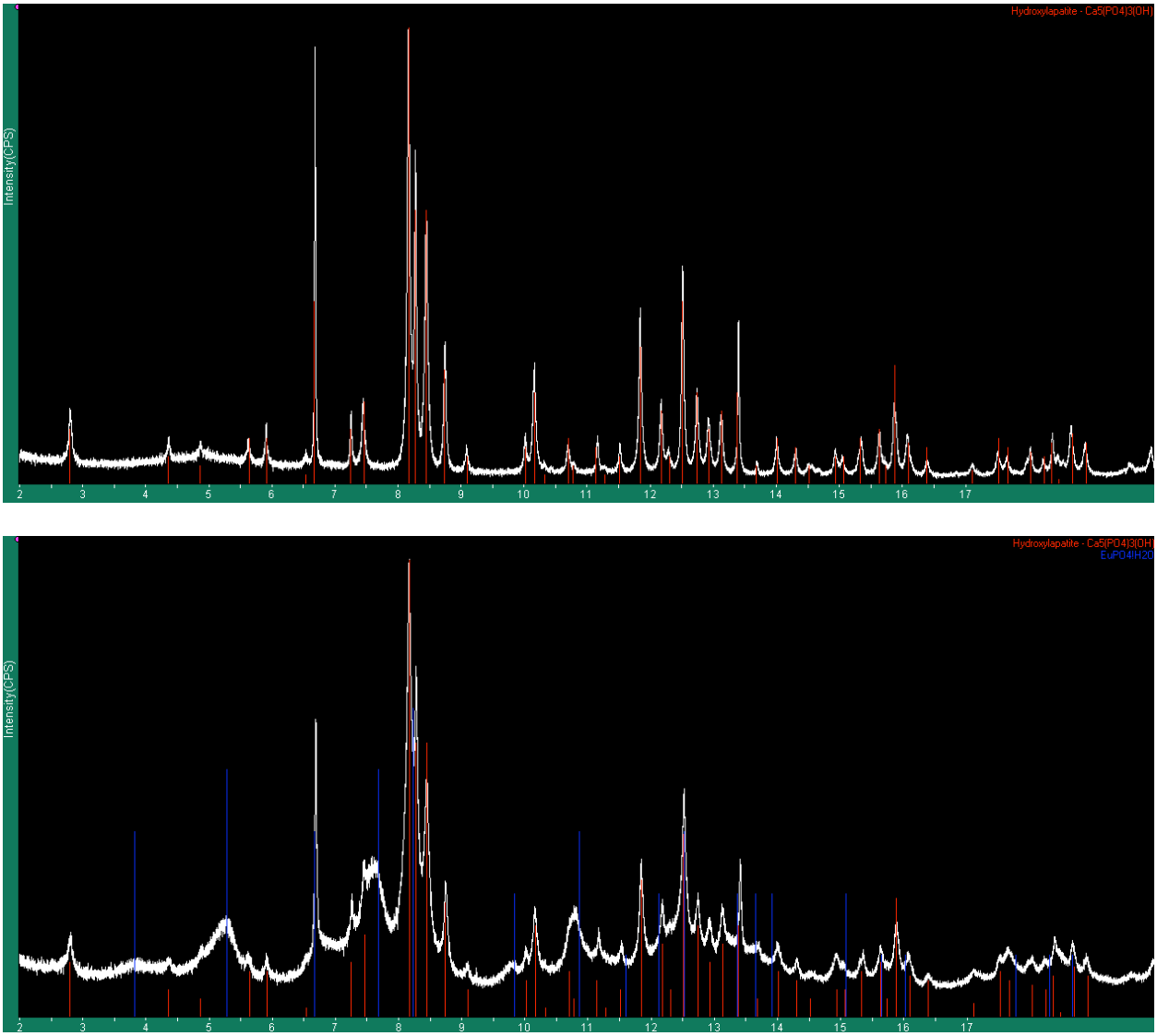

Figure 2.3. Refined XRD spectra of 1% Eu-doped HA(top) and 5% Eu-doped HA (bottom). These spectra have been compared with HA spectra and $EuPO_4.H_2O$ spectra from JCPDF database.

The crystallite size measured from the line broadening of the [002] and [300] diffraction peaks corresponding to the lattice directions perpendicular to the c and a axis respectively, decreased with the europium doping. The decrease stopped after 5% Eu doping, indicating a doping saturation point (Table 2.3, Figure 2.4). The smaller the crystal the lower the crystallinity, indicating that the structure is more disordered,

evidenced by broader peaks. Similarly, with increasing europium content from 1% to 25% the a-axis dimension of the apatite decreased from 9.463 to 9.430 while the c axis remain unchanged (Table 2.3, Figure 2.5). Both the decrease in crystallite size and the decrease in the a-axis parameter prove that the HA structure has been affected and altered by the europium doping and that a certain amount of europium has been incorporated in the HA structure. However the extent of its incorporation and amount incorporated cannot be drawn from this analysis.

Table 2.3. Effect of europium doping on the lattice parameters and the crystallite size of precipitated HA at 95 °C. The present samples are the europium doped HA with 0%, 5%, 9.5%,18.2% and 25% europium dopant.

Europium-doped HA samples	Lattice parameters (Å)		Crystallite size (Å)	
	a-Axis	c-Axis	[002]	[300]
0% Eu-doped HA	9.463	6.873	778	434
5% Eu-doped HA	9.441	6.873	690	341
9.5% Eu-doped HA	9.438	6.868	690	301
18% Eu-doped HA	9.430	6.870	690	305
25% Eu-doped HA			690	301

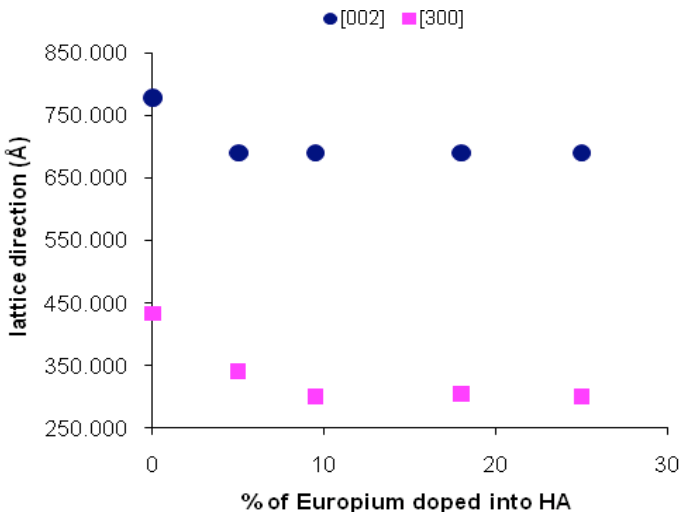

Figure 2.4. Visual graph of Table 2.2observing the effect of the HA-europium doping content with the crystallite size from the lattice directions [002](blue) and [300] (pink) of the HA. The plane [002] perpendicular to the c-axis and the plane [300] perpendicular to the a-axis both decrease with the europium doping.

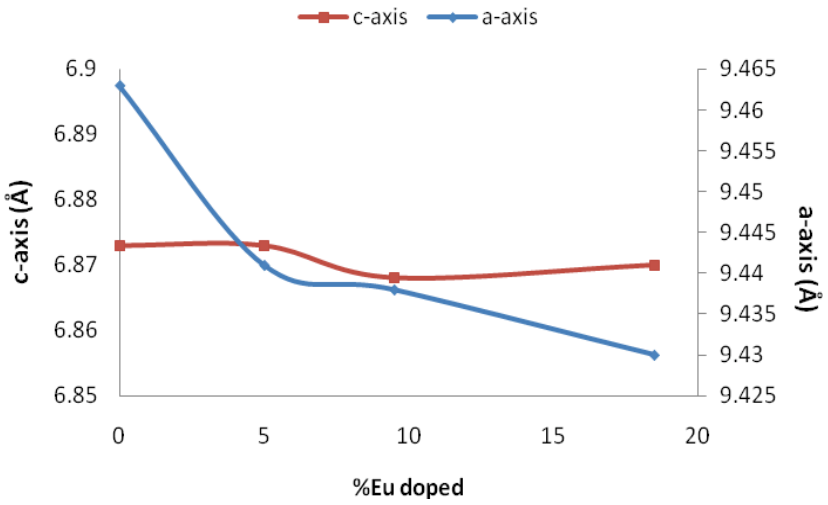

Figure 2.5. Visual graph of table 2.2 showing the fluctuation of the a and c latice parameters with the amount of europium doping. The a-axis (blue) is slightly decreasing with the doping whereas the c-axis (red)is not changing.

XRD patterns of 0% europium, 5% europium, 18.5% europium and 25% europium doped HA, sintered at temperature of 800 ^{o}C showed the presence of other peaks that were identified as beta-tricalcium phosphate (β-TCP), shown in Figure 2.6. β-TCP

forms when a calcium-deficient apatite is sintered at temperatures 800 ^{o}C and above[5]. In addition, it can be observed in the XRD patterns that the HA [300] diffraction peak shifted to higher 2Θ for the 18.2% Eu-HA compared to the 0% Eu-HA while no significant shift was observed for the β-TCP diffraction peaks between the two samples. This shows that the europium indeed incorporates in the HA structure affecting the a axis of the HA lattice. As the [300] lattice direction shifted towards the higher Θ with europium incorporation, the a axis decreases, as has already been observed previously[5]. Also, as the peaks characteristic for β-TCP remain unchanged, it shows the stability of europium in the HA structure. Moreover in the XRD of the 18.5% europium doped HA sintered, the peak at 30° appears broader and bigger than the one for the 0% europium doped HA. This observation reinforced the presence of another amorphous phase at 30 °.

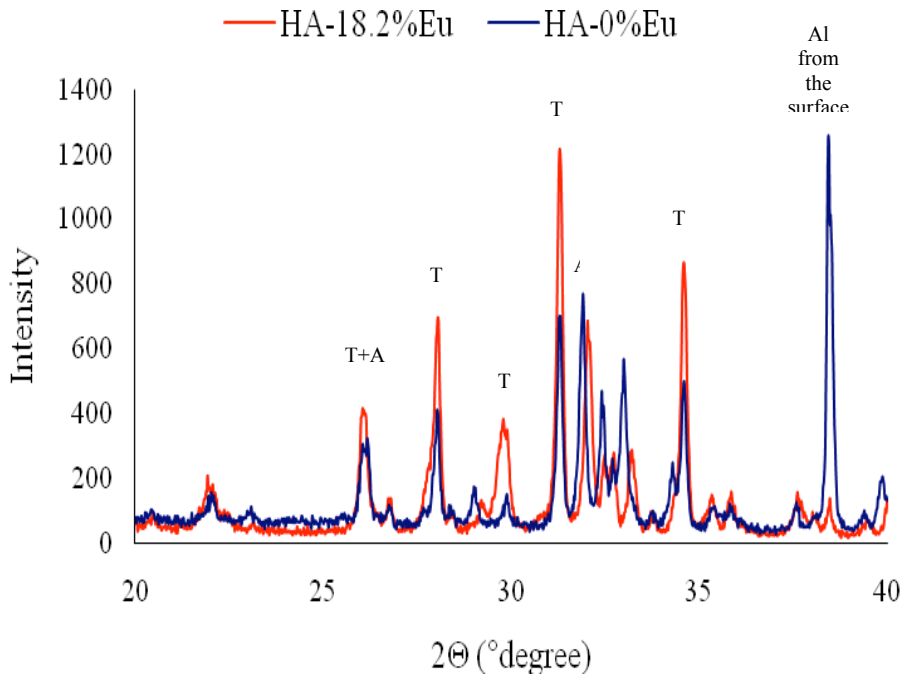

Figure 2.6. XRD patterns of apatitic precipitates (prepared at 95 °C) after sintering at 800 °C: 0% Eu-HA(blue) and 18.2% Eu-HA (red). T and A on the XRD patterns indicate the major peaks of the β-TCP and HA respectively.

2.3.3- Spectroscopy study

We concentrated on the vibration modes attributed to the phosphate and the hydroxyl ions vibrational mode in the apatite. Walters and Legeros[10] previously established the splitting of the T_2 vibration mode of the phosphate ions into 8 factor groups. The symmetries ν_1 and ν_2 are not split and the peaks are weak but observable in the IR in the mineral phase. The most relevant absorption peaks are the ν_3 (1000-1100 cm^{-1}) and ν_4 (550-620 cm^{-1}) bands which belong to the T_2 vibrational mode of the free phosphate ion. Each of them is split into two major bands: in the high frequency region from E_{1u} and in the low frequency region from A_u and E_{1u}.

The absorbances from the IR spectroscopy from the different doped samples are listed in Table 2.4. According to the infrared spectra of the samples with a low doping, the apatite absorption bands were present. The bands at 1100 cm^{-1} (ν_3), 1032cm^{-1} (ν_3), 962 cm^{-1} (ν_1), 602 cm^{-1} (ν_4) and 563 cm^{-1} (ν_4) are characteristic of P-O stretch of the PO_4^{3-} group from the apatitic environment; the weak band at 862 cm^{-1} is characteristic of the P-OH stretch from the HPO_4^{2-} group present; the weak band at 638 cm^{-1} is due to the O-H vibrational mode from the apatite. A band at 538 cm^{-1} becomes more apparent after 18.2% europium doping. After 50% europium doping, the IR spectrum changes; we observed that the υ_3 absorption band is slightly shifted to higher frequency.

	P-Oν_3		P-O (ν_1)	P-OH stretch	O-H stretch	P-O (ν_4)	P-O (ν_4 bend)		
0%Eu-HA	*1109*	*1032*	*962*	*634*		*602*		*563*	
5%Eu-HA	*1111*	*1032*	*964*	*636*		*604*		*563*	
9.5%Eu-HA	*1109*	*1034*	*964*	*636*		*604*		*565*	
13%Eu-HA	*1109*	*1032*	*964*	*634*		*606*		*563*	
18.2%Eu-HA	*1099*	*1036*	*964*			*604*		*563*	*538*
25%Eu-HA	*1099*	*1038*	*962*		*621*			*565*	*538*
50%Eu-HA	*1080*	*1020*			*623*		*585*		*536*
$EuPO_4.2H_2O$	*1070*	*1042-1020*	*977*		*629*		*571*		*540*
$EuPO_4$ anh	*1104*	*1050-1000*	*963*				*581*		*542*

Table 2.4. FT-IR peaks from P-O and O-H stretches/bents from different phosphates and hydroxyl groups. The last 2 rows are the Infra-red absorption bands from the IR spectra of the europium phosphate anhydrous and hydrated (*Spectrochim Acta* **1966**, *22*, 1949)[11].

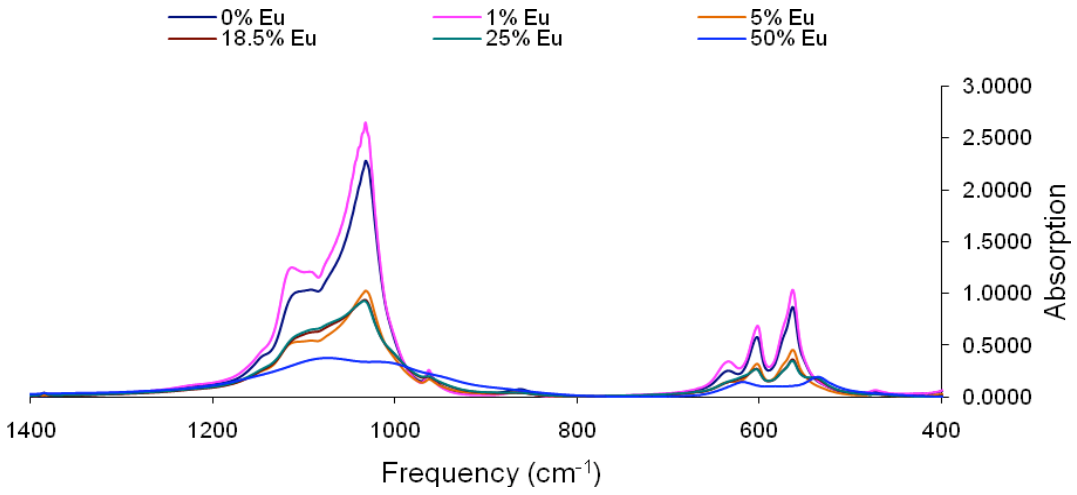

Figure 2.7. IR spectra of the samples with various europium doping concentration (0%, 1%, 5%, 13%, 18.5%, 25%, 50%). The observed decrease in resolution of the IR spectra reflect the loss of crystallinity similar to that shown in the XRD patterns (Figure 2.2)

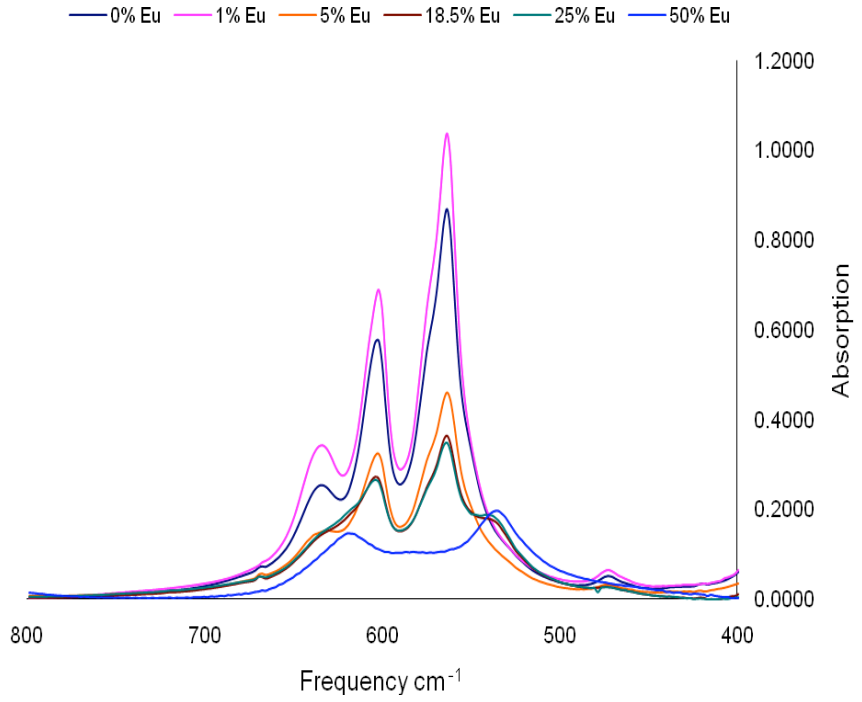

Figure 2.8. IR spectra of the Eu(III) doped HA samples from Figure 5 focusing on the P-O vibration modes in the region, 750 cm^{-1} to 400 cm^{-1}.

Increasing loss in the resolution of the PO_4^{3-} absorption bands was observed as the europium doping was increased. The resolution of the IR absorption bands reflects the crystallinity of the apatite. The decrease in crystallinity with increasing dopant concentration was also observed in the XRD data. Most of the P-O bond vibrations remain unchanged except one of the ν_3 absorption bands which shifts from 1113 cm^{-1} to the lower energies 1092 cm^{-1} with increasing the europium doping concentration from 1% to 25%. The decrease in energy of the P-O absorption band suggests the lengthening of the P-O bond.[7] The lengthening could imply the presence of a electron withdrawing element such as metal coordinated to another O from the PO_4 group. This idea is reinforced by the appearance of a vibration in the lower energy region (538 cm^{-1}); this is a signature of a vibration of a metal–oxygen bond. Get'man observed similar low energy absorption band upon incorporating Dy into HA; which he also ascribed to the Dy-O bond vibrations. Also the disappearance or shift of the absorption band at 634 cm^{-1} identified as the O-H vibration band could suggest a coupled substitution of calcium ion Ca^{2+} for europium Eu^{3+} and hydroxide ion OH^- to oxygen ion O^{2-} providing a charge balanced.[7] This observation corroborates also the work of Serret reporting the lanthanum substitution in HA's calcium sites.[12] The OH groups are located in the center of the structure channels of HA close to the Ca2 site. Thus, as the OH stretching and librational modes shifted, we can preliminarily suggest that the Eu^{3+} ions substitute in the Ca(2) site i.e. in the $Ca(2)O_7$ polyhedra.

2.3.4- Luminescence study

The observed emission corresponds to f-f transitions within the $4f^6$ configuration. The emission spectra of Eu-HA were recorded with an excitation wavelength at 397 nm. The emission spectra showed the strongest emission at 614 nm and 592 nm with two medium peaks at 690 nm and 696 nm and a small peak at 654 nm. These emissions are assigned to the $^5D_0$ to the ^7F_n transitions (Figure 2.9)

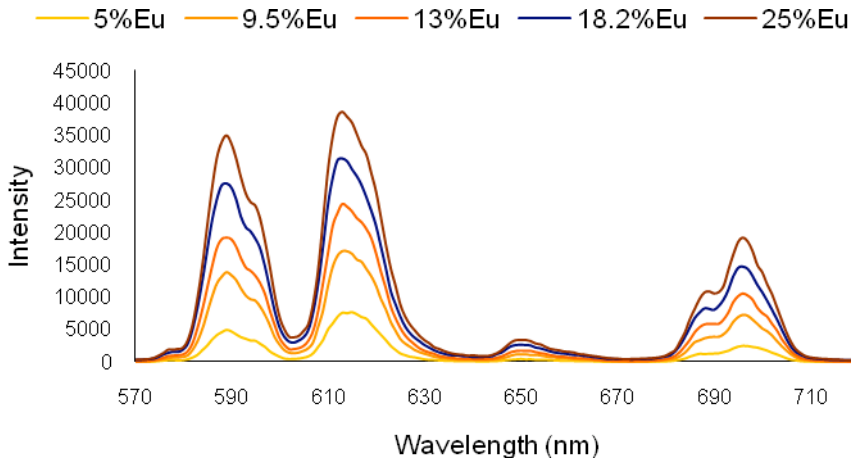

Figure 2.9. Luminescence emission spectra of HA samples doped with various europium concentrations (5%, 9.5%, 13%, 18.5%, 25%). The samples are excited at λ = 397 nm.

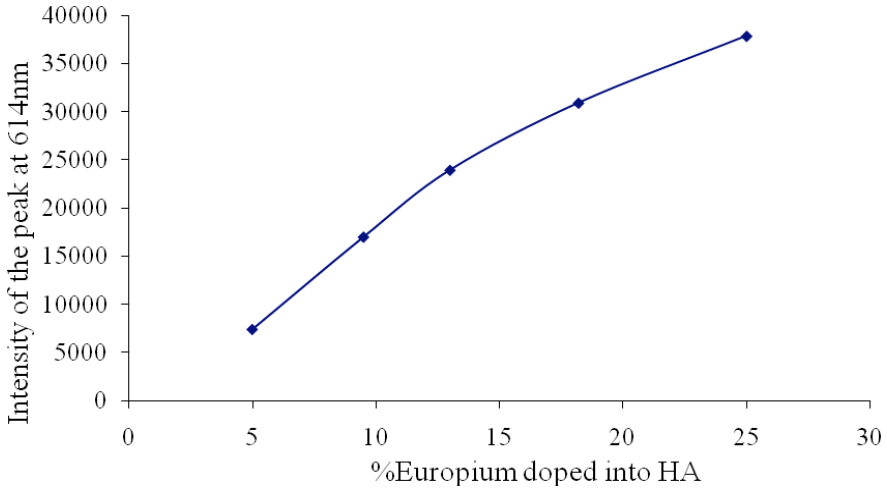

Figure 2.10. Plot of the intensities of the emission band monitored at 614 nm as a function of europium doping from Figure 2.9.

Figure 2.9 shows the emission spectra of the Europium doped HA samples. Figure 2.10 shows the intensities of the band at 614 nm from the emission spectra. We observe in both cases an increase of the europium luminescence intensity with an increase of the doping concentration. This is consistent with the results observed from the ICP analysis showing the increase of the europium content in the sample with the increase of the europium doping concentration. However, this is not an indication of incorporation in the HA structure. In order to know more about the environment of the europium in the samples, the luminescence decay lifetimes would interrogate the different europium environments by detecting the different sources of quenching.

The luminescence decay times were measured upon excitation into the 397 nm absorption band; this is the $^5D_0$ excited state of Eu^{3+} on solid state samples. The factor responsible for quenching would be the hydroxyl groups from the HA structure since

these are solid-state samples and non-radiative quenching contributions from inner and outer sphere water molecules due to solution are negligible. The measured lifetimes are single exponential with decay times ranging from 864 ms to 900 ms (Table 2.5). These lifetimes are consistent with approximately 1 molecule of water in the outer sphere based on the following Table 2.5 and the equation previously mentioned for the estimated number q:

$$q = A(k_{H2O} - k_{D2O})$$

where A is a coefficient factor equal to 1.2 ms^{-1} for europium and k_{D2O} is estimated as 0

The luminescence lifetimes remain essentially unchanged upon increased doping of europium suggesting an unchanged europium environment.

Table 2.5. Luminescence study on life time decay of HA doped europium samples. The samples were excited at 397 nm and a time-grating technique excluding scattered light and background luminescence with shorter life time from the long lifetime luminescence of europium centered luminescence.

	5%	9.50%	13%	18.20%	25%
k (ms^{-1})	1.144	1.129	1.115	1.158	1.11
Life time (ms)	0.874	0.885	0.897	0.863	0.900

2.3.5- Scanning electron microscopy (SEM), electron backscattered electron (BSE) and energy disperse X-ray spectroscopic (EDS) analysis

The scanning electron microscopy (SEM) is a type of electron microscopy which images the sample surface by scanning it with a high-energy beam of electrons. The

electrons from the beam interact with the atoms from the sample. Signals are produce revealing information about the sample's surface topology, its composition and other properties such as electrical conductivity. The types of signals produced by an SEM include secondary electrons and back scattered electrons (BSE). BSE are produced after the interaction of the electron beam with the nuclei of an atom. Some of the incident electron beam goes through the sample but also a part of this beam can be scattered back out of the sample. The amount of electrons scattered back varies in function of the atomic number Z of the scattering atoms. As a result, areas of high average atomic number appear brighter than the areas with low average atomic number.

EDS is used as a technique for elemental analysis or chemical characterization of a sample. A beam of electrons, protons or X-ray excites the electrons from the inner shell of the atoms of the sample. These electrons pass from a unexcited state (in their ground state) to an excited state, creating an electron hole in the ground state. As an electron from the outer shell comes down to fill up the hole in the lower shell, energy gets emitted from the energy difference between the higher shell and the lower shell in the form of an X-ray.

From SEM imaging it can be seen that the apatite forms very fine-grained crystals with their maximum dimension less than 1 μm and their shorter dimensions much lower than 1 μm. The SEM image of the sample Eu1% HA shows clearly a morphology of needle shaped crystals that are elongated in the [001] direction (Figure 2.11).

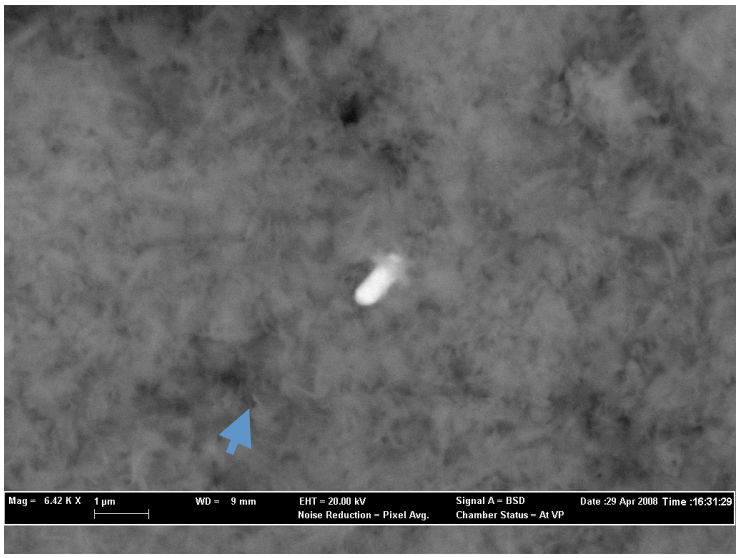

Figure 2.11. SEM backscattered electron image of a 1% Eu-doped HA sample prepared as described in experimental section 2.3.6. The multitude of crystals (gray) are apatite. The large bright crystal in the center is another as yet unknown phase. The arrow points to a well resolved needle-like apatite crystal.

In Figure 2.11, the second phase is present as a single crystal of much larger size than the apatite crystals in the sample. The greater brightness in the backscattered electron (BSE) image indicates a greater mean atomic weight of the second phase than for the apatite phase.

The EDS spectrum from the crystal in Figure 2.11 is shown in Figure 2.12. In Figure 2.12, the EDS data from the large bright crystal in the 1% Eu-doped sample (Figure 2.11) shows the presence of significant lead (Pb) impurity. Although the spectrum shows the presence of P and Ca, the EDS from the 1%Eu-HA sample shows also the europium peak. Nevertheless, further characterization of this crystal may be useful for phase identification and exact chemistry.

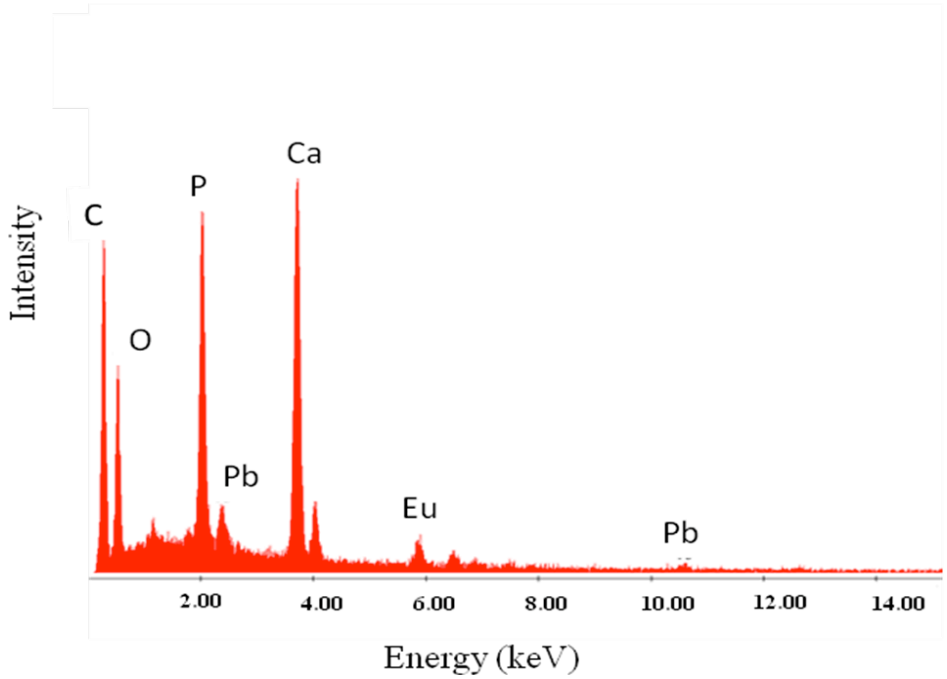

Figure 2.12. EDS spectra from1% Eu doped HA sample. The beam of electron is directed on the large single crystals shown in Figure 2.11.

An SEM - BSE image collected from the 9.5% Eu doped HA reveals different areas with a homogeneous collection of apatite crystals. In Figure 2.13 the SEM image of Eu9.5**%** doped HA sample exhibits slight variations in brightness, indicating a slight difference in mean atomic weight. EDS data are collected from the bright area (EDS1) and the less bright areas (EDS2) and compared in Figures 2.14 and 2.15 respectively. The elements present in both spectra are O, P, Ca, Eu and carbon C. The C is assumed to be from the carbon sticky tab on which the powder is mounted. Figure 2.14 shows the EDS spectrum of the bright region (EDS 1) from Figure 2.13. The bright areas (EDS 1) show more intense Eu peaks, indicating higher europium concentration, which is consistent with the brighter BSE imaging. Also, it shows a smaller amount of Ca relative to P. The Ca/P ratio can be interpreted in at least two ways: either the sample is all apatite in which case Eu would be substituting for Ca in the HA structure or another phase such as $EuPO_4$

or $EuPO_4.H_2O$ could be potentially present. The intimate admixture of HA and a $EuPO_4$ phase is highly suspected because the increased $EuPO_4$ phase relative to apatite phase would result in an increase of the intensity of the Eu peaks relative to the P compared to the Ca peaks (given the ratio of (Eu+Ca)/ P in the two phases: 1:1 in $EuPO_4$ vs 5:3 in apatite). The intensity of the O peak in the bright areas (EDS 1) is about twice as much as the one in the darker areas (EDS 2) (Figure 2.15). If the sample was all apatite then the O peak intensity should be the same in both areas. However, the (Eu+Ca)/O ratio in EuPO4 is 1:4 while in apatite it is 5:12 (approximately 1:2). Therefore, there is about twice as much O in EuPO4 as there is in apatite. The double increase in O peak intensity confirms the presence of two phases in the 9.5% Eu doped HA sample; these are apatite and $EuPO_4$.

Figure 2.13. BSE-SEM image of the 9.5% Eu-doped HA sample showing slight contrast between areas of what are assumed to be all apatite indicating a variation in mean atomic weight.

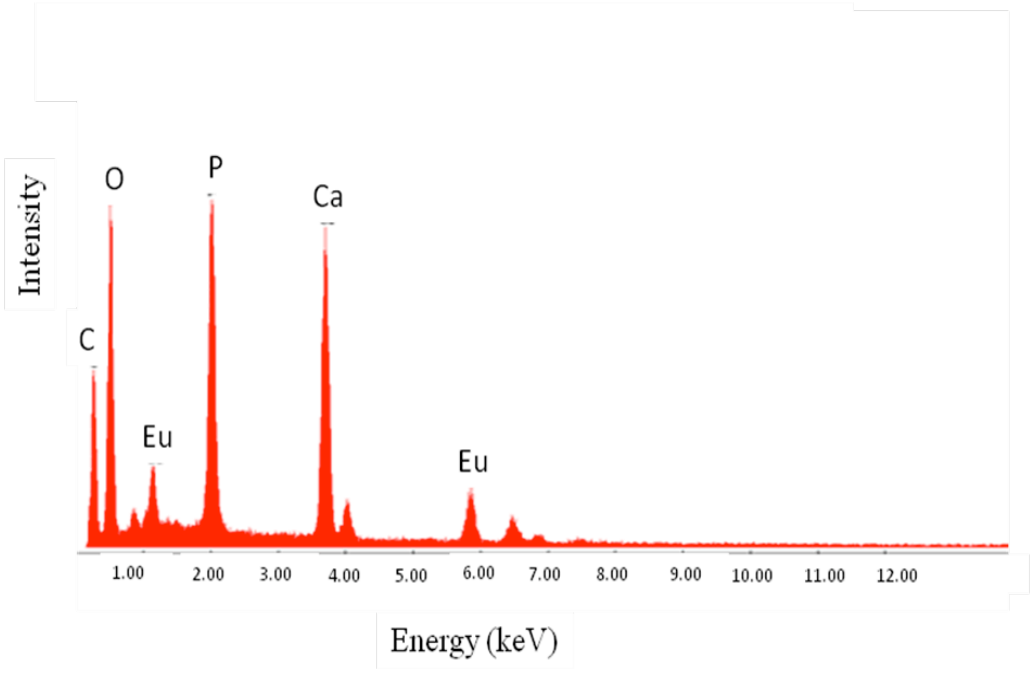

Figure 2.14. EDS spectra from areas labeled EDS 1 from figure 2.13. The three unlabeled peak indicated by arrows are Ca Kβ, and other Eu L fluorescence lines.

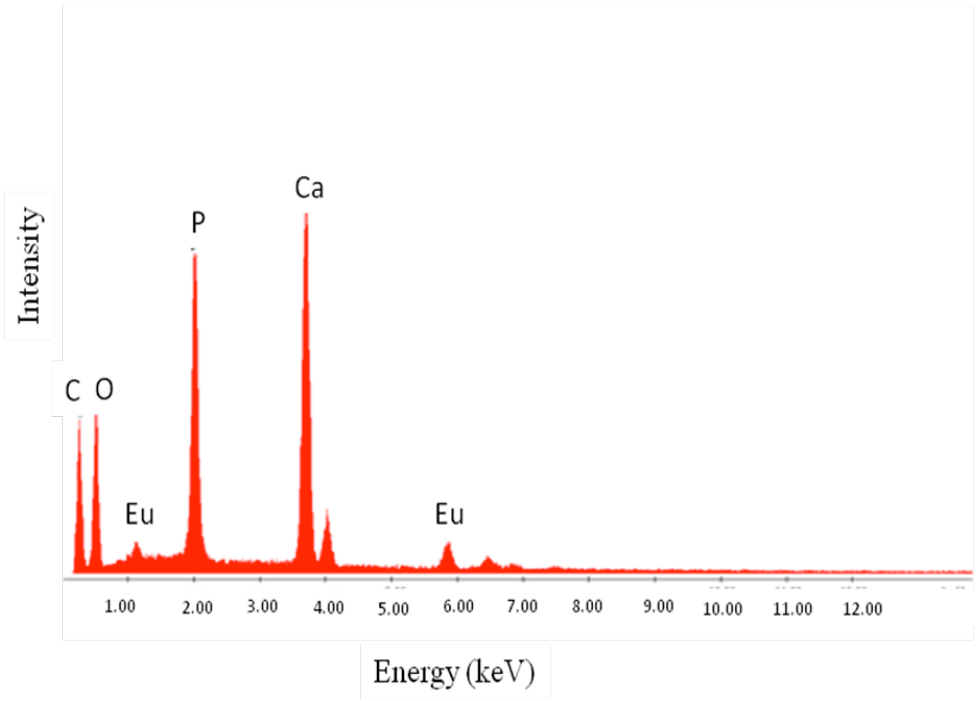

Figure 2.15. EDS spectra of from area labeled EDS 2 from Figure 2.13. The three unlabeled peaks indicated by arrows are Ca Kβ, and other Eu L fluorescence lines.

2.3.6- Extended X-ray absorption fine structure (EXAFS)

An X-ray beam is hitting the sample. The photon energy of the beam is gradually increased in order to reach one of the edges of the target element from the sample. The photon energy need to be sufficient in order to overcome the absorption edge K, when the beam can excite the electrons of the desired atomic level L. The resulting photoelectrons backscatter and hit the surrounding neighboring atoms. What is observed is a series of oscillations or waves on the high photon energy side of the adsorption edge.

EXAFS data were collected on samples HA-1%Eu and HA-5%Eu. The relevant atomic level for europium is level 3. The fitting of the Eu L-3 edge EXAFS was collected at the National Synchrotron Light Source (NSLS) with a beam line X11 on sample HA-5%Eu. Unfortunately, Eu L-3 is limited in energy above the absorption edge because the Eu L-2 is only 687 eV higher which makes these two levels very close to each other and therefore difficult to analyze separately. Twenty five scans were collected and merged. A reasonable EXAFS to about 7 or 8 k (Figure 2.16) is extracted. The Fourier Transform magnitudes of this data show three resolvable shells of atoms about the Eu (Figure 2.17). The EXAFS data were fit using four different models: (1) Eu in Eu-O system in structure (SG = Fm3m), (2) Eu in the $EuPO_4$ (monazite) structure, (3) Eu in the Ca1 site in the apatite structure and (4) Eu in the Ca2 site in the apatite structure. Only preliminary fitting was achieved.

The following summarizes the results of these models: (1) Eu-O gives a good fit with 13 good data points and 11 free variables; (2)The fit for $EuPO_4$ is not as good, but it has not been worked on as much given the more complex structure; (3)The data could not be

fit well with a model of Eu in the Ca1 site of apatite; (4) A better fit was achieved by modeling Eu in the Ca2 site, but as with the models of $EuPO_4$ it is not yet well refined. These samples cannot be fit to a suitable model for Eu in the Ca1 or Ca2 sites due to sufficient levels of Eu-based impurities in the sample. EXAFS is a technique that generally reports on an average environment for, in this case, Eu(III), and therefore, a number of Eu(III) impurities will require a very sophisticated model that is beyond the scope of this project.

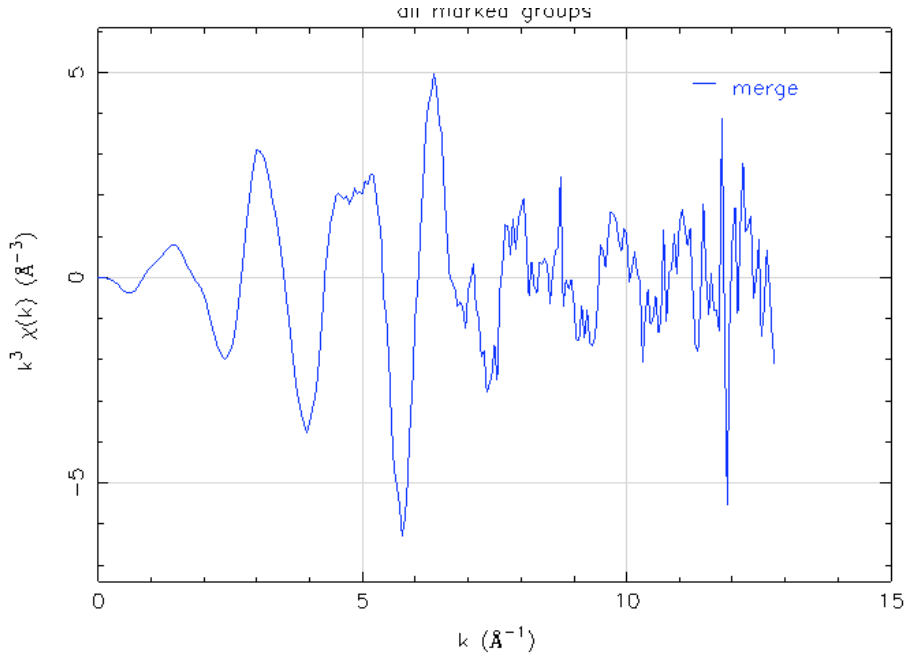

Figure 2.16. The k3-weighted EXAFS of the 5% Eu-doped HA

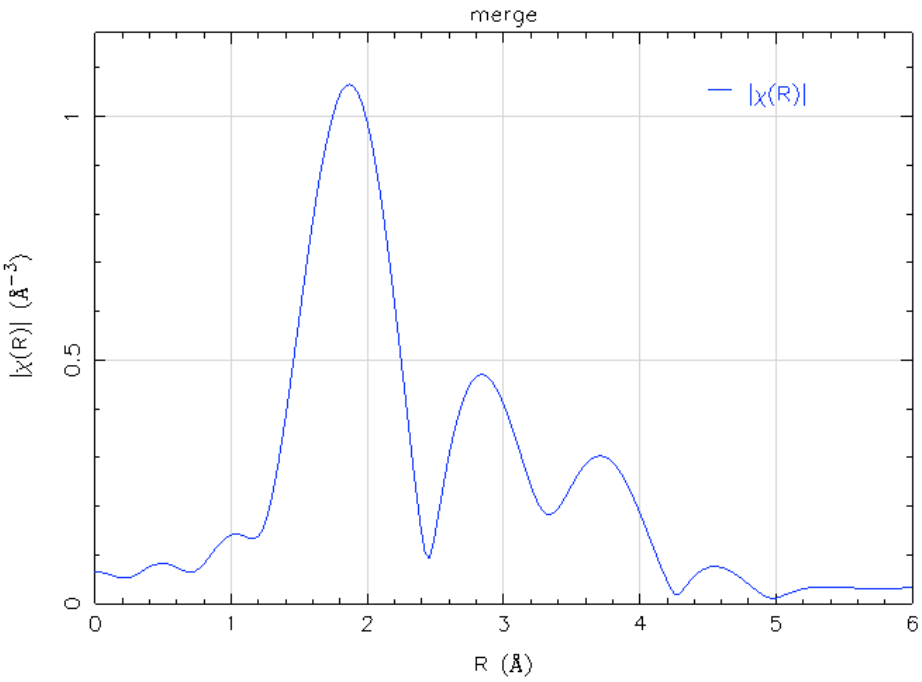

Figure 2.17. Fourier transform magnitudes of 5% Eu-doped HA , without correction for phase shifts.

2.3.7- Rietveld analysis

By modeling the Ca1 and Ca2 sites with Ca scattering factors and refining the occupancies, we see excess scattering at both sites (Figure 2.22) indicating the presence of a small amount of some other elements heavier than Ca.

*	name	type	ref/damp	fractional coordinates			Mult	Occupancy	Uiso
1	Ca1	CA	X0 U0 F0	0.666670	0.333330	-0.003445	4	1.0484	0.02246
2	Ca2	CA	X0 U0 F0	-0.011398	0.245131	0.250000	6	1.0131	0.01141
3	P	P	X0 U0 0	0.378201	0.404745	0.250000	6	1.0000	0.01866
4	O1	O	X0 U0 0	0.479081	0.327797	0.250000	6	1.0000	0.00618
5	O2	O	X0 U0 0	0.465487	0.586236	0.250000	6	1.0000	0.02809
6	O3	O	X0 U0 0	0.252353	0.332414	0.073045	12	1.0000	0.04528
7	O(H)	O	0 0 0	0.000000	0.000000	0.197900	4	0.5000	0.02500
8	H	H	0 0 0	0.000000	0.000000	0.040000	4	0.5000	0.02500

a	9.435622	b	9.435622	c	6.874016
α	90.0000	β	90.0000	γ	120.0000

Figure 2.18. Phase parameters refined from powder diffraction data using GSAS from sample 9.5%E-doped HA.

However, the Rietveld analysis is difficult to interpret given the uncertainties in the nature of the samples considering the presence of different phases and their chemical purity. We attempted to model the partitioning of Eu between the two Ca sites from the occupancy results. The low resolution and intensity of the peaks [002] at 6.7 2θ and [004] at 13.4 2θ after refinement, also reveal that these samples are subject to the presence of impurities which make the refinement challenging.

2.3.8- Conclusion

From these different analyses, it can be stated that we successfully incorporate europium in the HA structure using a precipitation method. The incorporation does not linearly increase with the amount of europium inserted; it reaches a saturation point before 5% europium when the europium forms an amorphous phase identified as hydrated $EuPO_4$. The presence of this phase and probably other minor amorphous phases render the use of some analysis methods difficult. Although it is very difficult to fully

assign the position of europium within the HA structure, from some of the raw results and the results from others research groups, one may lean towards the Ca(2) site versus the Ca(1) site, as the Ca(2) cavity hosts the europium(III) ions better.

2.4- Adsorption of EuEDTMP and EuDOTMP onto HA using phosphate buffer and Tris buffer as media

2.4.1- EuEDTMP and ErEDTMP solution ^{31}P NMR speciation at different pH 7 and 11

The EuEDTMP and ErEDTMP have been synthesized and ^{31}P NMR spectra have been processed at pH 7 and pH 11 in order to see the pH dependence on present species in solution.

Figure 2.19 shows one broad peak with a width of 16 kHz at 53 ppm. This peak corresponds to the $[Eu(EDTMP)]^{-5}$ species. When the concentration of EuEDTMP is higher than the one of $[^{-}OH]$ the intramolecular exchange between binding to the europium is fast and the four phosphorus atoms are averaged. We then would only see one peak. As we increased the pH from 7 to 11, a splitting of the peak occurs, leading to a set of three peaks, one main peak at 40 ppm and two smaller at 60 and 77 ppm (Figure 2.20). These peaks maybe associated with the formation of the hydroxy species of the complex. The broadness of the peaks could reflect the slower exchange rate of the ligand.

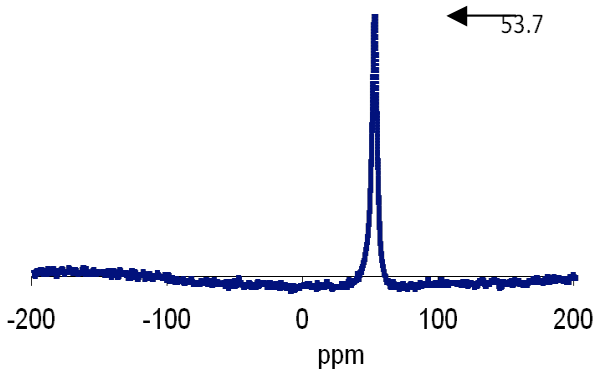

Figure 2.19. Spectrum of ^{31}P solution NMR of EuEDTMP at pH 7.

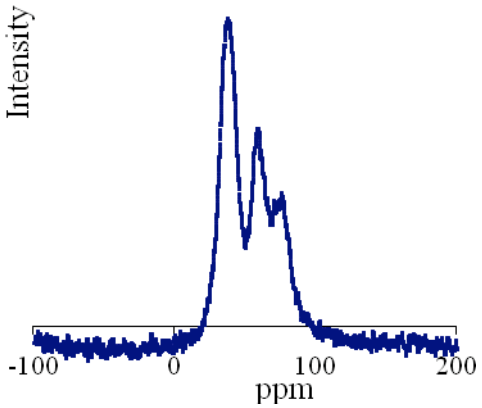

Figure 2.20. Spectrum of ^{31}P solution NMR of EuEDTMP at pH 11.

If we look at the Er(EDTMP) complex, we observed an early splitting of the peak (Figure 2.21), which is subject to further splitting. Figure 2.22 shows a symmetrical

quartet of broad peaks that could be associated to the formation of four hydroxyl complexes $Er(EDTMP)(OH)_n^{-(5+n)}$ with more rigid structure as the peaks appear more defined than at pH 7.8.

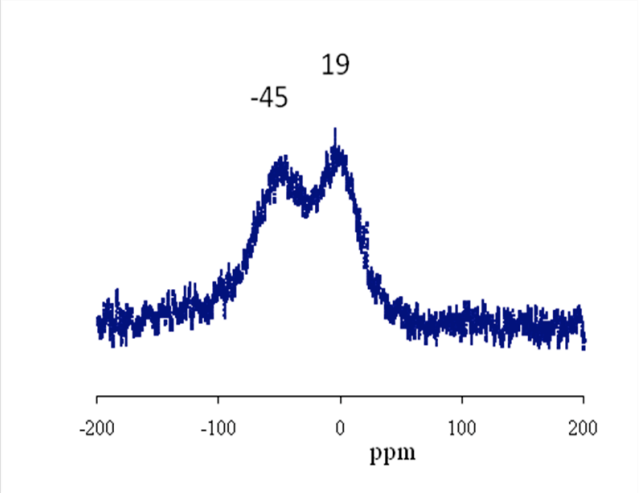

Figure 2.21. Spectrum of ^{31}P solution NMR of ErEDTMP at pH 7.8.

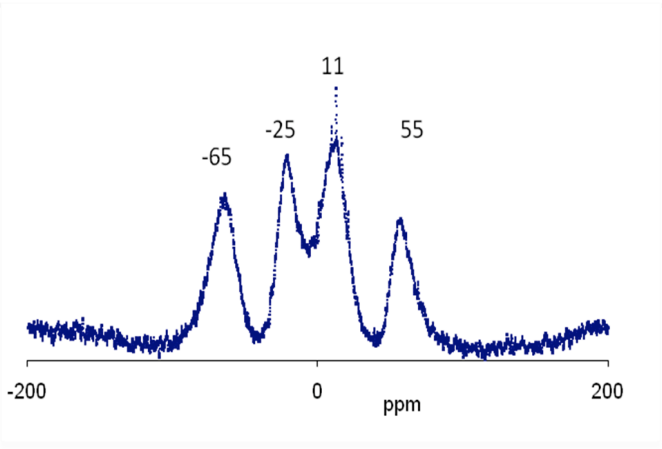

Figure 2.22. Spectrum of ^{31}P solution NMR of ErEDTMP at pH 11.5.

2.4.2- EuEDTMP adsorbed to HA using phosphate buffer as media

In the following section, we look at the adsorption of EuEDTMP onto HA in a phosphate buffer. In the next two sections, we examine the influence of the media on the adsorption by looking at its adsorption in a non-phosphate buffer and the influence of its structure on the adsorption by looking at the adsorption of EuDOTMP in a phosphate buffer.

When we look at the ICP-AA analysis of EuEDTMP adsorbed onto HA in the phosphate buffer, we can attest to an adsorption from the presence of europium in the sample. The amount of europium stays steady at a value of 2% europium EDTMP adsorbed until a ratio of 10/1 and then a slight increase to 3.8% europium EDTMP adsorbed at a ratio of 20/1 (Table 2.6). Nevertheless, we have to keep in mind that the EuEDTMP may not be stable in the phosphate buffer and therefore the europium can undergo transchelation from the ligand onto the HA surface..

Table 2.6. ICP results from the samples of europium(EDTMP) complex adsorbed to HA at various ratio of complex/HA inserted.

Experimental (EuEDTMP)/HA ratio	1:1	5:1	10:1	15:1	20:1
%Eu(EDTMP)	1.35	1.66	2.12	3.66	3.84

The f-f transition spectra of Eu(III) ion are one of the most easy and informative spectra among all of the other lanthanide ions thanks to the fact that the ground state $^7F_0$ and the emitting state $^5D_0$ of the ions are non-degenerate[2]. The transition $^5D_0 \rightarrow {}^7F_1$ is

magnetically allowed and its intensity is independent of the Eu(III) environment, which can be a useful tool to calibrate the intensity of other transitions. Indeed, the $^5D_0 \rightarrow {}^5F_2$ transition is known as an hypersensitive transition and its intensity depends grandly on the symmetry of europium ion and/or the ligand polarizability[13]. Therefore, due to the ratio of the emission bands representing the $^5D_0$ to $^7F_1$ and $^5D_0$ to $^7F_2$ transition states at 590 nm and 614 nm respectively, the symmetry of europium(III) can be studied. In Figure 2.23, this ratio remains constant at a value of 2.5-3 until the EuEDTMP/HA ratio reaches 10/1 and then decreases to 1.75. The emission ratio of EuEDTMP in water has been evaluated at 1.8. If we compare the Eu (III) symmetry in our system with its symmetry in water, one can see clearly that the value of the emission ratio of EuEDTMP in water is close to the emission ratios that we observe between 10/1 and 20/1 EuEDTMP to HA. This observation is consistent with the lifetime measurements, below.

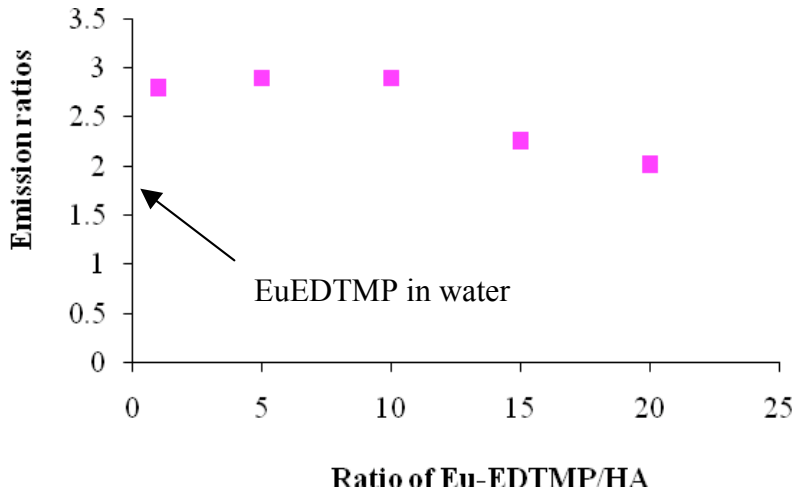

Figure 2.23. Intensity ratio of peak at 614 nm versus the peak at 590 nm from the europium emission spectrum (λ_{exc} = 397 nm).

Table 2.7. Rate decays and life time decays of Eu(III) ion in the EuEDTMP complex adsorbed to HA

EuEDTMP/HA	1/1	5/1	10/1	15/1	20/1
K (ms^{-1})	1.046	1.067	1.247	1.62	1.675
Life time (ms)	0.956	0.937	0.802	0.617	0.597

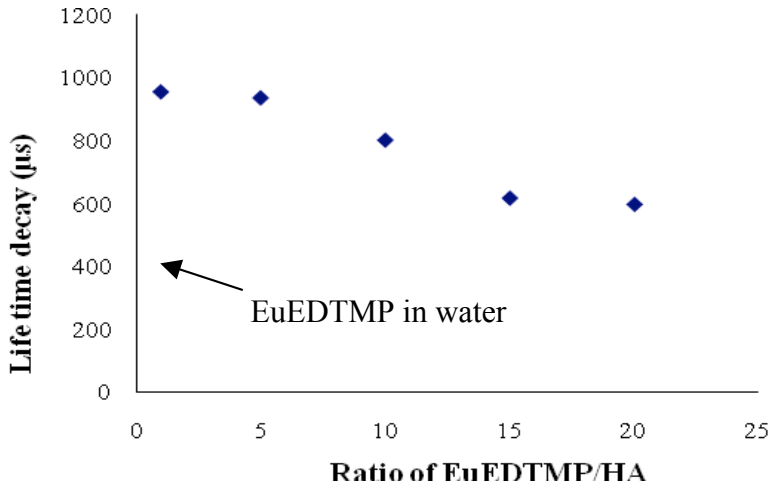

Figure 2.24. Life-time decay of europium as the EuEDTMP/HA ratio increases (λ_{exc} = 397 nm)

Figure 2.24 and Table 2.7 show the life-time luminescence decay of europium as we increase the Eu-EDTMP /HA ratio. Similarly to the study on the effect of the EuEDTMP/HA ratio on the europium crystal symmetry, the europium lifetime is fairly constant at a value above 0.900 ms until a 10/1 EuEDTMP/HA ratio when it decreases to

a value 0.600 ms approaching the value of free EuEDTMP in water of 0.419 ms (see Table 2.7, Table 2.8).

Table 2.8. Determination of the q value in EuEDTMP based on the life-time decay of Eu part of EuEDTMP complex in D_2O and H_2O.

	Eu-EDTMP in H_2O	**Eu-EDTMP in D_2O**	**Eu-EDTMP solid**
K (ms^{-1})	**2.387**	**0.574**	**1.006**
Life time (ms)	**0.419**	**1.742**	**0.994**
q	**1.875**		

The incorporation of europium into the EDTMP framework involves the binding of phosphonate groups from the EDTMP to the europium in order to satisfy the eight coordination needs of Eu(III). Upon adsorption to HA, the phosphonate groups may also bind to the HA or the Eu may bind to the phosphate of the HA. Mondry[2] showed that EuEDTMP complex strongly bind to CO_3^{2-} forming a stable Eu-EDTMP-carbonate complex with a life time decay rate of 864 μs at pH 7.5 (Figure 2.25).

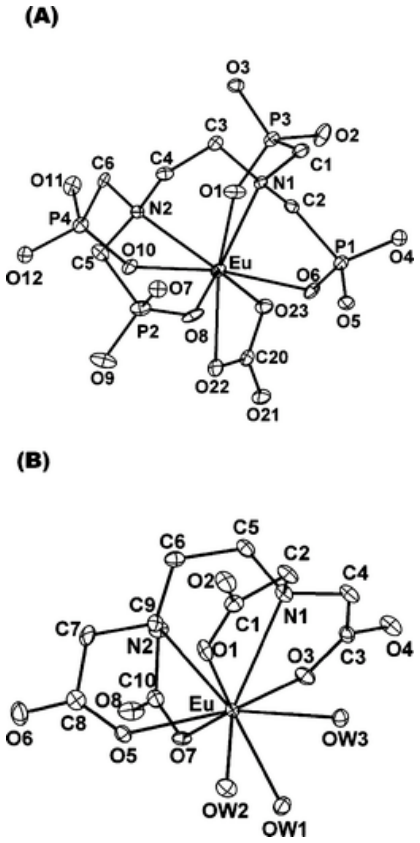

*Figure 2.25. Molecular structure of (A) $[Eu(EDTMP)(CO_3)]^{7-}$ and (B) $Eu(EDTA)(H_2O)]^{-}$ (Dalton Transactions **2006**, 4702-4710)* [2]

In our study, phosphate ions are present in the form of $HOPO_3^{2-}$ because we are working at physiological pH and the three values of H_3PO_4 pKas are 2.15, 6.86 and 12.32. Also, it is known that phosphate ions bind strongly to seven-coordinate lanthanide complexes. They are bidentate and displace solvent molecules from the metal center [14]. Therefore, one may hypothesize that similarly to the carbonate CO_3^{2-} ,phosphate ions may bind with EuEDTMP in the buffer and form a Eu-EDTMP-phosphate complex. Also, by looking at the ^{31}P NMR of EuEDTMP at a pH 7 we observed, from the broadness of the phosphate peak, the existence of the rapid exchange between the phosphonate arms and the europium, which emphasize the possibility of exchange

between a phosphonate arm by a phosphate ion. Therefore at low EuEDTMP concentration, one can suggest that the phosphate from the solution also participates in the exchange allowing the EuEDTMP to bind to the HA while maintaining its symmetry and preventing the possible "quencher", present in the aqueous media, to enter the coordination sphere and decrease the life time of europium. However as the EuEDTMP concentration increases the EuEDTMP appear to be either more affected by the solvent or less shielded by the phosphonated arms as their lifetime decay decreases to a value close to the lifetime decay of the solvated EuEDTMP. The coordination of another water molecule could be the source of this observed decrease of life decay and of the observed change of symmetry of the europium in the EuEDTMP structure.

The changes in symmetry and in life time decay of europium attest to a change in the EuEDTMP symmetry and environment, suggesting its binding to HA through the phosphate pendant arms from the EDTMP ligand. Nevertheless the transchelation of Eu from the EDTMP is not to be excluded as the life time and symmetry analysis only provide an average of the europium species present.

2.4.3- EuEDTMP adsorbed to HA using Tris-buffer as media

When using a media that contained phosphate, phosphate ions may also be a source of competition towards the binding site of the HA. To eliminate this competition, a set of experiments involving a TRIS buffer was performed. Tris buffer is a solution containing THAM, another name for $(HOCH_2)_3CNH_2$. Like the phosphate solution, TRIS solution is a widely used buffer to mimic physiological conditions[15,16]. In Table 2.9, we reported the

ICP results from the adsorption experiments of EuEDTMP onto HA in TRIS buffer. This adsorption levels off after a ratio of 5/1 Eu(EDTMP)/HA.

Table 2.9. *ICP results from the samples of europium(EDTMP) complex adsorbed to HA at various ratio of complex/HA inserted*

Experimental (EuEDTMP) /HA ratio	1:1	5:1	10:1	20:1
% Eu(EDTMP) versus HA	5.3	10.3	11.6	12.5

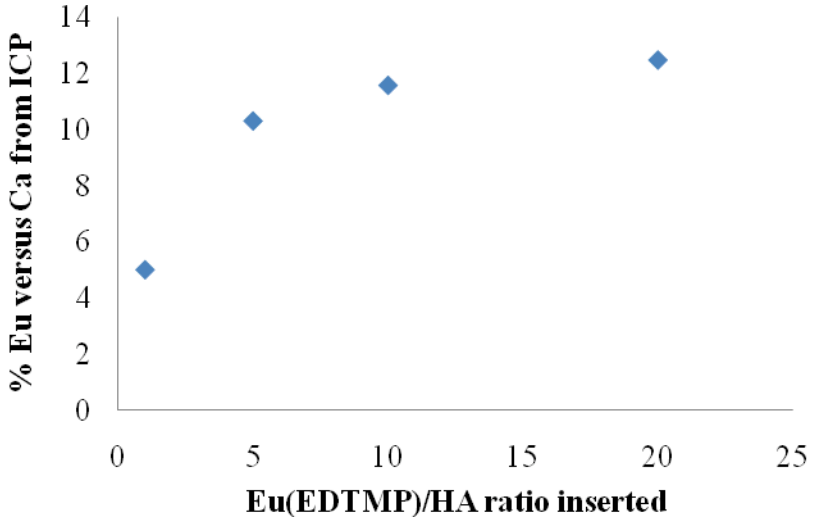

Figure 2.26. Plot visualizing the ICP results from the samples of europium(EDTMP) complex adsorbed to HA at various ratio of complex/HA inserted.

In Figure 2.26, the ICP analysis presents a rapid adsorption until 5:1 EuEDTMP/HA ratio, followed by a plateau. This result is somewhat similar to the EuEDTMP adsorption in a phosphate buffer where the adsorption is twice as low as in the Tris-buffer. We may

hypothesize a competition reaction between the phosphate ions from the phosphate buffer and the phosphonate group from the EuEDTMP toward the HA binding. As the only component of Tris buffer is the following amine $(HOCH_2)_3CNH_2$ any competitive binding of the buffer component can be excluded.

Now that the presence of europium in HA is established, its environment and symmetry will give us more information on the EuEDTMP binding onto the HA. Figure 2.27 and 2.28 show the symmetry and life time decay of europium in the sample. Figure 2.27 indicates that the symmetry remains unchanged with an emission ratio of 2.8 whereas its life time decay decreases slightly from 0.85 ms to 0.62 ms until a 10/1 ratio when it levels off (Figure 2.28). We need to keep in mind that the measured life time is the sum life times of all the contributions from the europium species present in the sample. Therefore as the observed lifetimes from our sample range from 780 μs to 630 μs, it shows that different species are present (Table 2.10). The life times are lower than the lifetime of the solid EuEDTMP (994 μs) and Eu doped HA (850-900 μs) and higher than the one of the EuEDTMP in water (419 μs), which suggests the mixture of different species: EuEDTMP adsorbed to HA, allowing one molecule of water to enter the coordination sphere while one phosphonate arm binds to HA, and possibly the presence of a lower lifetime species such as europium ion which would have transchelate from the ligand. Overall, both lifetime and symmetry of the europium do not change as the EuEDTMP/HA ratio increases, but reveal a difference of environment when compared to the free EuEDTMP.

Table 2.10. *Rate decays and life time decays of Eu(III) ion in the EuEDTMP complex adsorbed to HA in TRIS buffer.*

EuEDTMP/HA	**1/1**	**5/1**	**10/1**	**20/1**
K (ms^{-1})	**1.283**	**1.586**	**1.663**	**1.588**
Life time (ms)	**0.779**	**0.630**	**0.601**	**0.630**

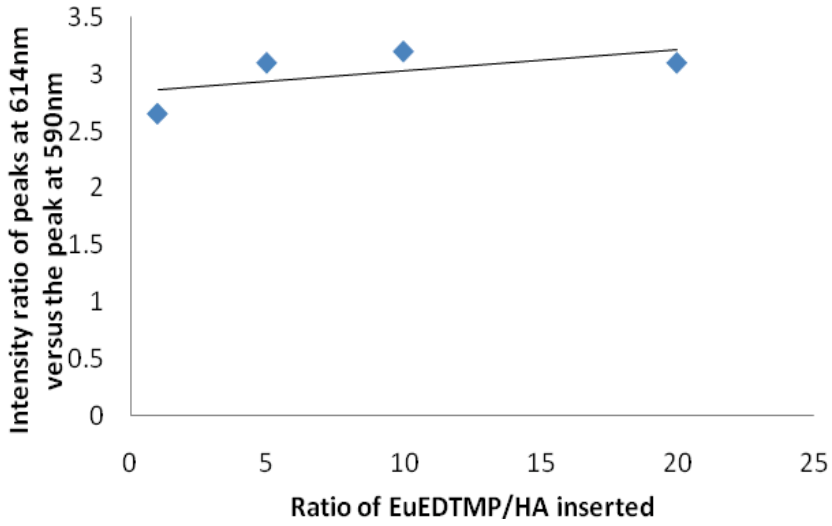

Figure 2.27. Intensity ratio of peak at 614 nm and peak at 590 nm attesting the symmetry of europium as the EuEDTMP/HA ratio increases (λ_{exc} = 397 nm)

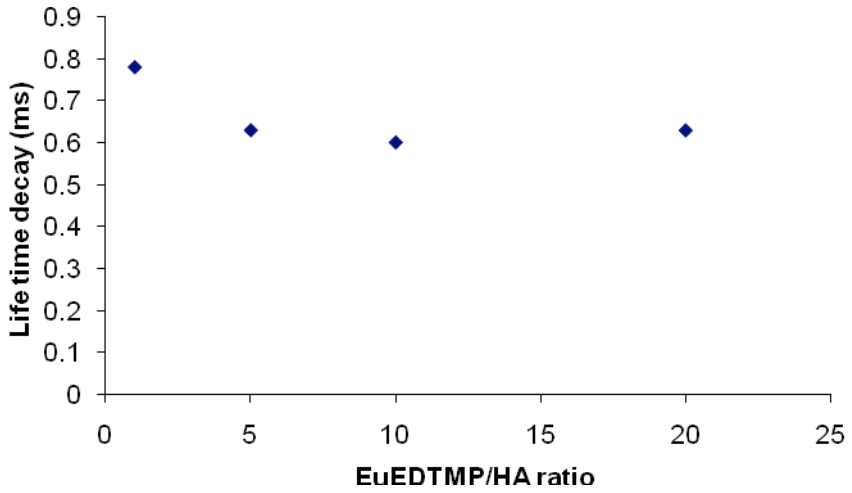

Figure 2.28. Lifetime decay of europium in EuEDTMP adsorbed to HA in TRIS buffer

2.4.4- EuDOTMP adsorbed to HA using phosphate buffer as media

Table 2.11 summarizes the europium content versus calcium or HA from the ICP analysis. We observed that as we increase the amount of EuDOTMP the amount of europium in the sample increases. As the Eu(DOTMP) is known to be very thermodynamically stable (Section 1.2.2) the assumption is that the europium is present as EuDOTMP.

Table 2.11. *ICP results from the samples of europium(DOTMP) complex adsorbed to HA at various ratio of complex/HA inserted*

Experimental (EuDOTMP) /HA ratio	1:1	5:1	10:1	20:1
% Eu(DOTMP) versus HA	0.54	1.65	3.05	6.03

Figure 2.30 shows the effect of the adsorption of EuDOTMP upon the crystal symmetry of europium. The LnDOTA, carboxylated congener of LnDOTMP, was found to have a quaternary axis of symmetry with an antiprism structure[17]. Geraldes et al. reported the structure of Gd(DOTMP) with an square antiprismatic structure (see Figure 2.29). Unlike our observations with the adsorption of EuEDTMP onto HA, the europium symmetry of EuDOTMP does not seem to be affected by the amount of complex. From literature, Ln(tript)[16] has been found to bind through its phosphonate pendant arm, releasing one bonding phosphonate from the europium. We can hypothesize that one phosphonate arm binds to the HA and allows a solvent molecule to bind to the Eu(III) to fill out the coordination sphere. The europium will then retain its structure symmetry (Figure 2.30).

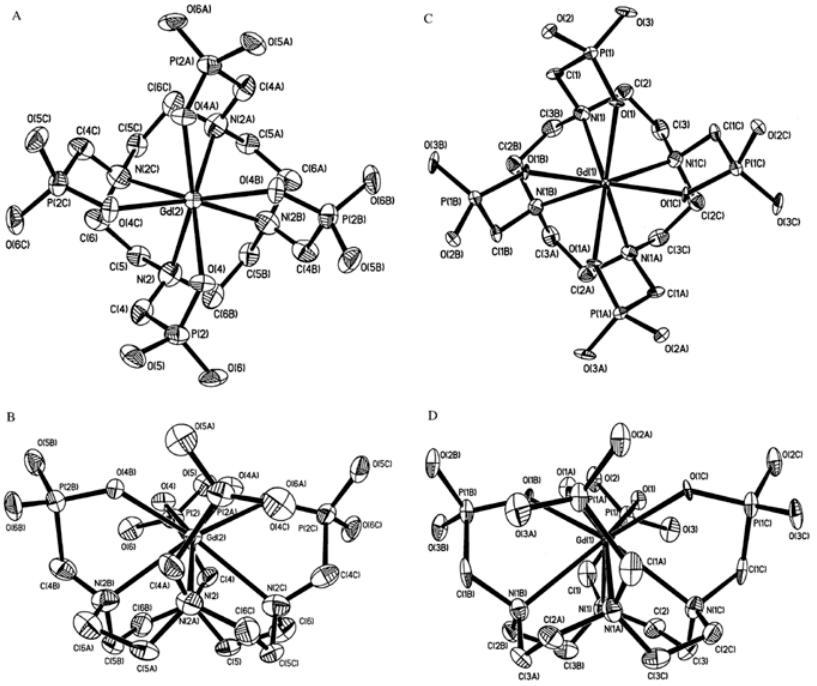

Figure 2.29. ORTEP diagrams of top and side view of Gd(DOTMP) complexes isomers with square-antiprismatic structure (*Eur. J. Inorg. Chem.* **2003**, *23*, 4179) [18].

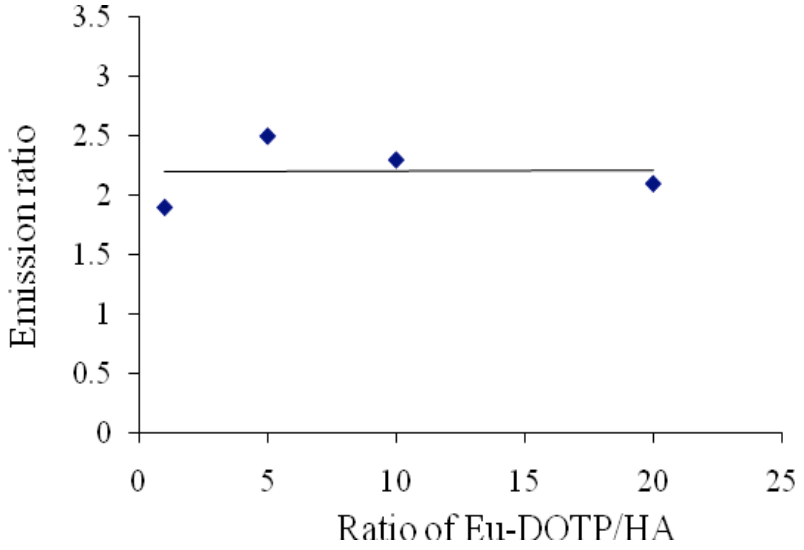

Figure 2.30. Intensity ratio of peak at 614 nm versus the peak at 590 nm from the europium emission spectrum (λ_{exc} = 397 nm).

In Table 2.12 and Figure 2.31 we observed a drastic decrease in the europium life time decay from 905 μs to 412 μs as we increase the Eu(DOTMP)/HA ratio. If we look at Table 2.13, we see that even in water the Eu(DOTMP) life time is not quentched and no water molecules are present in its inner sphere. In the DOTMP complex, the europium has a net 8 coordination provided by four nitrogen and four oxygen donor atoms. The encapsulation is very tight and does not allow solvent molecules to enter the europium coordination sphere. The value of q, the number of water molecules bound to Eu, calculated based on the rate of decay k_{D2O} and k_{H2O}, is equal to 0 (Table 2.13). The lifetime of EuDOTMP being the same in water, deuterated water or as a solid shows us how stable and shielded the EuDOTMP is. When looking at our results, we observed that the lifetime of europium gets greatly affected by the adsorption, which confirm its

binding. We know that biphosphonate groups bind strongly to mineral bone [19]. Ligands with methylphosphonate pendant arms have a better affinity to bone than their acetate derivative ligand[16]. Desreux and Sherry established some competitive binding when adding inorganic salts to LnDOTA complexes, and deducted the release of bound carboxylates from the lanthanide [20,21]. Also, Lukes reported that BPAMD, a derivative of DOTA with one biphosphonate moiety, is exclusively responsible for the binding to HA [22]. Therefore, this decrease of europium life time confirms the adsorption of the europium complex onto HA through its methylphosphonate arm, allowing the entry of water molecules in its first coordination sphere.

Table 2.12. Rate decays and life time decays of europium as EuDOTMP complex adsorbed to HA.

EuDOTMP/HA	**1/1**	**5/1**	**10/1**	**20/1**
k (ms^{-1})	**1.105**	**1.62**	**1.935**	**2.424**
Life time (ms)	**0.905**	**0.617**	**0.516**	**0.412**

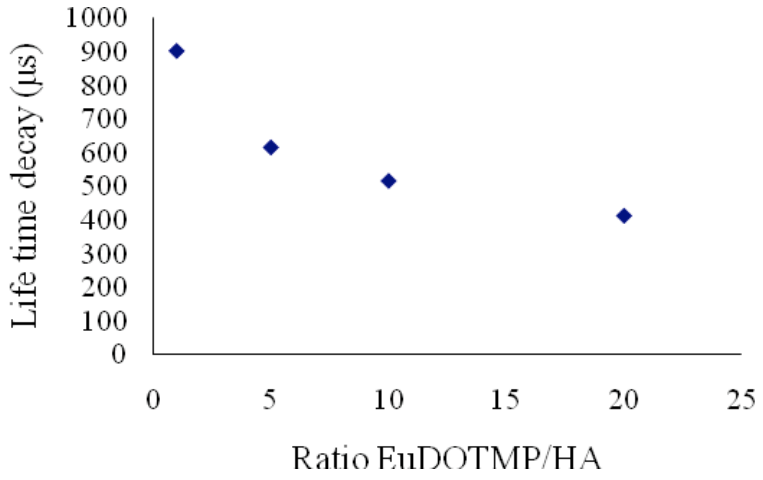

Figure 2.31. Life-time decay of europium as the EuDOTMP/HA ratio increases (λ_{exc} = 397 nm)

Table 2.13. Determination of the q value in EuDOTMP based on the life-time decay of Eu in the complex in D_2O and H_2O

	Eu-DOTP in D_2O	**Eu-DOTP in H_2O**	**Eu-DOTP solid**
k (ms-1)	**1.044**	**1.026**	**0.959**
Life time (ms)	**0.958**	**0.974**	**1.043**
q	**0**		

2.4.5- Conclusion

The two ligands studied in this work, EDTMP and DOTMP, formed europium complexes. Using a 1:1 europium-ligand molar ratio the macrocyclic and linear

complexes form at different rates. The macrocyclic complex is more thermodynamically stable and also formed at a slower rate, but once formed it shows the higher stability (Section 1.2.2). Due to the different stabilities of the EuEDTMP and EuDOTMP they behave differently towards their adsorption to HA. From luminescence studies, the europium environment and symmetry were monitored after each adsorption onto HA. The first set of experiments was conducted in phosphate buffer. One initial plateau and one plateau at 10/1 EuEDTMP/HA were observed, showing that EuEDTMP was indeed adsorbed to HA because the europium life time and the europium symmetry were decreasing with increase of the EuEDTMP content. In the first adsorption stage, we hypothesized the fact that phosphate ion could be responsible for maintaining of the europium symmetry and lifetime forming a EuEDTMP(HPO_4) complex. But as we increase the EuEDTMP content versus the HA, more competitive binding onto the HA surface may require more than one phosphonate arm to exchange between the HA and europium ion, leaving the luminescence of the europium ion more susceptible to being quenched.

Changing the buffer was shown to have an effect on the adsorption of EuEDTMP to HA. Using TRIS buffer (without phosphate), we observed the absence of the first plateau and a direct decrease of the europium life time while the symmetry of europium remained constant. Comparing with a different ligand such as DOTMP in a phosphate buffer, we observed similar results to the ones from the EuEDTMP adsorption in TRIS buffer. This shows the more stable character of EuEDTMP in TRIS buffer rather than in phosphate buffer.

As future work, the analysis of the adsorption by solid state ^{31}P NMR spectroscopy would be informative in order to assess the europium environment and binding through bond distance determination. The phosphorus nucleus interacts with the paramagnetic europium electron. As the electron-dipolar interaction is dependent on the distance of the P atom from the Eu centers the bond distances, the ^{31}P NMR spectrum will show side bands from which bond distances can be extracted. Also, the study of the europium transition $^5D_0 \rightarrow {}^7F_0$ using a high resolution phosphorimeter can inform us of the different europium-ion sites or europium species present in the sample due to the uniqueness of this transition for a given europium environment. Based on the number of bands and their positions, the symmetry and number of electron withdrawing groups can be evaluated.

2.5- References

(1) Vogel, A. I. *A Text-Book of Quantitative Inorganic Analysis including Elementary Instrumental Analysis*; 3rd ed.; Longmans, **1961**.

(2) Mondry, A.; Janicki, R. *Dalton Transactions* **2006**, 4702-4710.

(3) Sherry, A. D.; Ren, J.; Huskens, j.; Brücher, E.; Tóth, É.; Geraldes, C. F. C. G.; Castro, M. M. C. A.; Cacheris, W. P. *Inorg. Chem.* **1996**, *35*, 4604–4612.

(4) Shaw, W. J.; Long, J. R.; Dindot, J. L.; Campbell, A. A.; Stayton, P. S.; Drobny, G. P. *J. Am. Chem. Soc.* **2000**, *122*, 1709-1716.

(5) LeGeros, R. Z. *Monographs in Oral Science* **1991**, *15*.

(6) Mayer, I.; Layani, J. D.; Givan, A.; Gaft, M.; Blanc, P. *Journal of Inorganic Biochemistry* **1999**, *73*, 221-226.

(7) Get'man, E. I.; Loboda, S. N.; Tkachenko, T. V.; Ignatov, A. V.; Zabirko, T. F. *Functional Materials* **2005**, *12*.

(8) Webster, T. J.; Massa-Schlueter, E. A.; Smith, J. L.; Slamovich, E. B. *Biomaterials* **2004**, *25*, 2111-2121.

(9) Ternane, R.; Trabelsi-Ayedi, M.; Kbir-Ariguib, N.; Piriou, B. *Journal of Luminescence* **1999**, *81*, 165-170.

(10) Leung, Y.; Walters, M. A.; Legeros, R. Z. *Spectrochimica Acta, Part A: Molecular and Biomolecular Spectroscopy* **1990**, *46A*, 1453.

(11) Hezel, A.; Ross, S. R. *Spectrochim Acta* **1966**, *22*, 1949.

(12) Serret, A.; Cabanas, M. V.; Vallet-Regi, M. *Chem. Mater.* **2000**, *12*, 3836.

(13) Klink, S. I.; Hebbink, G. A.; Grave, L.; Oude Alink, P. G. B.; van Veggel, F. C. J. M. *J. Phys. Chem. A.* **2002**, *106,*3681.

(14) Pope, S. J. A.; Burton-Pye, B. P.; Berridge, R.; Khan, T.; Skabara, P. J.; Faulkner, S. *Dalton Trans.* **2006**, 2907.

(15) Grossmann, G.; Grossmann, A.; Ohms, G.; Breuer, E.; Chen, R.; Golomb, C.; Cohen, H.; Hagele, G.; Classen, R. *Magnetic Resonance in Chemistry* **2000**, *38*, 11-16.

(16) Marques, F.; Lurdes, G.; Campello, M. P.; lacerda, S.; Santos, I.; Lima, L. M. P.; Costa, J.; Antunes, P.; Delgado, R. *J. Inorganic Biochemistry* **2006**, *100*, 270.

(17) Aime, S.; Botta, M.; Ermondi, G. *Inorg. Chem.* **1992**, *31*, 4291.

(18) Avecilla, F.; Peters, J. A.; Geraldes, C. F. G. C. *Eur. J. Inorg. Chem.* **2003**, *23*, 4179.

(19) Nancollas, G. H.; Tanga, R.; Phipps, J.; Hennemana, Z.; Guldea, S.; Wua, W.; Mangooda, A.; Russell, R. G. G.; Ebetin, F. H. *Bone* **2006**, *38*, 617-627.

(20) Jacques, V.; Desreux, J. F. *Inorg. Chem.* **1994**, *33*, 4048

(21) Marques, M. P.; Geraldes, C. F. G. C.; Sherry, A. D.; Merbach, A. E.; Powell, H.; Pubanz, D.; Aime, S.; Botta, M. *J. Alloys Compd* **1995**, *225*, 303.

(22) Kubíek, V.; Rudovský, J.; Kotek, J.; Hermann, P.; Vander Elst, L.; N. Muller, R.; Kolar, Z. I.; Wolterbeek, H. T.; Peters, J. A.; Lukeš, I. *J. Am. Chem. Soc.* **2005**, *127*, 16477.

Chapter 3: Influence of the Lanthanide Ion and Solution Conditions on Formation of Lanthanide Well-Dawson Polyoxomethalate.

3.1- Introduction

3.1.1- General introduction

Polyoxomethalates are robust metal oxide cluster. One of their characteristic is the possibility of facile incorporation of transition metal ions. Their size charge and redox potential can be easily modified,[1] which has been of great interest as catalysts for oxidation and acid-dependant reactions.[2] Professor Michael Pope was the pioneer in the field by examining the solution and solid state chemistry of lanthanide (Ln) polyoxometalates. Lanthanide polyoxometalates have received a lot of interest for various reasons. Because lanthanides and actinides have analogue behaviors, analytical methods have been developed and explored for lanthanide studies and adapted to actinides.[3-14] Due to their homogeneous crystalline structures polyoxometalates are excellent models for minerals and colloids and can be studied at the molecular level.[15-17] Therefore, solution speciation studies and solid state structural studies of Ln(POM) can provide good models for the understanding of actinide interactions with mineral compounds in the geosphere. When designing separation and storage strategies for actinides, these factors become crucial. The valence controlling aspects of actinide heteropolymetalates [18-23], along with the solid state structures of actinide polyoxomethalates by X-ray crystallography and X-ray spectroscopy [7,24-27] have been well studied. Nevertheless, speciation in aqueous solution has not been examined greatly. Catalysis materials chemistry and nanotechnology [28-30] are domains where lanthanide

POMs are of great use. When combined with the POM, lanthanide ions can give a unique functionality to the POMs. For example, the use of lanthanide ions to ‘‘link’’ POMs into solid state oligomers [31,32] and large wheel structures [14,33,34] has been reported in solid-state X-ray crystal structures. Also, from solution studies lanthanide ions can be used as connectors and transfer agents for different monolacunary POMs [3]. Other useful functionalities can be provided when a lanthanide is incorporated into POMs, for example, in creation of luminescent, magnetic Lewis acid catalytic centers. We are interested in Ln complexes of monovacant polyoxometalate stems in order to identify stable 1:1 Ln:POM complexes for specific applications, such as catalysis and development of hybrid organic Ln POMs and other potential applications related to materials sciences. Therefore, a good understanding of solution speciation chemistry is critical. Because of the existence of multiequilibria, polyoxomethalate composition in aqueous solution depends on different variables such as the pH of the solution, the countercations present, the concentration and aging of the solution. Complexes formed with lanthanides ions also demonstrate dynamic behavior in aqueous solution. A series of studies have been reported by Pope *et al.* regarding the speciation of lanthanide with POMs.[8,32,35,36] We are reporting herein some solid-state chemistry and solution speciation of lanthanide α2-$P_2W_{17}O_{61}^{-10}$ complexes and track the changes in structure and in solution behavior across the lanthanide series and as a function of solution conditions.

3.1.2- Background

The general formula of Polyoxometallates (POMs) is $[M_xO_y]^{n-}$, where the metal can be molybdenum (Mo), tungsten (W), vanadium (V), titanium (Ti) and aluminium (Al) for the most encountered. They are robust metal oxide cluster, water and air stable. They are chemically robust and can be easily modified with respect to incorporation of transition metal ions, charge, size, redox potential, and solubility.[1] They can be synthesized easily under aqueous conditions, and they are paired with various ammonium or metal cations (Cs, Na, K, Li…). Regarding Keggin POMs, they originally were discovered with tungsten but have been expanded to the general form of ($XM_{12}O_{40}^{n-}$). Their interesting structure makes them desirable for different purposes. This supramolecular structure is composed of repeat units of the octahedron. At the vertices of each of these octahedra sites oxygen atoms are linked to each other with the presence of a metal atom at the center. The oxygen atoms may serve as terminal and bridging ligands connecting the shared octahedral vertices. The complexes are three tiered structures with an empty space at the center that can accommodate the incorporation of a variety of compounds or metal ions. We can then prepare Keggin half-sandwiches by removing the top or bottom triad of octahedral and expose the central catalyst.

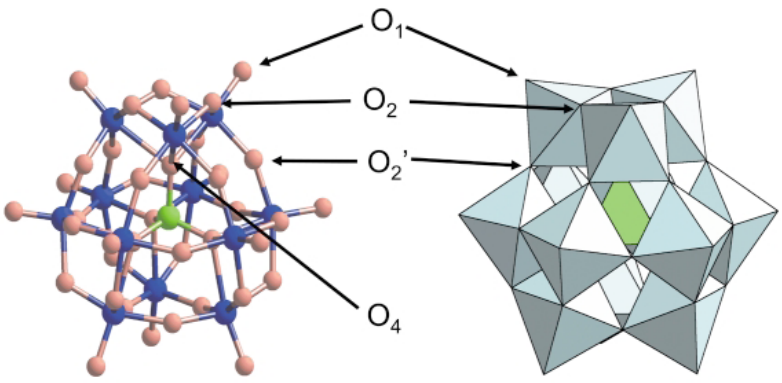

Figure 3.1. Ball and stick and polyhedral representation for an α-$[XM_{12}O_{40}]^{-n}$ Keggin anion. Blue and green identify cations while red is used for oxo ions (Chem. Rev. 1998 98 199)[1]

3.1.3- POM 'PW_{17}' with lanthanide

For the past decade, the solid-state and aqueous chemistry of lanthanide complexed with monovacant lacunary polyoxometalates has been analyzed and reported. This chapter has been mostly focus on the α2-$P_2W_{17}O_{61}^{-10}$ (α2-POM) and α1-$P_2W_{17}O_{61}^{-10}$ (α1-POM) isomers. They derived from the Wells-Dawson ion α-$P_2W_{18}O_{62}^{-6}$ in which the ion is incorporated into the "cap" and "belt" regions of the α2- and α1-POMs, respectively. [11,31,32,35,37-42]

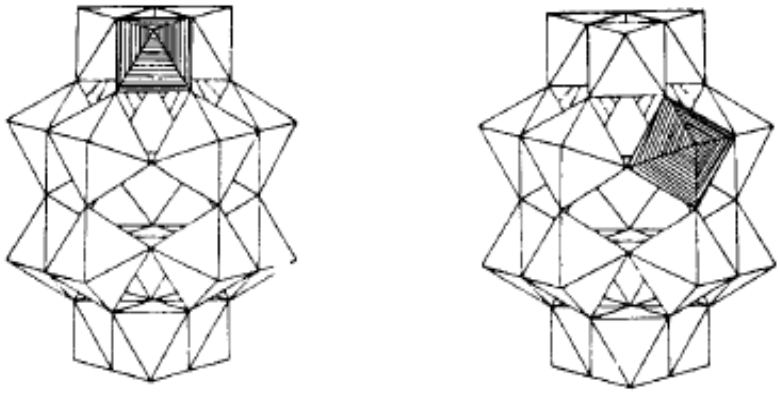

Figure 3.2. Polyhedral representation of the α2-$P_2W_{17}O_{61}^{-10}$(left) and α1-$P_2W_{17}O_{61}^{-10}$(right) Keggin ions.

In 1971, 1:2 Ln: α2-$P_2W_{17}O_{61}^{-10}$, (Ln(α2-$P_2W_{17}O_{61}^{-10}$)$_2$, was discovered by Peacock and Weakley [43]. In this complex the lanthanide is bound to two α2-$P_2W_{17}O_{61}^{-10}$ moieties. Crystal structures show that these POM units are arranged in a cis conformation.[42,44] Three decades later, the 1:1 Ln:α2-$P_2W_{17}O_{61}^{-10}$ species has been reported [11,40,41,45] and it is consider as a "2:2 self-associated dimer" with a formula of Ln$(H_2O)_n$(α2-$P_2W_{17}O_{61}^{-14}$)$_2$ (n = 3,4) in the solid state. In solution, the dimer dissociates to form a 1:1 monomer in equilibrium with the 1:2 dimer. This species will be referred to as the 1:1 Ln:α2-$P_2W_{17}O_{61}^{-10}$ species, in this thesis.

Some studies have suggested that the ionic radius of a lanthanide and the solution condition that it is in have an influence on the structure and the solution equilibria of α2-POM complexed with lanthanide. Pope shows, using solid state X-ray crystallography, that the Ce(α2-$P_2W_{17}O_{61}^{-7}$) species is a "cap to cap" (2:2) dimer. In this dimer, the Ce(III) is nine coordinate bound to four oxygen atoms from the α2-$P_2W_{17}O_{61}^{-10}$ unit, four water

molecules and a terminal W=O of an adjacent Ce(α2-$P_2W_{17}O_{61}^{-10}$) unit [11]. This complex also possesses a capped square antiprismatic coordination geometry. In solution ^{183}W NMR and ^{31}P NMR spectroscopy demonstrate that the dimer dissociates into a monomeric species in equilibrium with the 1:2 Ce(III):(α2-$P_2W_{17}O_{61}^{-10}$) species. Also Kortz isolated the La analog which also showed the "cap to cap" dimer in their solid-state crystal structures where the lanthanum is bound to acetate anions to complete the coordination sphere of La(III) and provide an organic-inorganic hybrid [40]. Regarding the mid-late lanthanides, their behaviors are slightly different. In solid state, the Nd(III) [40], Tb(III) [45], Eu(III) [41] and Ho(III) [45] analogs show a different coordination than those observed for the ealier lanthanides, previously mentioned. For the mid-late lanthanides the coordination number is 8, with coordination to four oxygen atoms from the α2-$P_2W_{17}O_{61}^{-10}$, three water molecules and a terminal W=O from the "belt" region of the adjacent α2-$P_2W_{17}O_{61}^{-10}$. They form a "cap to belt" 2:2 dimer. In solution the dimmers dissociate to form a monomeric 1:1 species as suggested by the ^{183}W NMR spectra for Nd(III) and Lu(III) analogs and the luminescence lifetime experiments for Eu(III) analog. Also, from the ^{31}P NMR spectrum and the luminescence studies of Eu(III): (α2-$P_2W_{17}O_{61}^{-10}$) aqueous solution at pH 6, a trace amount of the 1:2 species was observed due to the presence of an equilibrium on a micro-molar level between 1:1 Ln(III) α2-$P_2W_{17}O_{61}^{-10}$ and 1:2 α2-$P_2W_{17}O_{61}^{-10}$. Nevertheless, this equilibrium has not been observed for the later lanthanides [41]. In this chapter we document and attempt to understand the effects of the lanthanide ionic radius and of the solution conditions (pH, countercation and concentration) on the solid-state structure and on the solution

speciation in order to identify parameters that impact the structural differences across the series.

3.1.4- Purpose

In this chapter we will introduce the α2-$P_2W_{17}O_{61}^{-10}$ speciation with lanthanide such as Pr, Eu and Yb. The preliminary study by Cheng Zhang on crystal structure lead us to direct our research towards the speciation of the lanthanide polyoxomethalate through the collection of detailed high resolution ^{31}P NMR. The objective is to identify parameters that impact the structural differences across the series in aqueous solution speciation, specifically, the 1:1 to 1:2 equilibria processes. In this study, we document and attempt to understand the influence of the lanthanide ionic radius and of solution conditions (pH, countercation and concentration) on the solid-state structure and on the solution speciation.

3.2- Experimental section

3.2.1- Materials

All reagents were commercially available and used without further purification. Nanopure water was obtained from a Millipore Reverse Osmosis Direct-Q System. The lacunary $K_{10}[\alpha_2\text{-}P_2W_{17}O_{61}]$ and Li_{10} $[\alpha_2\text{-}P_2W_{17}O_{61}]$ anions salts were prepared according to published methods and were identified by ^{31}P NMR [46]. All reagents were obtained from commercial sources and used as received.

3.2.2- ^{31}P NMR speciation experiments as a function of solution conditions

1. Standardization of $Li_{10}[\alpha 2\text{-}P_2W_{17}O_{61}]$. The standardization procedure by titration with Co(II) has been reported [38]. Three titrations were run for each standardization, the agreement was within 1%.

2. Standardization of the lanthanide (III) ions, $LnCl_3$, for NMR experiments was accomplished by complexometric titration using xylenol orange as an indicatior [47].

3. Collection of NMR Data. All NMR spectra were recorded on a JEOL GX-400 spectrometer with 5 or 10 mm tubes. Resonance frequencies are 161.8 MHz for ^{31}P and 16.7 for ^{183}W. Chemical shifts are given with respect to external 85% H_3PO_4 for ^{31}P and 2.0 M Na_2WO_4 for ^{183}W. Typical acquisition parameters for ^{31}P spectra included the following: spectral width, 10,000 Hz; acquisition time, 0.8 s; pulse delay, 1 s; pulse width, 15 ls (50_ tip angle). From 200 to 1000 scans were required. The pulse delay of 1 s was sufficient for reproducible data for the equilibrium constant determination. The more negative chemical shifts denote upfield resonances.

Experiments 1 and 2 were carried out for Pr(III), Eu(III) and Yb(III). Examples of prototypical reactions for Pr(III) are given below.

Reactions of Pr^{3+}, Eu^{3+} and Yb^{3+} with $[\alpha_2\text{-}P_2W_{17}O_{61}]^{10-}$ (1:1 stoichiometry) as a function of counter cation monitored by ^{31}P NMR

Buffer solutions of LiOAc (1 M), NaOAc(1 M), KOAc(1 M) and CsOAc(0.5 M) were prepared at pH 4.75. Standardized $Li_{10}[\alpha_2\text{-}P_2W_{17}O_{61}]$ solution (0.09 mL, 0.2311 M),

standardized $PrCl_3$ solution (0.0181 mL, 1.15 M) and 0.192 mL of D_2O were each placed into five 5 mm NMR tubes, followed by 0.3 mL of either H_2O or buffer. The final ion concentration was 0.5 M in each solution containing Li^+, Na^+ or K^+ and 0.25 M for Cs^+. The solutions were shaken for 5 min, incubated at room temperature for 30 min, after which the ^{31}P NMR spectra were recorded. The data are shown in Figures 3.3, 3.4 and 3.5 for Pr(III), Eu(III) and Yb(III), respectively. The final concentrations are: [Pr] = [α_2-$P_2W_{17}O_{61}$] = 34.6 mM, [Li^+] = 0.35 M (due to countercation); [Li^+] (due to added cation), [Na^+] or [K^+] = 0.5 M; [Cs^+] = 0.25 M.

Reaction of* Pr^{3+}, Eu^{3+} and Yb^{3+} *with* $[\alpha_2\text{-}P_2W_{17}O_{61}]^{10-}$ *(1:1 stoichiometry) as a function of pH monitored by* ^{31}P *NMR at constant ionic strength, with* Na^+ *counterion

Solutions of NaOAc (0.5 M) at five different pH values were each prepared (2, 4, 6, 8, 10) (30% D_2O) (pH 2 and 10 were adjusted by dilute HCl and NaOH respectively). Standardized $Li_{10}[\alpha_2\text{-}P_2W_{17}O_{61}]$ solution (0.09 mL, 0.2311 M) and 0.0181 mL of standardized $PrCl_3$ solution (1.15 M) were placed into five 5 mm NMR tubes, and 0.5 mL of one of the above NaOAc solutions was added into the NMR tubes to give five samples buffered at the five pH values. The NMR tubes were shaken for 5 min and incubated at room temperature for 30 min, then the ^{31}P NMR spectra were recorded and the data are shown in Figures 3.6, 3.7 and 3.8 for Pr(III), Eu(III) and Yb(III), respectively. The pH recorded after the NMR measurements did not change significantly. The final concentrations are: [Na^+] = 0.41 M; [Li^+] = 0.34 M, [Pr]=[$\alpha_2-P_2W_{17}O_{61}$]=34 mM.

Reaction of Pr^{3+} with $[\alpha_2\text{-}P_2W_{17}O_{61}]^{10-}$ (1:1 stoichiometry) as a function of cation concentration monitored by ^{31}P NMR

Solutions of NaOAc (0.04 M, 0.2 M, 0.5 M, 1.0 M, 2.0 M) at pH 4.75 were prepared. Standardized $Li_{10}[\alpha_2\text{-}P_2W_{17}O_{61}]$ solution (0.09 mL, 0.2311 M), $PrCl_3$ (0.0181 mL, 1.15 M) solution and 0.192 mL of D_2O were placed into five 5 mm NMR tubes followed by the addition of 0.3 mL of each buffer solution into the above five 5 mm NMR tubes individually. The solution in the NMR tubes were shaken for 5 min and incubated at room temperature for about 30 min. The ^{31}P NMR spectra were recorded; the data are shown in Figure 3.9. The final concentrations are: $[Li^+]$ = 0.34 M, [Pr] = $[\alpha_2\text{-}P_2W_{17}O_{61}]$ = 34.7 mM $[Na^+]$ = varies from 0.02 M to 1.6 M.

Reaction of Pr^{3+} with $[\alpha_2\text{-}P_2W_{17}O_{61}]^{10-}$ (1:1 stoichiometry) as a function of Ln $[\alpha_2\text{-}P_2W_{17}O_{61}]$ concentration monitored by ^{31}P NMR

Solutions of $Li_{10}[\alpha_2\text{-}P_2W_{17}O_{61}]$ and $PrCl_3$ of 1:1 stoichiometry were prepared at 50 mM, 100 mM, 150 mM, 200 mM, and 250 mM concentration. The pH ranged from 5.77 (50 mM) to 4.92 (250 mM). The ^{31}P NMR data are shown in Figure 3.10. The final concentrations are: $[Pr^{3+}]$ = $[\alpha_2\text{-}P_2W_{17}O_{61}]$ ranges from 50 mM, 100 mM, 150 mM, 200 mM, 250 mM; $[Li^+]$: 500 mM, 1 M, 1.5 M, 2.0 M, 2.5 M.

Solution speciation chemistry: impact of counterion, pH and concentration

In all our experiments ^{31}P NMR was used as a probe for POM complex speciation based on solution conditions. The 1:1 to 1:2 Ln(III):α2-$P_2W_{17}O_{61}$ equilibria for the early, mid and late lanthanides appears to be influenced by the solution conditions: pH, counterion and concentration. Thanks to their paramagnetic properties, Pr (III), Eu (III) and Yb(III), were selected as representative lanthanides for early, mid and late lanthanides in the ^{31}P NMR experiments. Their chemical shift dispersion allows clear observation and identification of the solution species. In order to perform these studies, we need the chemical shift values for the 1:1 and 1:2 complexes which were determined in this and previous work [36,39,41] and reported in Table 3.1.

Table 3.1. Multinuclear NMR chemical shifts (δ, ppm) for the 1:1 and 1:2 Ln:α_2-$P_2W_{17}O_{61}^{10-}$ complexes in 0.5 M sodium acetate buffer at pH 4.75 and 25°C with concentration of polyoxometalate 50 mM

	1:1Ln:α_2-P_2 $W_{17}O_{61}^{10-}$		1:2Ln:α_2-P_2 $W_{17}O_{61}^{10-}$	
Ln	P1	P2	P1	P2
La	-7.52	-13.56	-7.42	-13.58
Ce	-14.40	17.26	-13.92	-13.98
Pr	-11.91	-13.47	-8.41	-13.11
Nd	-20.74	-14.66	18.50	-14.36
Eu	7.32	-12.43	3.73	-12.73
Yb	32.78	-9.92	39.15	-8.28
Lu	-8.03	-13.52	-7.72	-13.42

In addition, the dissociation of the 2:2 dimmer into a 1:1 monomer, (in equilibrium with the 1:2 species for Ce(III)) in aqueous solution has been confirmed by combinations of ^{183}W NMR spectroscopy for the Ce(III) [11], Nd(III) and Lu(III) analogs and luminescence spectroscopy for the Eu(III) analogs [41].

3.3- Results and discussion

3.3.1- Results

3.3.1.1- Ln: α2-$P_2W_{17}O_{61}^{-10}$ speciation as a function of counter cation

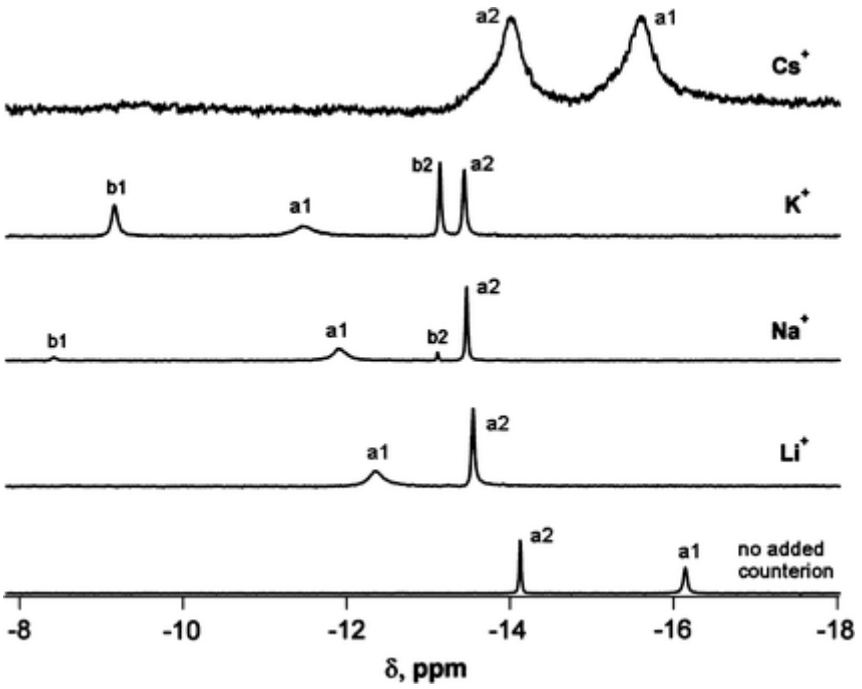

Figure 3.3. Reaction of Pr^{3+} with $Li_{10}[\alpha2\text{-}P_2W_{17}O_{61}]$ (1:1 stoichiometry) as a function of counter cation, pH 4.75, the concentration of Li^+, Na^+, K^+ = 0.5 M. Concentration of Cs^+ = 0.05 M.

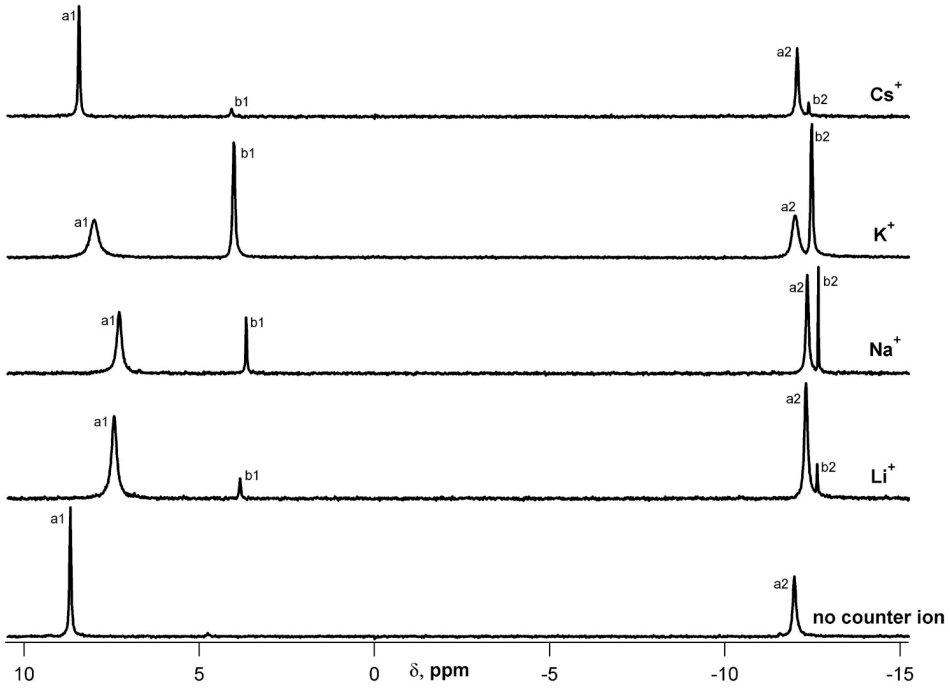

Figure 3.4. Reaction of Eu^{3+} with Li_{10}[α2-$P_2W_{17}O_{61}$] (1:1 stoichiometry) as a function of counter cation, pH 4.75, the concentration of Li^+, Na^+, K^+ = 0.5M . Concentration of Cs^+ = 0.05M

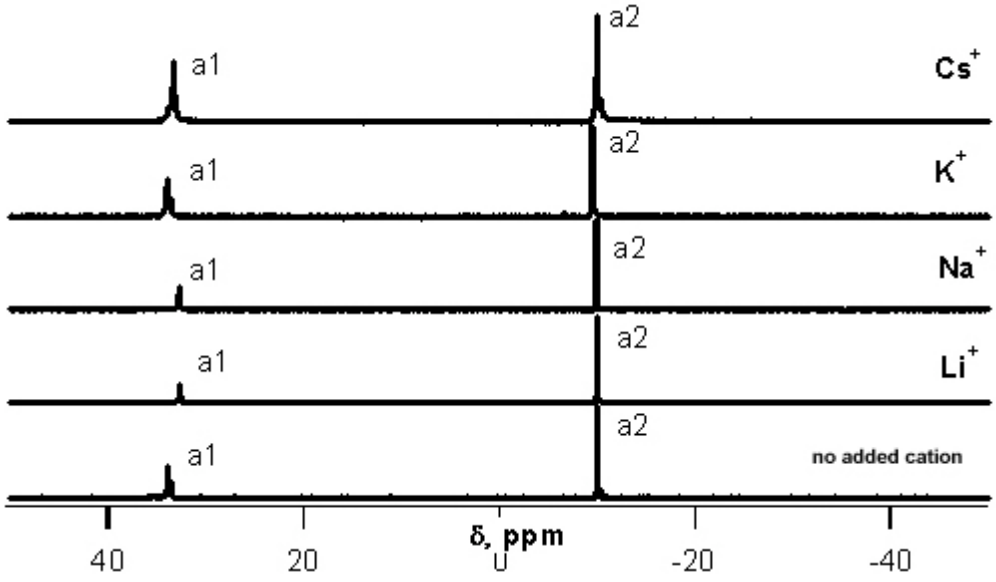

Figure 3.5. Reaction of Yb^{3+} with Li_{10}[α2-$P_2W_{17}O_{61}$] (1:1 stoichiometry) as a function of counter cation, pH 4.75, the concentration of Li^+, Na^+, K^+ = 0.5M . Concentration of Cs^+ = 0.05M.

Figure 3.3 shows the ^{31}P NMR data for the reaction of Pr(III) with $Li_{10}[\alpha 2\text{-}P_2W_{17}O_{61}]$ in 1:1 stoichiometry with different counterions. The cations used are Li^+, Na^+, K^+ and Cs^+ cations. Their concentration in the buffer are 0.5 M for Li^+, Na^+ and K^+ and 0.05 M for Cs^+ to prevent precipitation. If no cations are added, the 1:1 species shows two chemical shifts in the ^{31}P NMR spectrum, a1 and a2. The peak the most down field is designated a1. It is broader due to the fact that it corresponds to the phosphorus closest to the paramagnetic lanthanide. When we added additional cations, we see the appearance of 2 other phosphorus resonances, b1 and b2, from the 1:2 complexes. The peak b1 is broader than b2 due to the closeness of its assigned phosphorus to the lanthanide. This peak b1 shifts as we change the cations, which shows that the cations influence the chemical shift and speciation. Indeed, addition of Li^+. Na^+ and K^+ cause the a1 peak to shift downfield. For praseodymium, it is observed that the quantity of the 1:2 species increases with the counter cation radius from Li^+ to K^+ as shown by the increase in intensity of b1 and b2 peaks. The ^{31}P NMR spectrum of the Cs^+ experiment is similar to the one where no counterion is added, due to the low Cs^+ concentration required to prevent from precipitating. Under identical condition, the europium(III) analog behaves similarly to the Pr(III) (Figure 3.4). However for Eu(III) analog, we observed that the peaks assigned for 1:2 species , b1 and b2, are more distinct upon addition of the cations Li^+, Na^+, and K^+. These peaks increase with increasing the cation radius added. For Ytterbium no change is observed as we change the cation, the 1:1 species being the only species present (Figure 3.5).

3.3.1.2- Ln: α2-$P_2W_{17}O_{61}^{-10}$ speciation as a function of pH

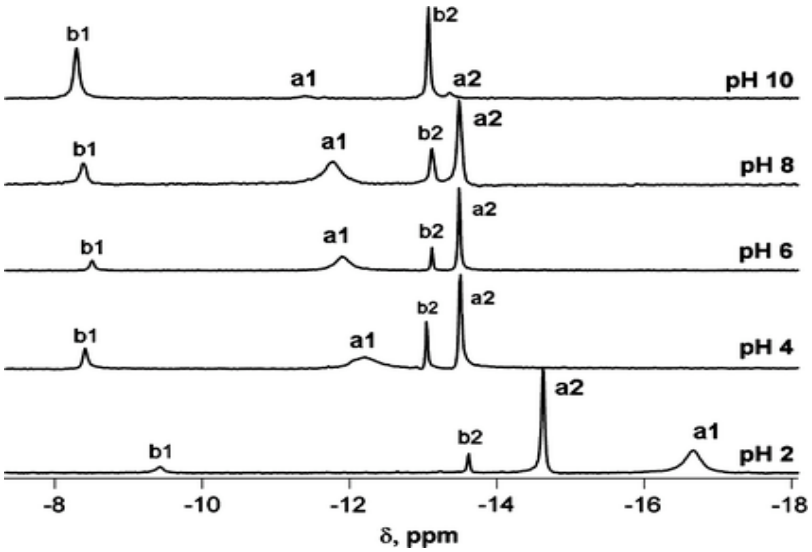

Figure 3.6. Reaction of of Pr^{3+} with $Li_{10}[\alpha2\text{-}P_2W_{17}O_{61}]$ (1:1 stoichiometry), 0.5 M NaOAc, as a function of pH.

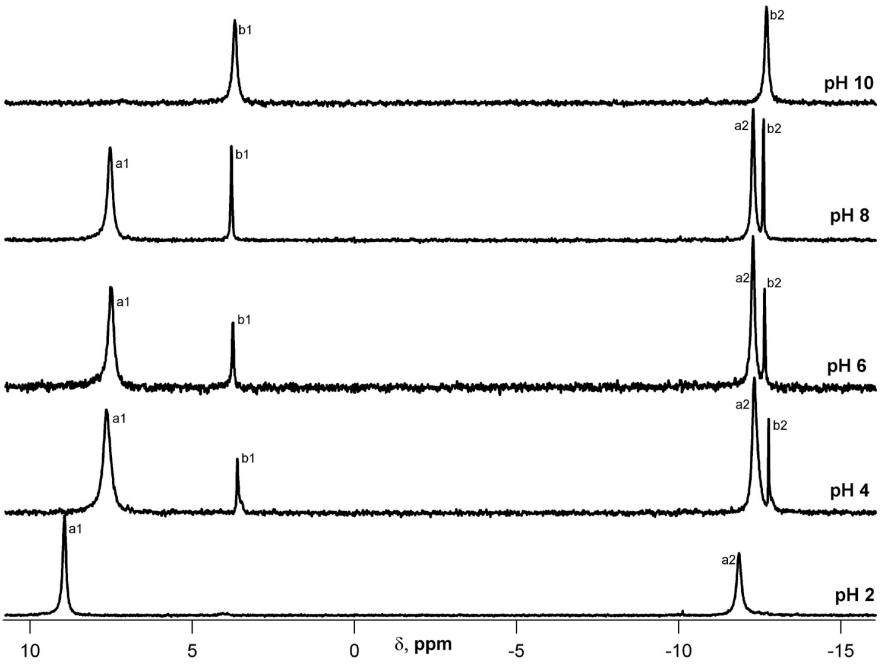

Figure 3.7. Reaction of Eu^{3+} with $Li_{10}[\alpha2\text{-}P_2W_{17}O_{61}]$ (1:1 stoichiometry) as a function of pH at constant ionic strength, with Na^+ counterion. ($[Li^+]$= 0.34 M, $[Na^+]$ =0.41 M, $[Eu^{3+}] = [\alpha_2\text{-}P_2W_{17}O_{61}^{-10}]$= 34 mM)

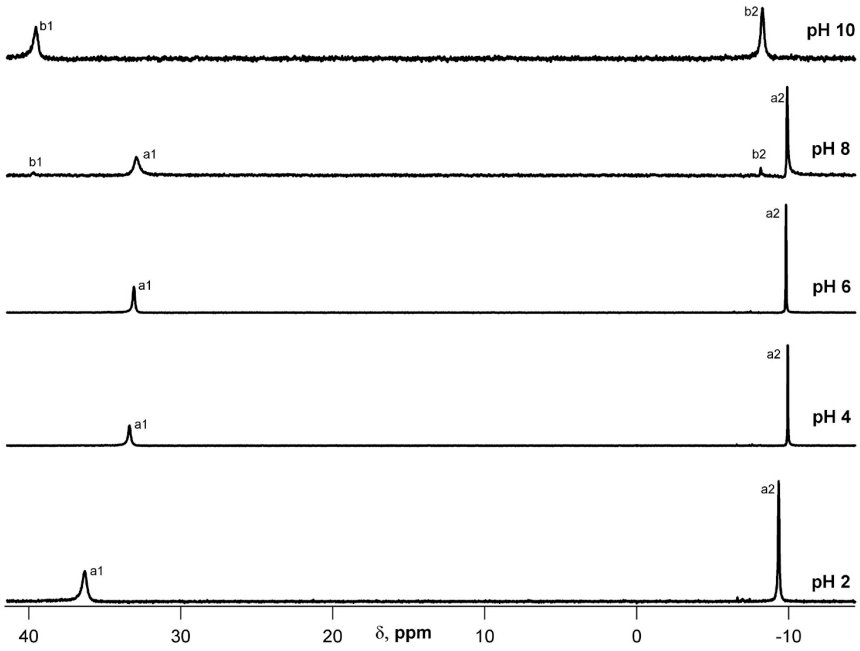

Figure 3.8. Reaction of Yb^{3+} with Li_{10}[α2-$P_2W_{17}O_{61}$] (1:1 stoichiometry) as a function of pH at constant ionic strength, with Na^+ counterion. ([Li^+]= 0.34 M, [Na^+] =0.41 M, [Yb^{3+}] = [α2-$P_2W_{17}O_{61}^{-10}$]= 34 mM)

Figures 3.6, 3.7, 3.8 show the 1:1 Ln: α2-$P_2W_{17}O_{61}^{-10}$ with Pr(III), Eu(III) and Yb(III) respectively in 0.5 M Na^+ as a function of pH. The variation of pH from pH 4 to pH 10 does not seem to affect samples of praseodymium (III) and europium(III) which show the 1:1 and the 1:2 species. Samples of Pr(III) (Figure 3.6) and Eu(III) (Figure 3.7), at all pH values, show the 1:1 and 1:2 species with little variation from pH 4 to pH 10. At basic pH the amount of 1:2 is high due to the competition between the OH^- ions and the POM for the Ln. Lanthanides are known to form highly stable hydroxides or oxides they detached from the POM which binds to a 1:1 Pr: α2-$P_2W_{17}O_{61}^{-10}$ species and to form a 1:2 species. Colloidal lanthanides are often undetectable to the eye which is why no precipitate was observed in the NMR tubes. The Yb analog behaves differently from the Eu and the Pr analogs: the 1:1 species persists until pH 8-10 (Figure 3.8) when the 1:2 begins to form.

3.3.1.3- Eu:α2-$P_2W_{17}O_{61}^{-10}$ speciation as a function of pH

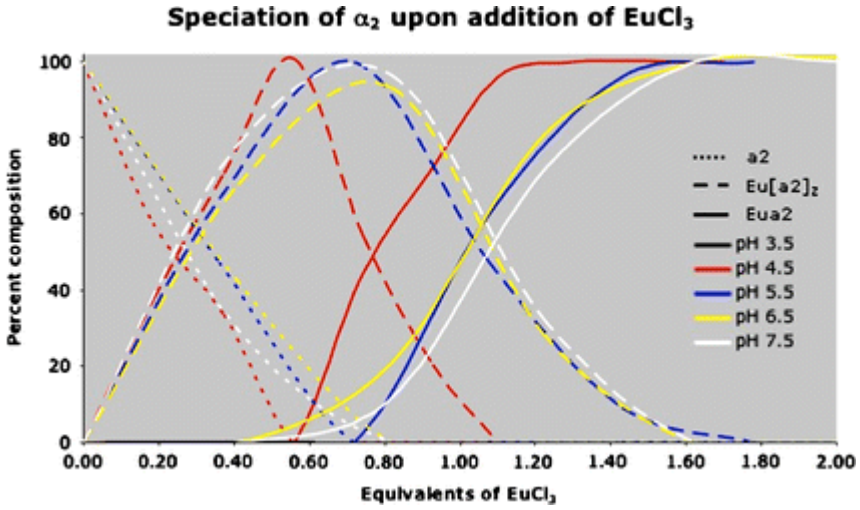

Figure 3.9. Titration of 25 mM α_2-$P_2W_{17}O_{61}^{10-}$ with Eu(III) at 0.005 M Na^+ as a function of pH[48] *(J. Cluster Science **2006** 17 389)*

The data shown in Figure 3.9 have been collected by Ben Burton-Pye. These data represent the speciation dependence on pH for the Eu:α2-$P_2W_{17}O_{61}^{-10}$ species. It is a series of titration experiments where the Eu(III) is added to the a_2-$P_2W_{17}O_{61}^{-10}$ ligand without addition of cations. In this titration, as expected, the ligand decreases with the addition of Eu(III), and the 1:2 species increases, followed by the 1:1 species. Also, as the pH increases, the range of the 1:2 species increases which is consistent with the previous pH studies (Figure 3.7). This suggests that pH plays an important role in shifting the 1:1 ↔ 1:2 equilibrium to the right.

3.3.1.4- Pr: α2-$P_2W_{17}O_{61}^{-10}$ speciation as a function of [Na^+] concentration.

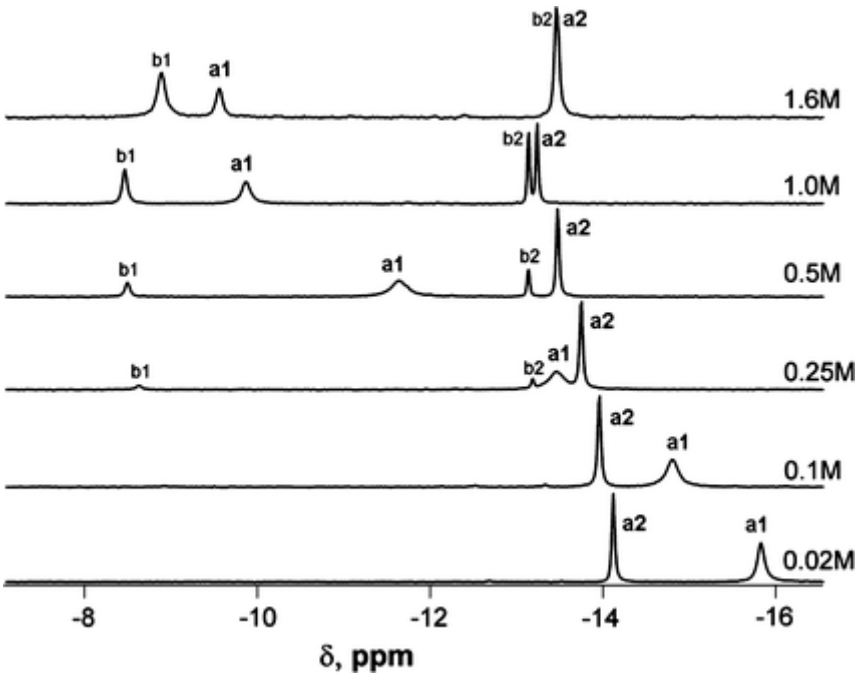

Figure 3.10. Reaction of Pr^{3+} with Li_{10}[α2-$P_2W_{17}O_{61}$] (1:1 stoichiometry) as a function of concentration of NaOAc, pH 4.75, [Pr^{3+}] = [(α2-$P_2W_{17}O_{61}$)$^{-10}$] = 34.7 mM.

Figure 3.10 shows the influence of increasing the [Na^+] concentration for the Pr(III) analog. The spectrum at 0.02 M added Na^+ resembles the spectrum with no added cation (Figure 3.3) where the 1:1 species is only observed. As the [Na^+] is increased, the a1 peak shifts downfield and broadens. At 0.25 M, the peaks b1 and b2 representing the 1:2 species appear and increase with increasing Na^+ ion concentration.

3.3.1.5- As a function of praseodymium concentration

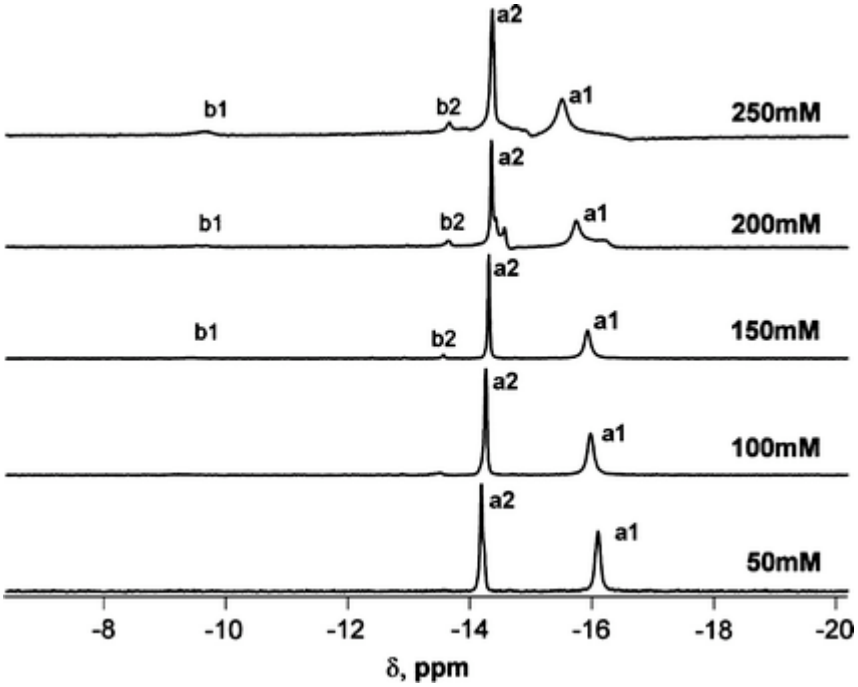

Figure 3.11. Reaction of Pr^{3+} with $Li_{10}[\alpha_2\text{-}P_2W_{17}O_{61}]$ (1:1 stoichiometry) as a function of concentration of $Pr(\alpha_2\text{-}P_2W_{17}O_{61})$ complex (pH 4.92–5.77).

Figure 3.11 shows that the 1:2 species forms at a concentration of the praseodymium complex of 100 mM and higher. This behavior has been previously observed and reported with the Ce(III) analog suggesting the 1:1 to 1:2 equilibrium.

$$2[\mathrm{Ln}(\alpha_2-\mathrm{P_2W_{17}O_{61}})]^{7-} \rightleftharpoons [\mathrm{Ln}(\alpha_2-\mathrm{P_2W_{17}O_{61}})_2]^{17-} + \mathrm{Ln}$$

3.3.2- Discussion

From ^{183}W NMR and luminescence studies it was recognized that the 2:2 Ln (III): α2-$P_2W_{17}O_{61}^{-10}$ solid-state dimeric species, both the ‘‘cap-to-cap’’ and the ‘‘cap-to-belt’’ analogs, dissociated into a 1:1 species, represented as $[Ln(H_2O)_4(\alpha2\text{-}P_2W_{17}O_{61})]_7$). From ^{183}W and ^{31}P NMR spectroscopy, Pope showed that the 1:1 species and the 1:2 [Ce(α2-

$P_2W_{17}O_{61})_2]^{-17}$ species were in equilibrium with an equilibrium constant 1.46 [11]. In one of our previous report[41] on the mid-late lanthanide complexes of the α2-$P_2W_{17}O_{61}^{-10}$ species, we observed equilibrium between the 1:1 and 1:2 species in the luminescence spectroscopy (micromolar concentration) in water at pH 6.0. Under this condition we can establish that the 1:1 to 1:2 Eu: α2-$P_2W_{17}O_{61}^{-10}$ equilibrium is on the order of micromolar [41]. This study reports solution speciation studies as a function of pH, cation, cation concentration and lanthanide concentration for the Ln: α2-$P_2W_{17}O_{61}^{-10}$ species. Examination of the solution chemistry of Pr(III), Eu(III) and Yb(III) monitored by ^{31}P NMR studies, shown in Figure 3.3, 3.4 and 3.5 reveals the influence of the cation in the speciation of the 1:1 Ln: α2-$P_2W_{17}O_{61}^{-10}$ species. For the early (Pr) and mid (Eu) lanthanides, the larger, less extensively hydrated alkali metal cations induce the formation of the 1:2 $[Ln(\alpha2\text{-}P_2W_{17}O_{61})_2]^{-17}$. Concentration of cation also influences the distribution between the 1:1 and 1:2 species, Figure 3.10. However the later lanthanide (Yb) is not affected by the identity of the cations as it maintains the 1:1 stoichiometry with all of them. We can hypothesized that large, less extensively hydrated alkali metal cations bind to the surfaces of the polyoxometalates and ‘‘anchor’’ the POM units in place for assembly into larger structures, such as the 1:2 sandwich structures. Kirby and Baker propose the possibility of ion pairing of large cations (Rb^+) to POM surfaces in a study to understand the solution ‘‘cis’’ structure of $Th(\alpha2\text{-}P_2W_{17}O_{61})_2^{-16}$ [49]. We and others have observed the role of cations on the speciation of $XW_9O_{34}^{-n}$ (X = P, n = 9; X = Si, n = 10).[36,50] K^+ and Cs^+ exclusively promote 1:2 $[Ln(PW_{11}O_{39})_2]^{-13}$ and $Cs_{15}K(SiW_{11}O_{39})_2$, with K^+ bound in the cavity. Laronze et al. [50] proposes, according to the solid-state crystal structure, that the Cs^+ anchors the $SiW_{11}O_{39}^{-8}$ species which promote the formation of the

1:2 K^+:POM complex. Also to corroborate the hypothesis, the solid-state structure of $Cs_{15}K(SiW_{11}O_{39})_2$ shows that three Cs^+ ions are bound to terminal oxygen atoms of each $SiW_{11}O_{39}^{-10}$ unit (with Cs–O distances of ca. 3.2 Å). This maybe help stabilizing the $K(SiW_{11}O_{39})_2^{-15}$ solid-state structure as the molecule dissociates in aqueous solution.

Ion pairing of alkali metal cations to polyoxometalates, it has been seen that the larger and less extensively solvated alkali-metal cations form smaller (more intimate) association complexes with the $(Xn^+VW_{11}O_{40})^{9-n}$ (X = P(V), Si(IV), Al(III)) family of polyoxometalates [51,52]. Also, our observations on the solution speciation of the 1:2 Ln(α1-$P_2W_{17}O_{61})_2^{-17}$ species [53] corroborate the cation effect. Cations are found to be crucial for the formation of 1:2 Ln(α1-$P_2W_{17}O_{61})_2^{-17}$ species in aqueous solution. In these ^{31}P NMR studies in aqueous solution, we can see that an equilibrium between the 1:1 and 1:2 is established with K^+ buffer. In Li^+ buffer, the 1:2 Ln(α1-$P_2W_{17}O_{61})_2^{-17}$ species completely dissociate into the 1:1 Ln(α1-$P_2W_{17}O_{61})_2^{-17}$ species and ligand (α1-$P_2W_{17}O_{61})_2^{-10}$. We suspect that the Cs^+ ions, and to an extent the K^+ ions, are binding to surface sites of POMs and thus stabilize the 1:2 structures in solution.

If we investigate the equilibria further by ^{31}P NMR spectroscopy, we observed that the ^{31}P NMR spectra recorded of aqueous solutions of the crystals of the Ce(III) 2:2 analog, prepared via the method reported in by Sadakane *et al*.,[11] with no additional electrolyte, showed a pH dependence (data not shown). At neutral to slightly basic pH, the ^{31}P NMR spectrum showed exclusively the 1:1 species, whereas at low pH (around 2) a small amount of the 1:2 species can be detected. The lanthanides Pr(III) and Nd(III) have a similar behavior which was not observed for the 1:1 analogs of the mid to late lanthanides. Indeed, the mid-late lanthanides (Eu(III) and Lu(III) at 10–30 mM of

crystalline material) at acidic to neutral pH, form only the 1:1 species. The pH study of the Eu(III) speciation, in low concentration of electrolyte, shown in Figure 3.9, corroborates this observation where the start of the 1:1 species occurs at lower [α2-$P_2W_{17}O_{61}$]$^{-10}$:Eu(III) ratios at the lower pH values. The range of the 1:2 species is increased at higher pH.

In Figures 3.6, 3.7 and 3.8, we observed that the 1:2 species is prevalent for the early-mid lanthanides, but the 1:1 species remains until high pH for the Yb (late lanthanide). These studies certify the significant impact of pH along with the cation in the distribution of the 1:1 and 1:2 species. The counterions and pH influence the lanthanides differently through the lanthanide. This behavior should be utilized in designing protocols for comparative experiments.

3.4- Conclusion

Michael T. Pope was the pioneer of the lanthanide complexes of polyoxometalates, including the (α2-$P_2W_{17}O_{61}$)$_2^{-10}$ ligand. Examination of the solution behavior of lanthanide complexes of the (α2-$P_2W_{17}O_{61}$)$_2^{-10}$ ligand are reported in this chapter to try to identify trends that will facilitate rational synthesis of hybrid organic lanthanide polyoxometalate complexes. Therefore, when we combine our data with that obtained by Pope [10], Kortz [40], and Krebs [45], a number of trends come into view. The 1:1 ↔ 1:2 equilibrium, observed by Pope for the Ce(III) analog [11], is established for the early-mid lanthanides and is slightly dependent on pH. Cations have a major influence on this equilibrium: for the early to mid lanthanides, larger, poorly hydrated cations appear to favor the 1:2 species; for the late lanthanide, cations do not appear to influence the

equilibrium when, the 1:1 species was stable in the absence of the 1:2 species, for all counterions.

3.5- References

(1) Hill, C. *Chem. Rev.* **1998**, *98*, 1.

(2) Mizuno, N.; Misono, M. *Chem. Rev.* **1998**, *98*, 199.

(3) Belai, N.; Sadakane, M.; Pope, M. T. *J. Am. Chem. Soc.* **2001**, *123*, 2087.

(4) Besserguenev, A. V.; Dickman, M. H.; Pope, M. T. *Inorg. Chem.* **2001**, *40*, 2582.

(5) Creaser, I.; Heckel, M. C.; Neitz, R. J.; Pope, M. T. *Inorg. Chem.* **1993**, *32*, 1573.

(6) Dickman, M. H.; Gama, G. J.; Kim, K.-C.; Pope, M. T. *J. Cluster Sci.* **1996**, *7*, 567.

(7) Gaunt, A. J., May, I., ; Collision, K.; Holman, K. T.; Pope, M. T. *J. Mol. Struct.* **2003**, *656*, 101.

(8) Kim, K.-C.; Pope, M. T. *J. Amer. Chem. Soc.* **1999**, *121*, 8512.

(9) Kim, K.-C.; Pope, M. T. *J. Chem. Soc. Dalton Trans.* **2001**, 986.

(10) Pope, M. T.; Wei, X.; Wassermann, K.; Dickman, M. H. *C.R. Acad. Sci. Paris* **1998**, *1*, 297.

(11) Sadakane, M.; Ostuni, A.; Pope, M. T. *J. Chem. Soc. Dalton Trans.* **2002**, 63.

(12) Termes, S. C.; Pope, M. T. *Transition Met. Chem.* **1978**, *3*, 103.

(13) Wassermann, K.; Pope, M. T. *Inorganic Chemistry* **2001**, *40*, 2763.

(14) Wassermann, K.; Dickman, M. H.; Pope, M. T. *Angew. Chem. Int. Ed. Engl.* **1997**, *36*, 1445.

(15) Saito, A.; Choppin, G. R. *Inorg. Chem.* **1991**, *30*, 4563.

(16) Saito, A.; Choppin, G. R. *Radiochimica Acta* **1995**, *68*, 221.

(17) Saito, A.; Tomari, H.; Choppin, G. R. *Inorganica Chimica Acta* **1997**, *258*, 145.

(18) Bion, L.; Moisy, P.; Madic, C. *Radiochimica Acta* **1995**, *69*, 251.

(19) Bion, L.; Moisy, P.; Vaufrey, F.; Meot-Reymond, S.; Simoni, E.; et al. *Radiochim. Acta* **1997**, 78.

(20) Chartier, D.; Donnet, L.; Adnet, J. M. *Radiochim. Acta* **1998**, *83*, 129.

(21) Milyukova, M. S.; Litvina, M. N.; Myasoedov, B. P. *Radiokhimiya* **1983**, *25*, 706.

(22) Milyukova, M. S.; Varezhkina, N. S.; Myasoedov, B. F. *Soviet Radiochem., Engl. Trans* **1990**, *32*, 361.

(23) Yusov, A. B.; Shilov, V. P. *Radiochemistry* **1999**, *41*, 1.

(24) Chiang, M.-H.; Williams, C. W.; Soderholm, L.; Antonio, M. R. *Eur. J. Inorg. Chem.* **2003**, *2003*, 2663.

(25) Duval, P. B.; Burns, C. J.; Clark, D. L.; Morris, D. E.; Scott, B. L.; et al. *Angew. Chem. Int. Ed.* **2001**, *40*, 3357.

(26) Gaunt, A. J.; May, I.; Helliwell, M.; Richardson, S. *J. Amer. Chem. Soc.* **2002**, *124*, 13350.

(27) Williams, C. W.; Blaudeau, J.-P.; Sullivan, J. C.; Antonio, M. R.; Bursten, B.; et al. *J. Am. Chem. Soc.; (Communication)* **2001**, *123*, 4346.

(28) Liu, S.; Kurth, D. G.; Bredenkotter, B.; Volkmer, D. *J. Am. Chem. Soc.* **2002**, *124*, 12279.

(29) Liu, S.; Kurth, D. G.; Mohwald, H.; Volkmer, D. *Adv. Mater.* **2002**, *14*.

(30) Okun, N. M.; Ritorto, M. D.; Anderson, T. M.; Apkarian, R. P.; Hill, C. L. *Chem. Mater.* **2004**, *16*, 2551.

(31) Mialane, P.; Lisnard, L.; Mallard, A.; Marrot, J.; Antic-Fidancev, E.; et al. *Inorg. Chem.* **2003**, *42*, 2102.

(32) Sadakane, M.; Dickman, M. H.; Pope, M. T. *Angew. Chem. Int. Ed.* **2000**, *39*, 2914.

(33) Muller, A.; Krickemeyer, E.; Bogge, H.; Schmidtmann, M.; Peters, F. *Chem. Int. Ed.* **1998**, *37*, 3360.

(34) Muller, A.; Sarkar, S.; Shah, S. Q. N.; Bogge, H.; Schmidtmann, M.; et al. *Angew. Chem. Int. Ed.* **1999**, *38*, 3238.

(35) Sadakane, M.; Dickman, M. H.; Pope, M. T. *Inorg. Chem.* **2001**, *40*, 2715.

(36) Zhang, C.; Howell, R. C.; Scotland, K. B.; Perez, F. G.; Todaro, L.; et al. *Inorg. Chem.* **2004**, *43*, 7691.

(37) Bartis, J.; Dankova, M.; Blumenstein, M.; Francesconi, L. C. *J. Alloys Compounds* **1997**, *249:*, 56.

(38) Bartis, J.; Dankova, M.; Lessmann, J. J.; Luo, Q.-H.; Horrocks, W. D. J.; et al. *Inorg. Chem.* **1999**, *38*, 1042.

(39) Bartis, J.; Sukal, S.; Dankova, M.; Kraft, E.; Kronzon, R.; et al. *J. Chem. Soc., Dalton Trans* **1997**, 1937

(40) Kortz, U. *J. Cluster Sci.* **2003**, *14*, 205.

(41) Luo, Q.; Howell, R. C.; Bartis, J.; Dankova, M.; Horrocks, W. D. J.; et al. *Inorg. Chem.* **2002**, *41*, 6112.

(42) Luo, Q.; Howell, R. C.; Dankova, M.; Bartis, J.; Williams, C. W.; et al. *Inorg. Chem.* **2001**, *40*, 1894.

(43) Peacock, R. D.; Weakley, T. J. R. *J. Chem. Soc. A* **1971**, 1836.

(44) Molchanov, V. P.; Kazanskii, L. P.; Torchenkova, E. A.; Simonov, V. I. *Crystallogr.* **1979**, *24*, 96.

(45) Drewes, D.; Krebs, B. *Z. Naturforsch* **2006**, *61b*, 637.

(46) Contant, R. *Inorg. Synth.* **1990**, *27*, 71

(47) Vogel, A. I. *A Text-Book of Quantitative Inorganic Analysis including Elementary Instrumental Analysis*; 3rd ed.; Longmans, **1961.**

(48) Zhang, C.; Bensaid, L.; McGregor, D.; Fang, X.; Howell, R. C.; Burton-Pye, B. P.; Luo, Q.; Todaro, L.; Francesconi, L. C. *Journal of Cluster Science* **2006**, *17*, 389.

(49) Kirby, J. F.; Baker, L. C. W. *Inorg. Chem.* **1998**, *37*, 5537.

(50) Laronze, N.; Marrot, J.; Herve, G. *Inorg. Chem.* **2003**, *42*, 5857.

(51) Grigoriev, V. A.; Cheng, D.; Hill, C. L.; Weinstock, I. A. *J. Am. Chem. Soc.* **2001**, *123*, 5292.

(52) Grigoriev, V. A.; Hill, C. L.; Weinstock, I. A. *J. Am. Chem. Soc.* **2000**, *122*, 3544.

(53) Zhang, C.; Howell, R. C.; McGregor, D.; Bensaid, L.; Rahyab, S.; Nayshtut, M.; Lekperic, S.; Francesconi, L. C. *C.R. Chimie* **2005**, *8*, 1935.

Chapter 4: Eu(POM) in layer by layer composite

4.1- Introduction

4.1.1- General introduction

Nowadays, as everything tends to go smaller, modern technologies have been interested in the development of new molecular-based materials with the ability of either transport electrons and/or store electrons in order to decrease the size of the future electronic devices such as high density optical memory and photooptical switching. The challenge is to be able to control the structure of the materials and understand the electron transport phenomena in relation with molecular conductance.

4.1.2- Europium

Lanthanides are elements with interesting features that enable them to be used in different domains such as biochemistry, medicine, or photophysics. Their special photophysical properties are due to their inherent orbital configuration and binding ability. They possess a unique $4f^n$ configuration which gives them useful spectroscopic and magnetic properties. The region of emission bands of lanthanides can range from visible with europium (Eu) and terbium (Tb) which exhibit a red and green color respectively after excitation to near infrared (NIR) with erbium (Er) or and IR

neodymium with (Nd). In the medical domain, gadolinium complexed with chelating ligands is well used as contrast agent in magnetic resonance imaging (MRI)[1,2]. In biological research, lanthanides have been used in biological assays such as DELFIA (dissociation enhanced lanthanide fluoroimmunoassay).[3] One of the important characteristic of these lanthanide ions, which makes their biological application possible, is their long life time in the order of milliseconds. When a reported molecule is considered for biological optical imaging, the important factor to take into consideration is the lifetime relative to the lifetimes of the biological system. While most of the emissive states of macrocyclic aromatic molecules are quenched by their biological media (oxygen from the air), the emissive lanthanide ion is not affected by its aerobic environment because of its filled 5s and 5p shells which act as a shield to its 4f partly filled orbitals. Moreover, biological systems have a life time in the order of nanosecond which is six orders of magnitude lower from the lanthanide emission lifetime, and makes their signal separation easy when using a time-gating separation technique.

Even though the lanthanides are not affected by the surrounding oxygen from the air, they can be quenched by O-H or N-H oscillators through non-radiative quenching. In order to minimize the quenching effect from the surrounding molecules susceptible to affect the europium luminescence (see Chapter 1 Section 5.3) the europium is incorporated or encapsulated within chelating ligands. This chelate will bind to the lanthanide preventing the approach of an “exterior quencher”. Lanthanides being hard Lewis acids favor complexing to atoms that are hard Lewis bases such as nitrogens or

oxygens. Therefore the ligands that bind to lanthanide contain O or N. Such chelators can be (1) cyclic ligands such as DOTA derivatives (see Chapter 1 Section 2) previously mentioned as ligands to Gd for MRI contrast agents, (2) polydentate ligands such as EDTA derivatives (see chapter 1 section 2) or (3) clusters such as polyoxomethalate (POM) (see chapter 3).

Even though the lanthanide is partially protected from the eventual nonradiative quentching from O-H groups, their extinction coefficients remain small due to the Laporte forbidden f-f transitions. The presence of a sensitizer is needed to enhance the lanthanide luminescence.

They need to be excited via an intramolecular energy transfer from another organic aromatic chromophore or antenna. This chromophore will absorb light and will get excited from a S^0 to a S^1 singlet state. This energy will then get transferred to its triplet state T^1 through an inter system crossing (ISC) and then will get transferred through energy transfer (E.T.) to the metal emitting state. Both triplet state of the ligand and emitting state of the metal should be comparable to prevent energy loss (Figure 4.1).[4,5]

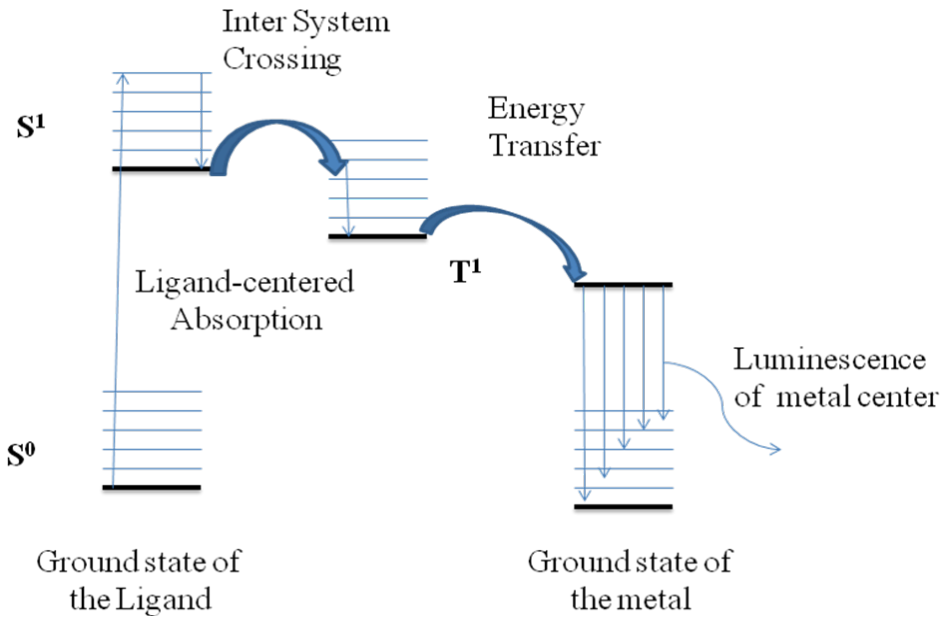

Figure 4.1. Energy transfer schematic from the ligand to the metal center via the ligand triple state.

This sensitizer could be part of the ligand as a pendant arm or could be a foreign aromatic molecule which will be subsequently attaching to the Ln for sensitization. This binding can be done covalently [6-11] or electrostatically [12-14]. This electrostatic bonding comes from the fact that lanthanides are highly charged, they have a strong electrostatic nature in their bonding due to the polarization of the ions and their hard Lewis acid character.

4.1.3- Layer by layer

4.1.3.1- Introduction

In the past four decades, materials science has fused with many other chemistry fields such as organic chemistry, polymers, biology and inorganic in order to achieve multicomposites with higher device functionalities, better stability and tunability. This assembly would require control of molecular orientation, and nanoscale orientation. The deposition of consecutive layers onto a planar solid support in order to form multilayers is a way to control the orientation in only one dimension[15]. This self-assembly procedure, which can be carried out manually, involves the electrostatic interaction of polyions or other charged molecules. It entails the adsorption of polyanions and polycations consecutively onto a solid support, most commonly a glass slide (Figure 4.2).

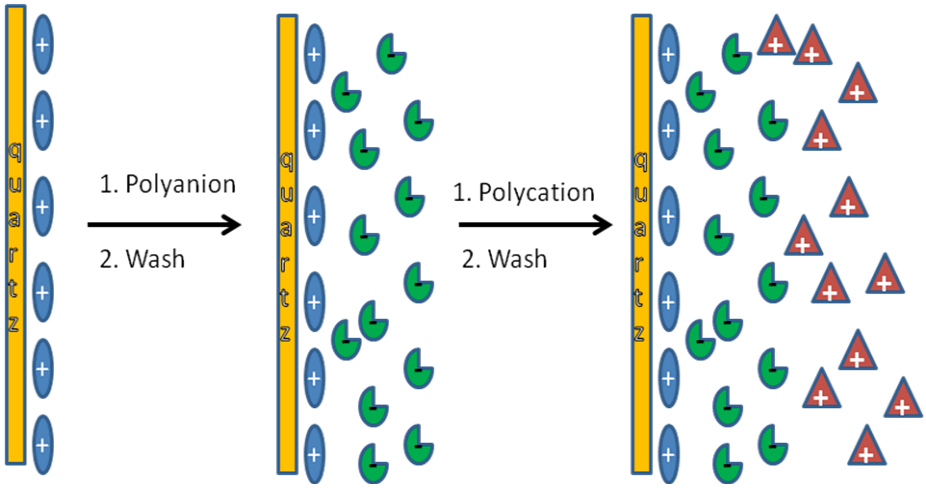

Figure 4.2. Simplified molecular picture of the two adsorption steps starting with the positive charged substrate PEI, the deposition of the polycation layer and the deposition of the polyanion layer.

4.1.3.2- Polyoxomethalate for layer by layer deposition

Because of the high stability of most of their redox states, the possible tunability of their redox potential by changing the heteroions without altering the structure, their high charges availability tunable with the incorporation of various metal cations, their wide solubility properties, and their versatility as building blocks, POM are good candidates in self assembly multilayer films. In this hybrid organic-inorganic material, POM is used as the anionic inorganic moiety with a molecule such as polyelectrolytes[16], porphyrins[17,18], dyes[19] or long alkyl chain amines[20,21] as the organic cationic moiety. These

polyelectrolytes provide strong electrostatic interaction between the positively charged layers and the negatively charged layers. Douvas reported the molecular layers of the Keggin structure $H_3PW_{12}O_{40}$ and the 1,12-diaminododecane on a silicon surface for charge transport control in molecular devices using electrical characterization[22].

4.1.3.3- Lanthanide polyoxomethalate for layer by layer deposition

POMs complexed with rare earth metals such as lanthanides have been used to fabricate photoluminescence films with cationic polyelectrolytes. The photoluminescence of POM containing lanthanide has been the center of investigation from various groups such as Yamase, Kurth and Xu[23-25]. This photoluminescence exists via the intramolecular energy transfer from the oxygen to metal charge transfer (OMCT) to the lanthanide cations. As several energy levels are present within the O to M ligand to metal charge transfer (LMCT) bands in the POM lattices, energy transfer from the OMCT excited states to this level can occur. This is observed for Eu^{3+}, Mn^{4+}, and Cr^{3+}[25]. Lin Xu reported the photoluminescence study of the europium cluster $EuP_5W_{33}O_{110}^{-12}$ and poly(allylamine) hydrochloride as layer by layer self assembly components. The fluorescence spectra of europium shows two main peaks at 590nm and 613nm corresponding to the $^5D_0$ to $^7F_1$ and $^5D_0$ to $^7F_2$ europium emission bands, but with low intensity[24]. Also Gao reported the study of multilayer films based on the cerium cluster $Ce(P_2W_{17})_2^{-17}$ and PAH, investigating its electrochromism [23]. Kurtz also reported

multilayer films containing POM clusters of $[Eu\text{-}(H_2O)P_5W_{30}O_{110}]^{-12}$ showing good electrochromism[26].

4.1.3.4- Transition metal for layer by layer deposition

Different ligands with transition metal complexes have been reported as the cationic moiety. Transition metal complexes have the unique properties to have well-defined surface functionality compared to conventional polyelectrolytes. Only a few cases were reported. Ingersoll and Kuhn investigated this combination of POM and chelated transition metal. Ingersoll reported the feasibility of $[Fe(phen)_3]^{3+}$ (phen = 1,10-phenithroline) and POM in different substrates using the LBL self assembly method and Kuhn studied the fabrication of multilayer films using bypiridine as ligand, $Os(bpy)_3^{2+}$ with $P_2Mo_{18}O_{62}^{6-}$ and $Ru(bpy)_3^{2+}$ with $P_2Mo_{18}O_{62}^{6-}$ on electrode surfaces[27,28]. In 2005, Xu investigated the color tunable electrochromic multilayer films of the $\alpha\text{-}P_2W_{17}O_{61}^{-10}$ with a copper complex $Cu(Phen)_2^{2+}$ and with an iron complex $Fe(phen)_3^{2+}$ [29]. Later, the fabrication of multilayer films using the phendione complexes of transition metal $M(phendione)_3^{2+}$ ($M = Fe^{2+}$ or Co^{2+} and phendione = 1,10-phenanthroline-5,6-dione) and polyoxomethalates $BW_{12}O_{40}^{5-}$ (BW_{12}) and $Co_4(H_2O)_2(PW_9O_{34})_2^{10-}$ (PW_9) was reported. In this study they investigated the electrochemical behavior of the phendione complexes in the films and the luminescence properties of the films. The emission spectrum of the

$[Fe(phendione)_3]^{2+}$ films showed a broad band at 672 nm arising from the MLCT absorption at 510 nm of the Fe to phendione transition[30].

Ma reported multilayer fabrication based on $PMo_{12}O_{40}^{3-}$ (PMo_{12}) and $Ru(bpy)_3^{2+}$, using layer by layer self assembly[31]. The film exhibited photoluminescence arising from the ligand to metal transition π^*- t_{2g} of the $Ru(bpy)_3^{2+}$ at 612 nm also observed by Malliaras[32]. Later, Ma and Wang[33] investigated a multilayers film consisting of a europium $H_3Eu(SiMo_9W_2O_{39})_2^{-10}$ and $Ru(bpy)_3^{2+}$. The film exhibited photoluminescence activity from the metal to ligand charge transfer (MLCT) state π^*-d of the bpy to the Ru^{2+} ion transition upon excitation at 470 nm.

4.1.4- Sensitizing via electrostatic interaction

Through the last decade, the interest towards electrostatic interaction has grown due to their synthetic advantage. Faulkner, Pope and DeCola reported few studies toward the mechanism of energy transfer without covalently synthetic apparatus, of the effectiveness of transition metal bearing cyanide[13] or carboxylates[14] and of chromophore bearing carboxylates and phosphonates as good sensitizer[12]. The idea is to excite a chromophore electrostatically attached to europium rather than being covalently bound to the ligand chelating Eu^{3+} in order to sensitize the europium through space. This can give more freedom way in the facile tunability of the sensitization. They all observed energy

transfer from the MLCT of the transition metal complex, used as chromophore, to the triplet state europium.

Earlier, we reported the synthesis of europium in a POM cluster being sensitized by phenanthroline, bipyridine, phthalic acid and picolinic acid in an acetonitrile solution. The Eu(POM) reacted with the various organic ligands in suspension. This bonding is suspected to also come from electrostatic interaction from the oxygen or nitrogen of the organic ligand [34].

4.1.5- Purpose

In this chapter, we will look at the fabrication of layer by layer film deposition containing $[Eu(\alpha1\text{-}P_2W_{17}O_{61})]^{-7}$ and $Zn(phen)_3^{2+}$. Phenanthroline (phen) and phenanthroline derivatives are richly charged chromophores which can effectively form stable complexes with transition metal ions. The POM $\alpha1\text{-}P_2W_{17}O_{61}^{-10}$ will be used as a receptacle of the europium ion conferring a highly negative charge to the europium cluster. In order to optimize the amount of absorbed harvesting light and energy transfer three molecules of phenanthroline will bind to a Zinc(II) ion (Zn^{2+}) and create a positively charged complex. Zinc acts as the anchor for the three phenanthroline ligands. The excitation will take place at the tail of the Phen absorption band to avoid any absorption overlap with the LMCT of the POM. Via the two positive charges of the

$Zn(Phen)_3^{2+}$ and the seven negative charges of the $Eu(\alpha1\text{-}P_2W_{17}O_{61})^{-7}$ cluster the two complexes have the potential to effectively interact electrostatically. This is why we will introduce the fabrication of a multilayer film using these two complexes as the positive and negative layers. The film building will be monitored by UV –vis and excitation at 325 nm (π-π^* Phenanthrolin absorption band) and at 397 nm (europium excitation band).

4.2- Experimental Section

4.2.1- General

Materials.

Nanopure water was obtained from a Millipore Reverse Osmosis Direct-Q System. The lacunary [$\alpha1\text{-}P_2W_{17}O_{61}$TBA], anion salt was prepared according to published methods and were identified by ^{31}P NMR.[35-37] Reagents such as phenanthroline, $Zn(NO_3)_2$ and polyethelenyleneimine (PEI) were purchased from Aldrich and used without further treatment. The PEI solution was prepared dissolving 100 mg in 10 mL water. All reagents were obtained from commercial sources and used as received. $Zn(Phen)_3.(PF_6)_2$ was synthesized according to followed procedure. All other reagents were of analytical grade and used as received. All reagents were commercially available and used without further purification.

4.2.2- Layer by layer self assembly films

Preparation of $Zn(Phen)_3.(PF_6)_2$

To a solution of $Zn(NO_3)_2$ (0.207 g, 1.09 mmol) and phenanthroline (0.613 mg, 3.1 mmol) in ethanol, a solution of NH_4PF_6 (0.533 g, 3.27 mmol) was added. A precipitate appeared and was isolated by vacuum filtration and washed with water and ether. To purify, the obtained white residue was dissolved in a small amount of acetonitrile. Ether was added to lead to a new white precipitate which was washed with ether. The white solid was isolated by vacuum filtration and air dried.

Preparation of the multilayers

The quartz slides were cleaned with a "piranha solution" (H_2SO_4/H_2O_2 (3:1). For 40minn, and thoroughly rinsed with distilled water. Further purification was carried out by immersion in a $H_2O/H_2O_2/NH_3OH$ (5:1:1) bath for 30 min.

Preparation of PEI-$[Eu(POM)-Zn(Phen)_3]_n$ multilayer film

The clean quartz slides were immersed in aqueous solution of polyethyleneimine (PEI) (10 mg/mL) for 20 min, washed with water and dried with nitrogen stream. The precoated quartz slides were then alternately immersed in (i) $Eu(\alpha1\text{-}P_2W_{17}O_{61})^{-7}$ (5 mM, 35 mM charge) and $Zn(Phen)_3^{2+}$ (17.2 mM, 34.4 mM charge) acetonitrile solutions; (ii) $Eu(\alpha1\text{-}P_2W_{17}O_{61})^{-7}$ (5 mM, 35 mM charge) and $Zn(Phen)_3^{2+}$ (1.74 mM, 3.48 mM charge)

acetonitrile solutions and (iii) $Eu(\alpha 1\text{-}P_2W_{17}O_{61})^{-7}$ (0.5 mM, 3.5 mM charge) and $Zn(Phen)_3^{2+}$ (17.4 mM, 34.8 mM charge) acetonitrile solution for 20 min.

Characterization of the films

UV-vis absorption spectra were recorded on a quartz slide using a Varian Cary 50 UV-visible spectrophotometer. Photoluminescence were recorded on a Flurolog Tau3 with a Spex 1934D phosphorimeter. Emission spectra were obtained after excitation at 325 nm and 397 nm.

4.3- Results and discussion

4.3.1- Layer by layer fabrication

UV-vis spectroscopy is used to monitor the layer by layer self assembly process of organic-inorganic composite films. Figure 4.3 shows the UV-vis absorption spectra of the multilayers assembled on quartz substrate for PEI-Eu(POM)-$Zn(phen)_3^{2+}$ multilayers at different concentrations. Three sets of experiments were performed where the concentrations of the EuPOM and Zn(phen) were changed: 1:1 ratio EuPOM versus Zn(phen), 1:10 ratio EuPOM versus Zn(phen), 10:1 ratio EuPOM versus Zn(phen). These ratios are charge concentration ratios not the molar ratios.

The term "(n+1)Eu(POM) + nZn(phen)" designates the multilayer film where EuPOM layer is deposited last, while the term "nEu(POM) + nZn(phen)" designates the multilayer film where Zn(phen) is deposited last.

If we look at the layer by layer and not the bilayer depositions, we can see that the absorption does not increase constantly, rather it increases when a layer of Zn(phen) is added and decreases when a layer of Eu(POM) is added. Both bilayer [{Zn(phen)}$_n$/{EuPOM}$_{n+1}$] and [{Zn(phen)}$_n$/{Eu(POM)}$_n$] absorptions increase at different rates. The UV-vis spectra for the three sets of experiments show two "independent-like" sets of absorptions, both increasing with the number of layers deposition (Figure 4.3).

It can be seen from the bilayers (n+1)EuPOM/nZn(phen) spectra, Figure 4.3a, a broad peak centered at 278 nm. This absorption peak is ascribed to the LMCT oxygen to tungsten of the PW_{17} polyanion. In layers nEuPOM/nZn spectra, Figure 4.3b, 3 other peaks can be observed: two sharp peaks at 227 nm and 273 nm and a broader peak at 300 nm. They are all assigned to the centered π-π^* transitions of the phenanthroline ligand. Figure 4.3c and 4.3d represented the absorptions of all layers superposed on the EuPOM/Zn(phen) 10:1 and 1:10 systems, respectively.

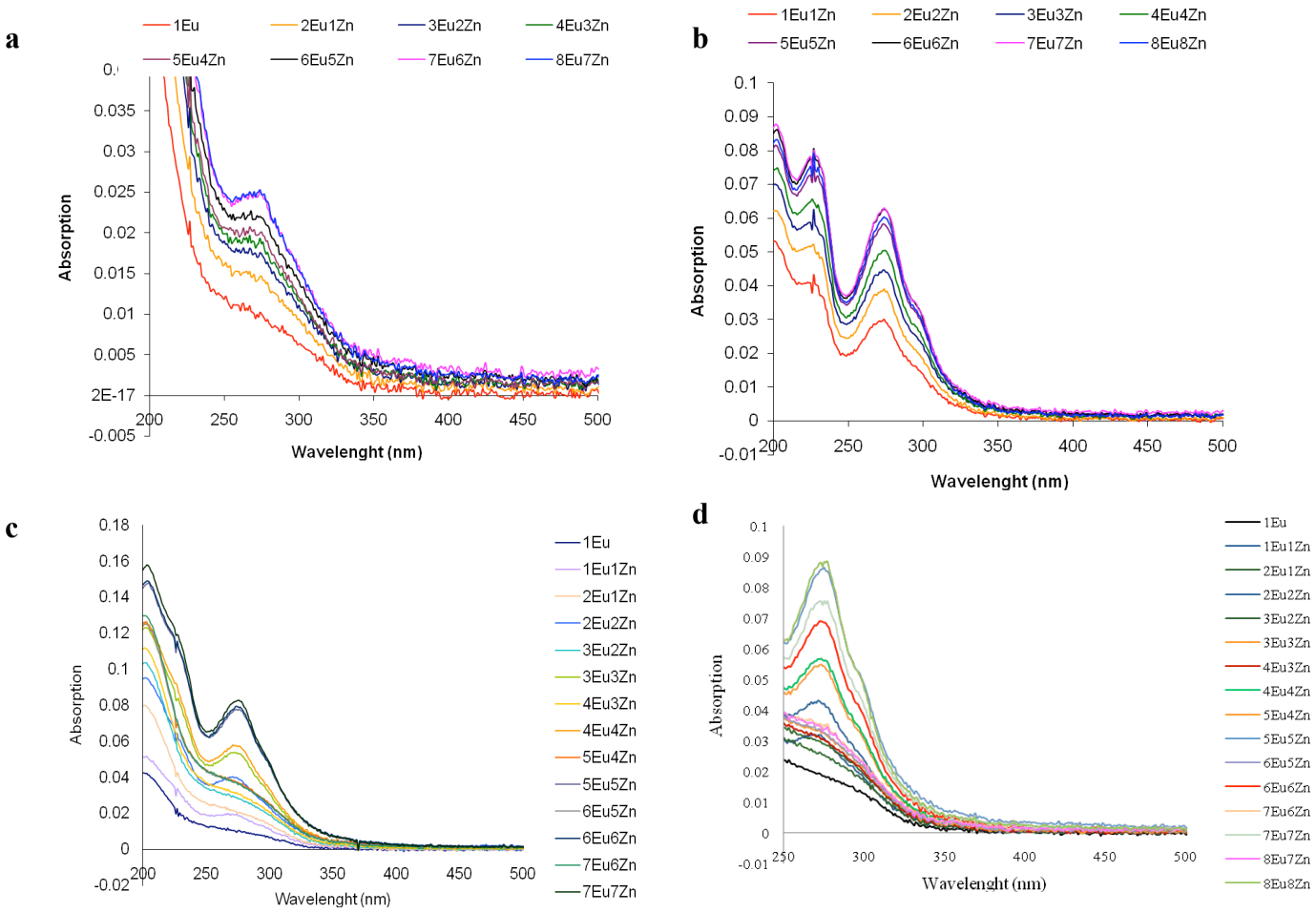

Figure 4.3. UV-vis spectra of (a) [{EuPOM}$_n$ /{Zn(phen)}$_n$]of 1:1 charge ratio, (b) [{EuPOM}$_{n+1}$ /{Zn(phen)}$_n$] of 1:1 charge ratio, (c) all combined absorption from all layers of the 10:1 charge ratio system (d) all combined absorption from all layers 1:10 charge ratio system.

If we follow the absorption at 276 nm ascribed for the phenanthroline π-π^* transition, we observed a regular increase until the deposition of 10 layers or 5 bilayers, after which a plateau is reached. We also observed a clear division between the absorption for the [{Eu(POM)}$_n$ /{Zn(phen)}$_n$] layers (red in Figures 4.4, 4.5 and 4.6) and the [{EuPOM}$_{n+1}$ /{Zn(phen)}$_n$] layers (blue in Figures 4.4, 4.5 and 4.6). The absorption of the [{Eu(POM)}$_n$ /{Zn(phen)}$_n$] bilayers increases more rapidly and with a higher intensity than the one of the [{EuPOM}$_{n+1}$ /{Zn(phen)}$_n$] bilayers. This phenomenon can be attributed to the fact that the EuPOM layer may act as a shield which prevents the light from penetrating and complicating the irradiation of the Zn(phen). The EuPOM layer buffers the phenanthroline absorption at 276 nm after each deposition.

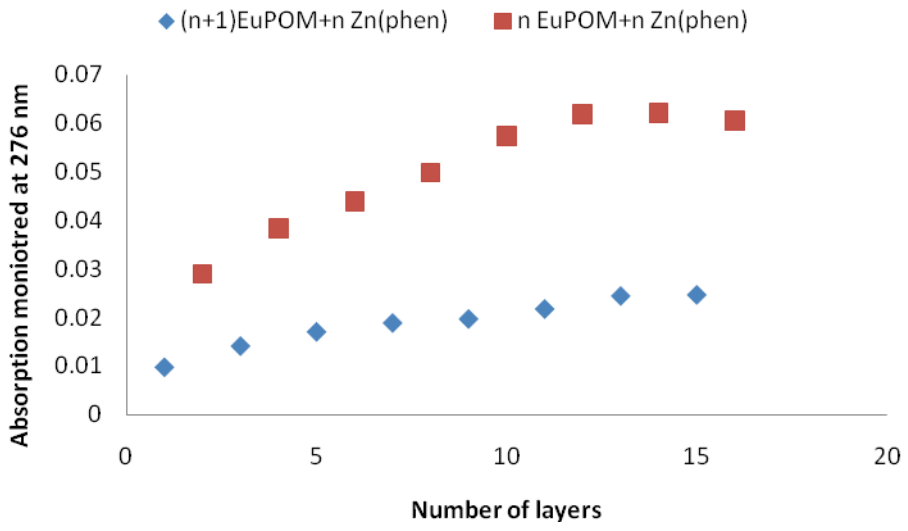

Figure 4.4. Plot of the absorptions from UV-vis monitored at 276 nm for the 1:1 EuPOM/Zn(phen) multilayer system.

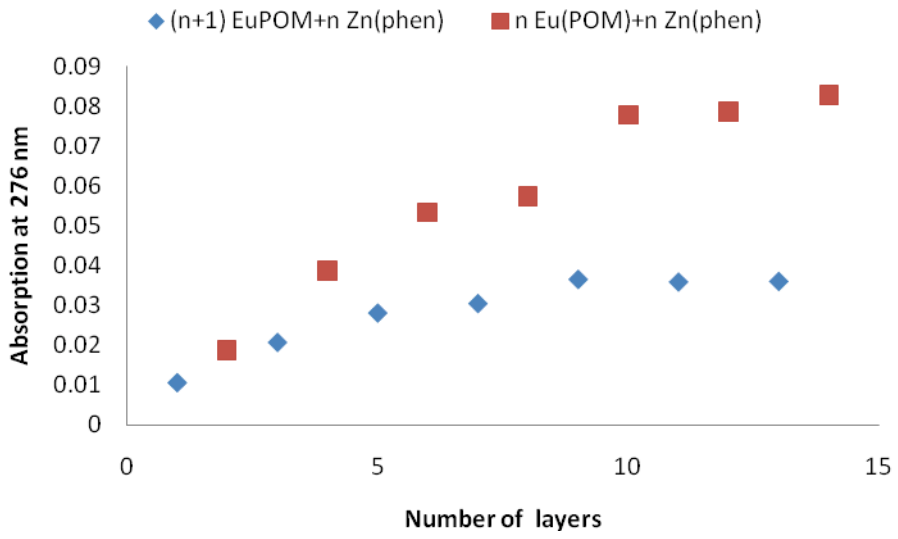

Figure 4.5. Plot of the absorptions from UV-vis monitored at 276 nm for the 10:1 EuPOM/Zn(phen) multilayer system.

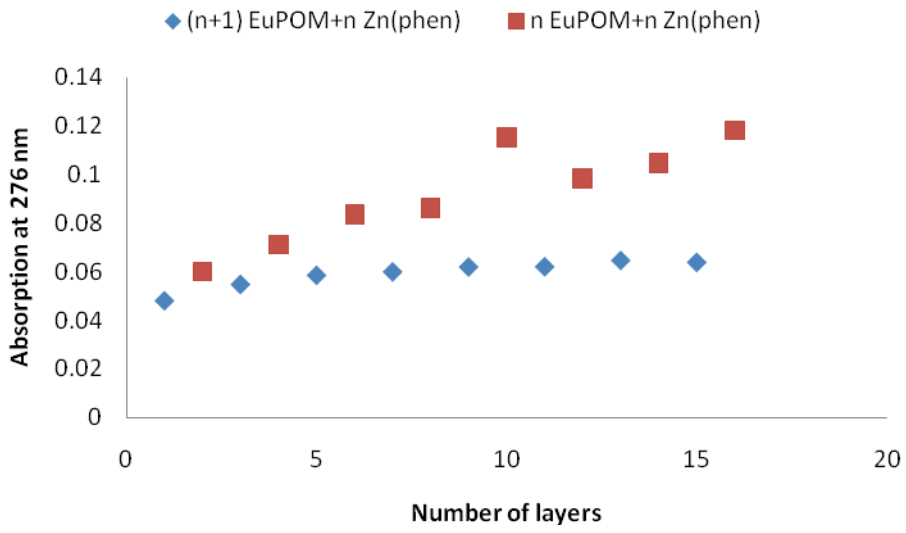

Figure 4.6. Plot of the absorptions from UV-vis monitored at 276 nm for the 1:10 EuPOM/Zn(phen) multilayer system.

Also a bathochromic shift from 274 to 280 nm can be observed for the phenanthroline absorption peak in the film compared to the Zn(Phen) in solution as shown in Figure 4.7. This red shift may be associated with a strong electrostatic interaction between the EuPOM and the Zn(phen) or a change of environment. Nevertheless, after 5 bilayers, the leveling off of the absorption of the UV-vis spectra may show the stripping off of the layers either the EuPOM layer and/or the Zn(phen) layer. Indeed, when examining the solution under a UV lamp, the phenanthroline solution shows a red color tint, characteristic of the presence of europium ions. Possible reasons of the stripping could be the decrease in EuPOM concentration or alterations in the film morphology.

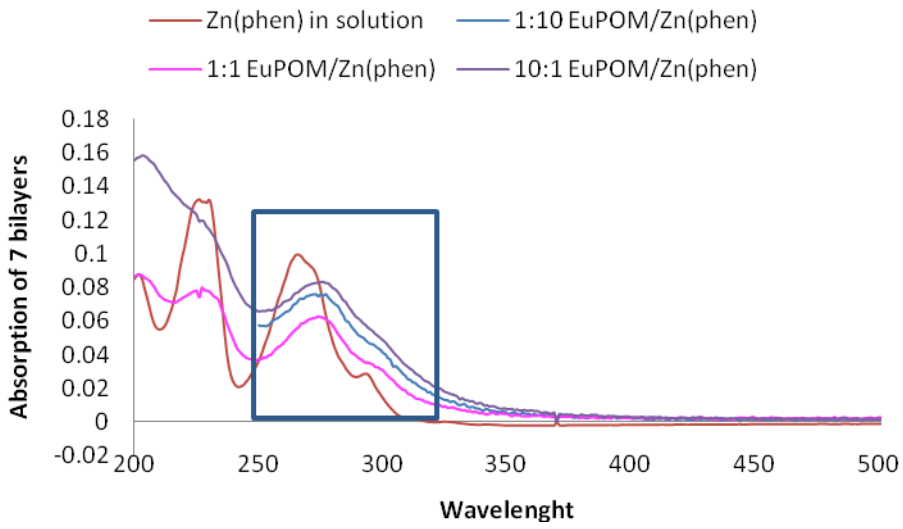

Figure 4.7. Comparative UV-vis spectra of the 7 bilayers film from the 3 differents concentration conditions and the Zinc phenanthroline in solution.

Looking at the two following figures (Figures 4.8 and 4.9), one can see that the three systems, with different concentration ratios, behave similarly towards the layer by layer deposition process. A variation of 2 degree of magnitude does not affect the absorption of the multilayer films.

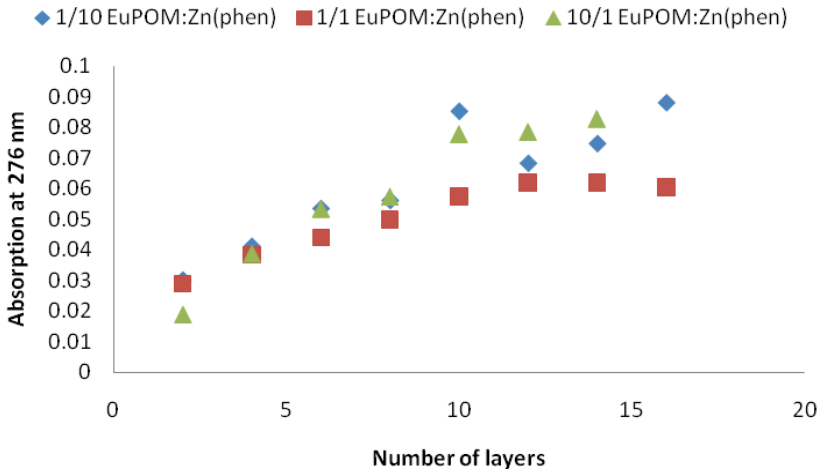

Figure 4.8. Comperative plot of the intensity of the absorption at 276 nm of multilayers $\{EuPOM\}_n/\{Zn(phen)\}_n$ *from the different ratio systems 1:1 (red), 1:10 (blue) and 10:1 (green) EuPOM/Zn(phen)*

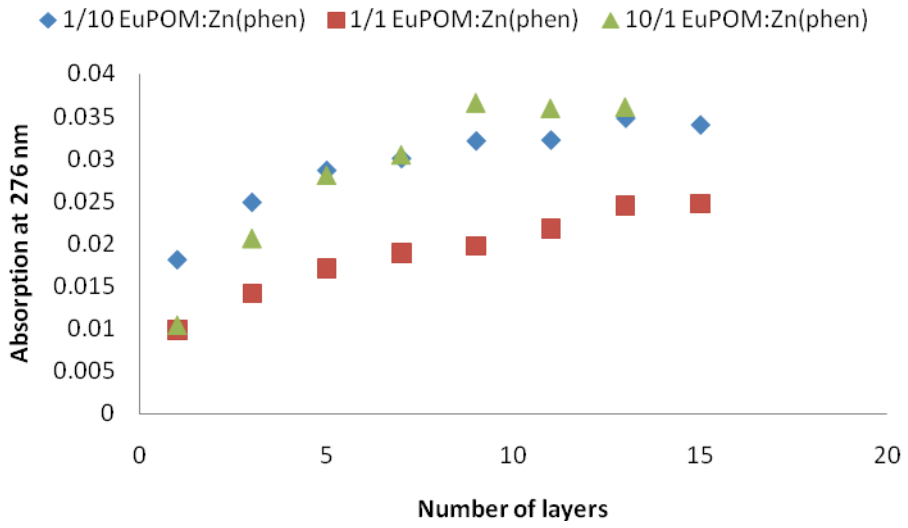

Figure 4.9. Comperative plot of the intensity of the absorption at 276 nm of the multilayers $\{EuPOM\}_{n+1}/\{Zn(phen)\}_n$ from the different ratio systems 1:1 (red), 1:10 (blue) and 10:1 (green) EuPOM/Zn(phen).

4.3.2- Effective energy transfer

The luminescence data are the important piece of this project. The reason why the layer by layer films have been excited at 325 nm is to avoid the excitation of the POM. The ε coefficient of POM being a thousand time less than the one of phenanthroline we chose to monitor the energy transfer phen → europium by exciting at the tail of the phen π-π^* transition band (325 nm) in order to avoid exciting the POM LMCT, so that the observed europium emission will only be caused by the through space charge transfer from the phenanthroline to the europium.

As explained earlier, we monitored the $^5D_0 \rightarrow ^7F_2$ hypersensitive transition of the europium at 614 nm after exciting the tail of the absorption band of phenanthroline at 325 nm in order to avoid any excitation of the POM LMCT and be able to watch the energy transfer through space of the phen to Eu. As we observed with the UV-vis absorption spectra, the intensity of the 614 nm peak can be divided into 2 sets of peaks one for the [{EuPOM}$_{n+1}$ /{Zn(phen)}$_n$] layers (green in Figures 4.10, 4.11 and 4.12) and one for [{Eu(POM)}$_n$ /{Zn(phen)}$_n$] layers (red in Figures 4.10, 4.11 and 4.12). Both of the set of data show an increase in emission of the Eu(III) with the number of layers deposition that level off after the 10th layer deposition or 5 bilayers. The increase for [{EuPOM}$_{n+1}$ /{Zn(phen)}$_n$] bilayers is not so pronounced whereas the increase for the [{Eu(POM)}$_n$ /{Zn(phen)}$_n$] bilayers is more steep. This was also observed for the UV-vis spectra. The hypothesis was the possible lack of light penetration through the Eu(POM) layer to excite the phenanthroline ligand.

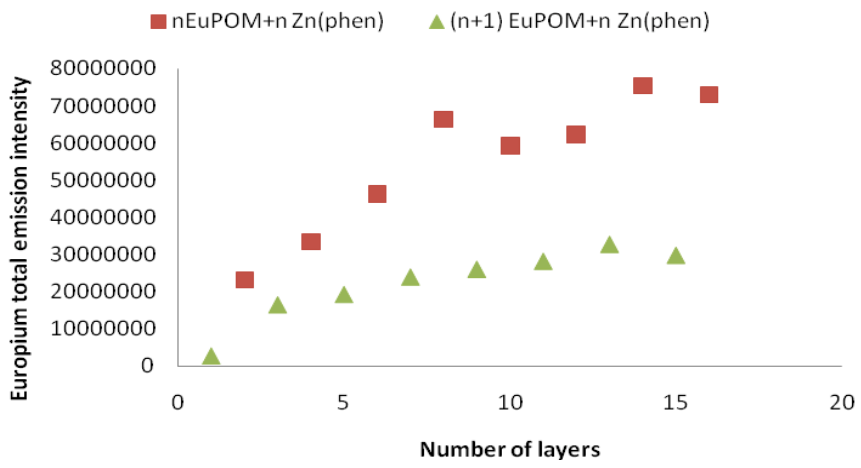

Figure 4.10. Total Emission intensity from the emission spectra of multilayers [{EuPOM}$_n$/{Zn(phen)}$_n$ in red and {EuPOM}$_{n+1}$/{Zn(phen)}$_n$ in green at $\lambda_{exc.}$= 325 nm using 1:1 EuPOM/Zn(phen) ratio.

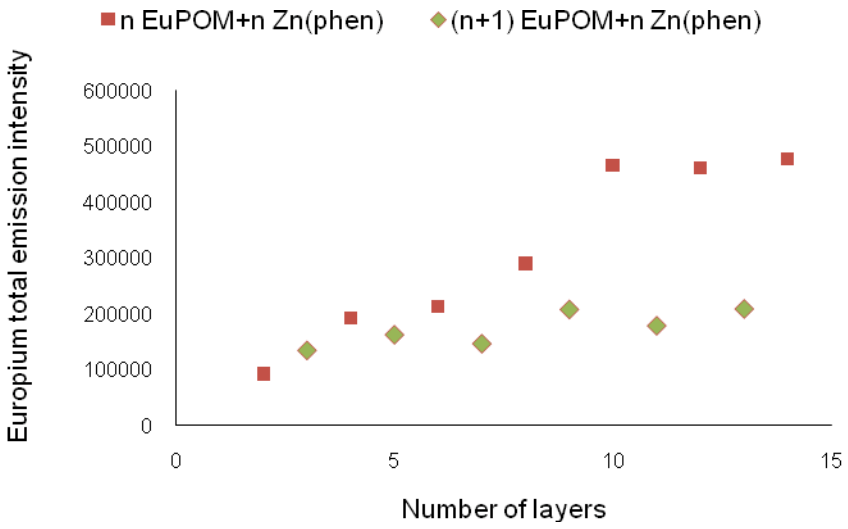

Figure 4.11. Total Emission intensity from the emission spectra of multilayers [{EuPOM}$_n$/{Zn(phen)}$_n$ in red and {EuPOM}$_{n+1}$/{Zn(phen)}$_n$ in green at $\lambda_{exc.}$= 325 nm using 10:1 EuPOM/Zn(phen) ratio.

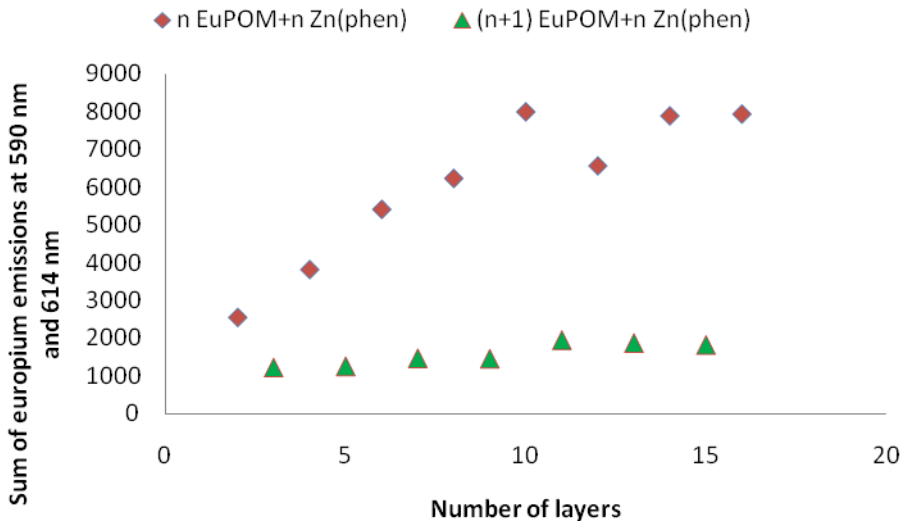

Figure 4.12. Sum of emission intensity at 614 nm and 590 nm from the emission spectra of multilayers [{EuPOM}$_n$/{Zn(phen)}$_n$ in red and {EuPOM}$_{n+1}$/{Zn(phen)}$_n$ in green at $\lambda_{exc.}$= 325 nm using 1:10 EuPOM/Zn(phen) ratio.

In Figures 4.13 and 4.14, we excite directly into 397 nm, which is the centered absorption band of europium. We observed for both 1:1 and 10:1 EuPOM/Zn(phen) ratio that the total emission intensities collected appear less irregular than the ones from the excitation at 325 nm. For the 1:1 ratio, two plateaus are observed monitoring the layer deposition of the europium layer which level off after 4 bilayers, beginning to strip off after the deposition of each Zn(phen) layer . For the 10:1 ratio the deposition of europium appears more monotonous with no real europium layer deposition as identify by the emission intensities of each layer until 4 bilayers when the emission increases slightly

and levels off. In this system we may have a constant stripping off as the europium concentration is high.

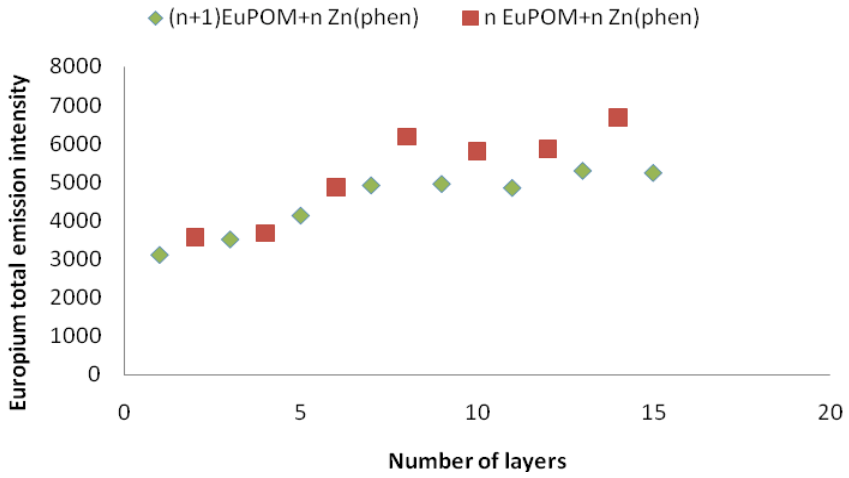

Figure 4.13. Emission spectra of multilayers [{EuPOM}$_n$/{Zn(phen)}$_n$ in red and {EuPOM}$_{n+1}$/{Zn(phen)}$_n$ at $\lambda_{exc.}$= 397 nm using 1:1 EuPOM/Zn(phen) ratio.

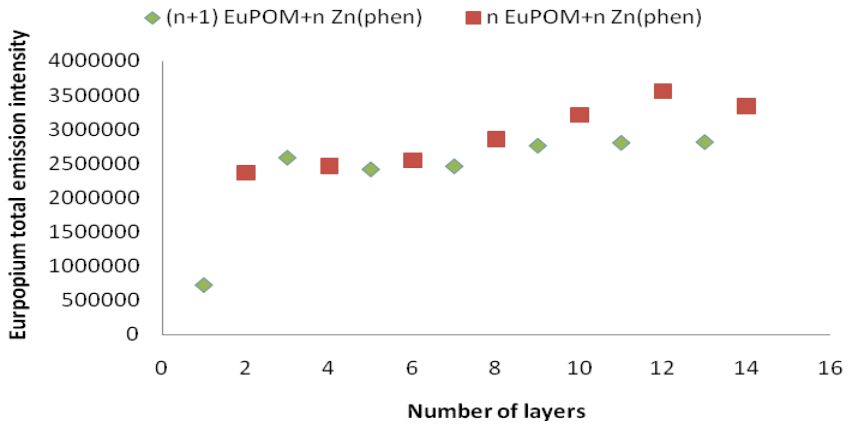

Figure 4.14. Emission spectra of multilayers [{EuPOM}$_n$/{Zn(phen)}$_n$ in red and {EuPOM}$_{n+1}$/{Zn(phen)}$_n$ at $\lambda_{exc.}$= 397 nm using 10:1 EuPOM/Zn(phen) ratio.

4.3.3- EuPOM configuration

Figure 4.15 is the ratio of the emission intensity at 614 nm and 590 nm. Where the emission at 614 nm is known as the hypersensitive transition which can give us information on the europium symmetry while the emission at 590 nm is an allowed transition which is not affected by the europrium symmetry or environment and is used as standard. What we see in this figure is 2 horizontal linear trends representing 2 distinct types of europium symmetries. We can show through this graph that the europium symmetry is indeed affected by the layer deposition and we can assess the position of the EuPOM as it deposits on top on the Zn(phen) layer. If the europium in the Eu-POM faces downward the europium symmetry would not be affected when an additional layer of Zn(phen) gets added. However, our results demonstrate that europium symmetry is affected each time a layer of Zn(phen) deposit on top of EuPOM. Figure 4.15 shows two distinct europium symmetries after each layer desposition. Therefore, it can be hypothesized that the EuPOM lays in such a way that the europium is facing upward as shown in Figure 4.16. Each Zn(phen) deposition affects the europium symmetry and each Eu(POM) deposition affects it back to its original symmetry.

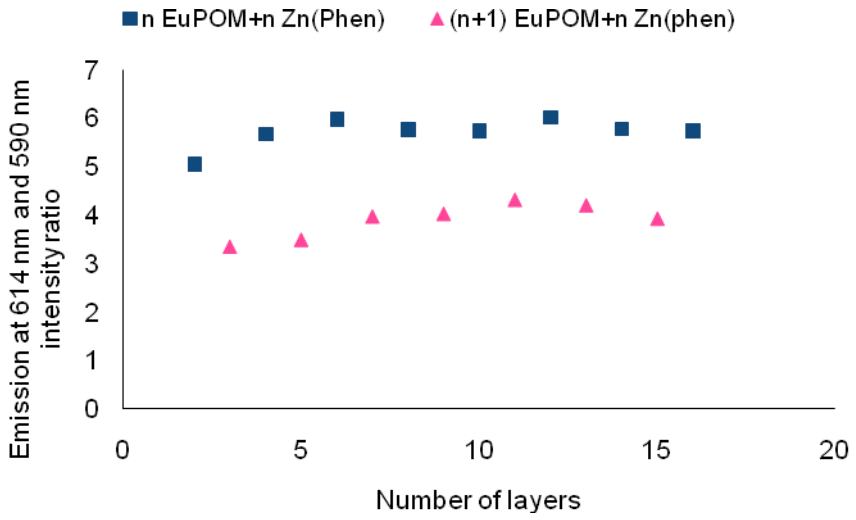

Figure 4.15. Emission at 614 nm and 590 nm intensity ratio (excitation at λ_{exc} = 325 nm) of a layer by layer self assembly film of EuPOM/Zn(phen) 1:1 ratio.

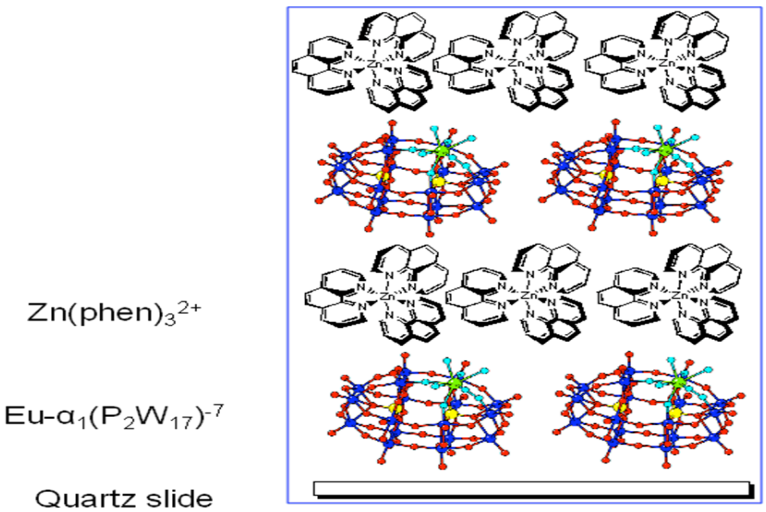

Figure 4.16. Schematic of a layer by layer deposition of EuPOM and Zn(phen) on a quartz slide.

This is also observed when using 10:1 or a 1:10 EuPOM/Zn(phen) ratio (Figure 4.17 and 4.18). Although, Figure 4.17 shows that at higher EuPOM concentration the symmetry of the europium does not follow as an ordered pattern as with the 1:1 or 1:10 which could be due to the over concentrated solution.

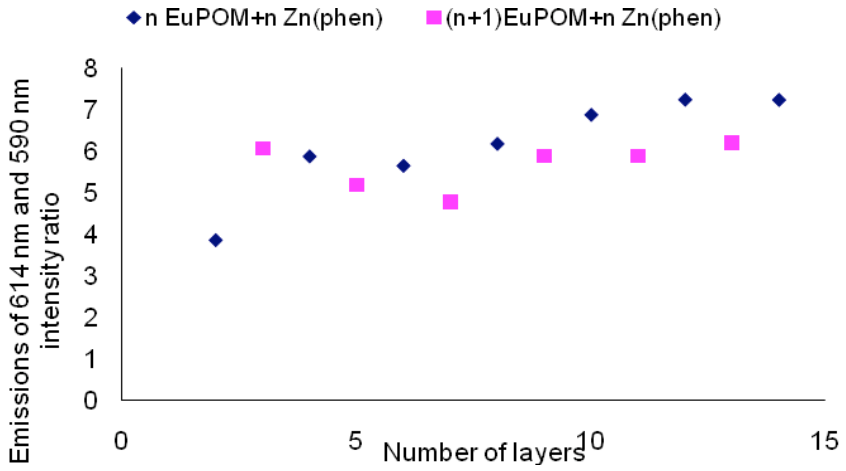

Figure 4.17. Emission at 614 nm and 590 nm intensity ratio (excitation at λ_{exc} = 325 nm) of a layer by layer self assembly film of EuPOM/Zn(phen) 10:1 ratio.

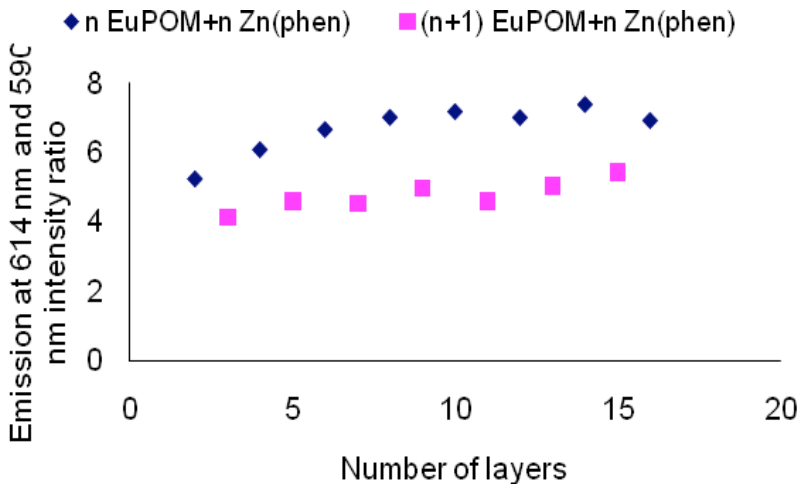

Figure 4.18. Emission at 614 nm and 590 nm intensity ratio (excitation at λ_{exc} = 325 nm) of a layer by layer self assembly film of EuPOM/Zn(phen) 1:10 ratio.

4.4- Conclusion

We successfully fabricate a multilayer film based on $Eu(\alpha 1\text{-}P_2W_{17})^{-7}$ and $Zn(phen)_3^{2+}$ on a quartz slide. The film fabrication has been monitored with UV-vis spectrophotometry. We see that in the three concentration ratios used the behavior of the films is very similar to one another. We can observe deposition until the 4 or 5 bilayers deposition then the layers are shown to strip off. From the luminescence studies, we reported an effective energy transfer from the phenanthroline to the europium. Also, the ratio of europium emission band at 614 nm, with respect to the emission band at 590 nm, revealed a prefered upward orientation of the EuPOM layer ontop of the Zn(phen)layer.

As future work, the study of the film with atomic force microscopy (AFM) can give us information on the topology and the thickness of the film, which can help us assessing the layering process. Also, a solution study in an anhydrous solvent can help confirming that the energy transfer is indeed from the phenanthroline to the europium. Moreover, since the $Zn(phen)_3$ cation can be isolated as a chiral complex and the EuPOM anion is inherently chiral, it gives us possibilities of studying layer by layer with chiral cations and anions.

4.5- References

(1) Alves, F. C.; Donato, P.; Sherry, A. D.; Zaheer, A.; Zhang, S.; Lubag, A. J. M.; Merritt, M. E.; Lenkinski, R. E.; Frangioni, J. V.; Neves, M.; Prata, M. I. M.; Santos, A. C.; de Lima, J. J. P.; Geraldes, C. F. G. C. *Investigative Radiology* **2003**, *38*, 750-760.

(2) Caravan, P.; Ellison, J. J.; McMurry, T. J. *Chem. Rev.* **1999**, *99*, 2293.

(3) Faulkner, S.; Pope, S. J. A.; Burton-Pye, B. *Appl. Spectr. Rev.* **2005**, *40*, 1-30.

(4) de W. Horrocks, W.; and Sudnick D.R. *J. Am. Chem. Soc.* **1979** *101*, 334.

(5) Supowski, R. M.; Bolender, J. P.; Smith, W. D.; Reynolds, L. E. L.; Horrocks, W. D. *Coord. Chem. Rev* **1999**, *307*, 185.

(6) Chang, A. C.; Liu, Y.-L.; Cheng, C.-Y.; Chou, X.-M. *Inorg. Chem.* **2001**, *40*, 3448.

(7) Quici, S.; Marzanni, G.; Cavazzini, M.; Anelli, P. L.; Botta, M.; Gianolio, E.; Accorsi, G.; Armaroli, N.; Barigelletti, F. *Inorg. Chem.* **2002**, *41*, 2777.

(8) Klink, S. I.; Hebbink, G. A.; Grave, L.; Oude Alink, P. G. B.; van Veggel, F. C. J. M. *J. Phys. Chem. A.* **2002**, *106*.

(9) Faulkner, S.; Pope, S. J. A. *J. Am. Chem. Soc.* **2003**, *125*, 10526.

(10) Li, M.; Selvin, P. R. *J. Am. Chem. Soc.* **1995**, *117*, 8132.

(11) Xiao, M.; Selvin, P. R. *J. Am. Chem. Soc.* **2001**, *123*, 7067.

(12) Pope, S. J. A.; Burton-Pye, B. P.; Berridge, R.; Khan, T.; Skabara, P. J.; Faulkner, S. *Dalton Trans.* **2006**, 2907.

(13) Baca, S. G.; Pope, S. J. A.; Adams, H.; Ward, M. D. *Inorg. Chem.* **2008**, *47*, 3736-3747.

(14) Coppo, P.; Duati, M.; Kozhevnikov, V. N.; Hofstraat, W.; De Cola, L. *Angew. Chem. Int. Ed.* **2005**, *44*, 1806.

(15) Decher, G. *Science* **1997**, *277*, 1232.

(16) Jiang, M.; Wang, E.; Kang, Z.; Lian, S.; Wu, A.; Li, Z. *J. Mater. Chem.* **2003**, *13*, 647.

(17) Shen, Y.; Liu, J.; Jiang, J.; Liu, B.; Dong, S. *J. Phys. Chem. B* **2003**, *107*, 9744.

(18) Bazzan, G.; Smith, W.; Francesconi, L. C.; Drain, C. M. *Langmuir* **2008**, *24*, 3244.

(19) Wang, Y.; Hu, C. *Thin Solid Films* **2005**, *476*, 84.

(20) Zang, G.; Chen, Z.; He, T.; Ke, H.; Ma, Y.; Shao, K.; Yang, W.; Yao, J. *J. chem. Phys. B* **2004**, *108*, 6944.

(21) Xu, B.; Xu, L.; Gao, G.; Jin, Y. *Applied Surface Science* **2007**, *253*, 3190.

(22) Douvas, A. M.; Makarona, E.; Glezos, N.; Argitis, P.; Mielczarski, J. A.; Mielczarski, E. *ACS Nano* **2008**, *2*, 733-742.

(23) Gao, G.; Xu, L.; Wang, W.; An, W.; Qiu, Y. *J. Mater. Chem.* **2004**, *14*, 2024.

(24) Xu, L.; Zhang, H.; Wang, E.; Kurth, D. G.; Li, Z. *J. Mater. Chem.* **2002**, *12*, 654.

(25) Yamase, T. *Chem. Rev.* **1998**, *98*, 307-326.

(26) Liu, S.; Kurth, D. G.; Mohwald, H.; Volkmer, D. *Adv. Mater.* **2002**, *14*.

(27) Kuhn, A.; Anson, F. C. *Langmuir* **1996**, *12*, 5481.

(28) Kloster, G. M.; Anson, F. C. *Electrochim. Acta* **1999**, *44*, 2271.

(29) Gao, G.; Xu, L.; Wang, W.; An, W.; Qiu, Y.; Wang, Z.; E., W. *J. Phys. Chem. B* **2005**, *109*, 8948.

(30) Gao, S.; Li, X.; Yang, C.; Li, T.; Cao, R. *Journal of solid state chemistry* **2006**, *179*, 1407.

(31) Ma, H.; Peng, J.; Chen, Y.; Feng, Y.; Wang, E. *Journal of Solid State Chemistry* **2004**, *177*, 3333-3338.

(32) Slinker, J.; Bernards, D.; Houston, P. L.; Abruña, H. D.; Bernhard, S.; Malliaras, G. G. *Chem. Commun.* **2003**, 2392.

(33) Ma, H.; Dong, T.; Zhang, W.; Gong, L.; Wang, F.; Li, C. *Journal of Colloid and Interface Science* **2007**, *311*, 523.

(34) Zhang, C.; Howell, R. C.; McGregor, D.; Bensaid, L.; Rahyab, S.; Nayshtut, M.; Lekperic, S.; Francesconi, L. C. *C.R. Chimie* **2005**, *8*, 1935.

(35) Contant, R. *Inorg. Synth.* **1990**, *27*, 71

(36) Bartis, J.; Sukal, S.; Dankova, M.; Kraft, E.; Kronzon, R.; et al. *J. Chem. Soc., Dalton Trans* **1997**, 1937

(37) Ciatorini, J. P.; Contant, R. *J. Chem. Research (S)* **1993**, *391*, 2720.